TWO DIMENSIONAL MESOSCALE SIMULATIONS OF PROJECTILE INSTABILITY DURING PENETRATION OF DRY SAND

By

RUSSELL DANIEL TEETER M.S.

A thesis submitted in partial fulfillment of
the requirements for the degree of

MASTER OF SCIENCE IN MECHANICAL ENGINEERING

WASHINGTON STATE UNIVERSITY
School of Mechanical and Materials Engineering

December 2007

To the Faculty of Washington State University:

The members of the Committee appointed to examine the thesis of RUSSELL DANIEL TEETER and find it satisfactory and recommend that it be accepted.

_____
Chair

_____

_____

ACKNOWLEDGMENTS

I first thank my advisor, Dr. Yogendra M. Gupta whose experience and support have been instrumental in the completion of this thesis. Dr. Gupta has always placed my personal development as a graduate student above all else, for this I am truly grateful. I would also like to thank Dr. Conrad W. Felice whose valuable input has guided this work. I also express appreciation to my Graduate Committee members, Dr. Jow-Lian Ding and Dr. David P. Field, for their guidance and time spent evaluating this thesis.

The time that Dr. Sunil Dwivedi has invested in me has been significant. It is he who introduced me to the mesoscale problem as an undergraduate and whose computational expertise has been invaluable for my graduate work. Over the years I have developed a deep respect for Dr. Dwivedi, and thank him for always having acted in my best interest.

I would also like to thank my parents, Verna and Gerald Teeter, for 25 years of love and guidance (as well as four and a half years of undergraduate tuition payments). I am greatly indebted to my wife, Trista Teeter, for her unwavering support during my graduate work. Last of all, I thank my daughter, Brooklyn, whose very existence has brought me happiness on even my most trying days.

This work was supported by AFOSR and DOE.

TWO DIMENSIONAL MESOSCALE SIMULATIONS OF PROJECTILE INSTABILITY DURING PENETRATION OF DRY SAND

ABSTRACT

By Russell Daniel Teeter M.S.
Washington State University
December 2007

Chair: Yogendra M. Gupta

Projectiles penetrating geologic media can experience instabilities characterized by divergence from their initial path and projectile bending. To gain insight into the effects of geologic features on projectile instability, a set of 2D non-continuum (mesoscale) simulations which account for the granular nature of sand was completed. The physical features of dry sand were accounted for by explicitly modeling and tracking each grain of sand in the target created using the program ISP-SAND. Penetration simulations were performed using the Lagrangian multi-body finite element code ISP-TROTP. Projectile instability was examined using projectile rotational momentum, unbalanced off-axis forces, and projectile deviation from path. Specific variables of interest were penetration velocity, grain size, grain distribution, target porosity, inter-granular friction, material properties, and sand grain randomness. Results show that the granular system can produce unbalanced radial forces which cause a projectile to become unstable. In all cases where penetration velocity was considered, projectiles became increasingly unstable as penetration velocities increased from 0.5 km/s to 1.5 km/s. For the cases considered, the effect of different target properties on projectile instability have

been quantified with reference to a set of baseline simulations. Throughout the simulations, which consider an elastic penetrator, an oscillation is seen with a uniform length scale that correlates with the lowest projectile bending mode.

TABLE OF CONTENTS

LIST OF FIGURES

LIST OF TABLES

SECTION 1
Introduction

This work constituted the initial phase of an ongoing effort to develop insight into possible causes of projectile instability when penetrating dry granular media (sand). To accomplish this, 2D finite element mesoscale simulations of projectile penetration into dry sand were conducted, and the sand grains were modeled explicitly to account for their response and interactions. A number of simulations were performed to quantify the effects of target parameters on projectile response. The work related to these simulations is presented here.

1.1 Motivation

Penetration of geologic media has been long studied with a focus on predicting depth of penetration (DOP). Starting in the eighteenth century[1], Robins[2] and Euler modeled penetration assuming that projectiles continued along their initial paths and experienced a constant deceleration. Since then a number of different DOP predication methods have been developed. These methods include the Poncelet[3, 4] method and cavity expansion[5] methods to name two approaches. In many cases, these types of methods work well and accurately predict penetration depth. However, there are a growing number of cases where these simple models fail and significantly overestimate penetration depth.

As a new generation of earth penetrators are developed, an emphasis has been placed on increased penetration depth and decreased damage to surrounding structures. Although these two requirements seem to be in opposition, one possible solution would be to use relatively small size high velocity projectiles[6]. To implement such a strategy,

a number of issues need to be understood. One of these issues, and the topic of this work, is a trend found in which projectiles become unstable when they decrease in size or increase in velocity[1, 7-11].

Projectile instability is characterized by severely bent or failed projectiles as well as projectile tumbling and deviation from the expected path[8, 10, 11]. This type of instability cannot be explained using the above DOP methods because unstable projectiles violate the implicit assumption (in these approaches) that projectiles remain on a nearly straight path during penetration. For this reason, the approach taken in this work was to simulate the early stages of penetration using a 2D approximation while taking into account the particulate nature of the targets: mesoscale features. The term mesoscale means that each randomly placed sand grain was simulated as it moved and interacted in the target. The inclusion of the sand grains in the model is necessary because it provides a realistic description of the sand media. The resulting heterogeneous loading on the projectile may cause the observed instability[12].

In these simulations, there are a number of variables which are not readily known. For example, determining the coefficient of friction between two sand grains at high relative velocities and large contact forces is not simple. Another feature that is not readily known is the material description of a grain of sand. Because there are a number of parameters, like these that are unknown, the intent of this work was not to accurately predict penetration depth. Instead, it was develop an understanding of the possible features which can causes projectile instability.

1.2 Objective and Approach

This work is the initial phase of a project to understand projectile instability during penetration. To begin developing this understanding, this work numerically examined the effects of grain scale heterogeneities (intergranular friction, grain size, grain shape, target porosity, etc) on projectile response during high velocity (1500 m/s) penetration of granular media. Specifically, three objectives were completed:

1. To realistically model the grain scale features of a granular media.
2. To simulate penetration into the granular media using tangent ogive projectiles.
3. To quantify the effects of grain scale features on projectile instability.

The first objective was completed using a Fortran program ISP-SAND, adapted from an earlier code written to produce polycrystalline metal domains. ISP-SAND uses an energy minimization technique along with Voronoi tessellation to place and construct the individual sand grains.

The simulations were carried out using the Lagrangian finite element code ISP-TROTP developed by Dr. Sunil Dwivedi. ISP-TROTP is an explicit multi-body wave propagation code with a robust contact algorithm which is a requirement for these simulations. These simulations required considerable computing power and ISP-TROTP was run on an Altix 4700 super computer, utilizing between 4 and 16 processors.

The effects of the mesoscale features on the projectile response were quantified in a number of ways. The simplest method was by visual inspection of the simulation results. If the projectile appeared to be tilted after one penetration depth then it was likely experiencing instability. Besides visual inspection, a number of more quantitative methods were also used to examine projectile instability. These methods quantified the

projectile rotational momentum, lateral displacement of the projectile center of mass, and the average lateral force applied to the projectile.

1.3 Organization of the Thesis

The ensuing sections provide the following information. Section two presents background information and cites instances when penetrator instability was found during penetration of geologic media. Methods used to explain projectile instability are discussed, and an overview of the mesoscale is given.

Section three contains a description of the simulation procedure. Topics such as target boundary conditions, target parameters, and measures of instability are discussed. Also, a discussion of the material models which were used is given

Section four has an in depth explanation of ISP-SAND. and discusses the sand placement method and the creation of the grain geometry. Section four also includes a verification of the numerical approach to produce specific targets as well as the meshing procedures used for both the target and penetrator geometry.

Section five details the simulation results, discusses the effects of various parameters on the penetration event and penetrator instability, and also discusses a possible cause of projectile instability. Finally, section six provides a summary and conclusions.

SECTION 2
Background

A compilation of the relevant literature is presented here. Section 2.1 discusses various experimental results where penetrator instability has been found. Section 2.2 discusses different explanations of projectile instability found in the literature. Section 2.3 is a description and explanation of the mesoscale simulation procedure developed by Dwivedi[13] and used in this work.

2.1 Experimental Evidence of Projectile Instability

A number of authors have reported penetrator instability during penetration into sand and geologic materials. In some cases, producing penetrator instability was the intent of the experiment. In others, the intent of the experiments was to avoid unstable penetration, but incremental increases in penetration velocity caused the penetrators to become unstable.

Allen et al.[1] fired 13mm diameter steel projectiles with length to diameter (l/d) ratios of 10 into unconfined sand targets. These projectiles had conical nose cones with varying nose cone angles. It was noted that the projectiles with nose cone angles less than 90 degrees became unstable (the smaller the angle the sharper the projectile) at velocities above 600 m/s, deviating from straight path and showing a decrease in penetration depth. It was also noted that projectiles left a trail of fine powered dust, illustrating sand grain fracture.

Biele[7] fired 13 mm diameter projectiles with 7.7 l/d ratios and conical tips into sand targets at 300 m/s and found that projectiles diverged from their expected paths. Byers et al.[9] displayed instability in a full scale projectile with a diameter of 155 mm

and an l/d ratio of 10. The penetrator was fired normally into a hard lake bed using a Davis gun at 300 m/s. The projectile had an ogive tip and became unstable leading to catastrophic failure. Frew et al.[14] found bending in steel and Aermet 100 projectiles with diameters of 7.1mm and 12.7mm. These projectiles had a 3 Caliber Radius Head (CRH) nose geometry and l/d ratios of 10. They were fired into limestone targets at 1600 and 1700 m/s and had initial pitch and yaw of less than 1 degree. Penetrators were found to be severely bent and to diverge from the initial path.

Savvateev et al.[11] fired tungsten alloy bullets with diameters of 4.7 mm and steel bullets with diameters of 6 mm, and length to diameter (l/d) ratios of 4.5 and 13.75 into dry sand at velocities ranging from 1.3 to 4 km/s. The recovered bullets were found to remain on a nearly straight path (shown using witness plates) but were highly deformed, possibly melted (depending upon initial kinetic energy), and had tumbled during penetration. It was also found that penetration depth decreased after a critical penetration velocity was reached.

Jones et al.[10] observed severe penetrator bending in 4.2mm and 12.7mm diameter projectiles with l/d ratios of approximately 10. The 12.7 mm diameter projectile was a steel ogive projectile and was fired into Eglin sand at 1500 m/s. The 4.2 mm diameter projectile was an aluminum ogive projectile and was fired into alumina power at 700 m/s. Both projectiles revealed similar bending upon final inspection. Along with bending, projectiles also deviated from their initial path.

As seen from the above reports of penetration experiments, there is a wide range of cases where projectiles exhibit instability. In each of these cases, projectile instability limited the penetration velocity at which projectiles could be fired effectively into

geologic targets. To mitigate this limitation, the underlying causes of penetrator instability need to be understood.

2.2 Instability Explanations

Explaining the causes of projectile instability is complicated due to the intense environment created during penetration. During penetration, projectiles experience large decelerations and can undergo intense heating[11]. These two features as well as others make obtaining data from the penetration event difficult. Simulating unstable penetration is also complicated because penetrators do not follow a straight path during unstable penetration. Thus, the degrees of freedom cannot be reduced in the simulation using the standard axi-symmetric approach[15, 16]. Further, standard continuum approaches cannot reproduce instability for initially normal penetration events because all applied loads to the projectile will remain symmetric.

Even with the above difficulties, a few authors have provided possible phenomenological explanations of penetrator instability in geologic media. In developing their explanations, authors focused on one of two types of instability. The first type describes projectiles, mostly retaining their shape, but veering off course. The second type is characterized by severe projectile bending or failure. Because these two types have distinct features, different explanations have been put forward for each.

Jones et al.[10] and Graham et al.[17] developed a projectile stability criterion for the case when penetrators show large amounts of bending. Their method is based on the dynamic buckling of long rods[18-21]. They postulated that if the loads applied to the penetrator were great enough to dynamically buckle the projectile then large amounts of bending would occur causing projectile instability. The results of their buckling

analysis are valid only for solid rod penetrators of constant diameter. However, their stability criterion was applied to two unstable penetration events and produced reasonable results.

Simonov and Osipenko[22] studied the case where projectiles retain their shape but diverge from their path. In their analysis, they use the frame work of separated flow to model penetration into elastic-plastic media. Their calculations consider frictional and normal forces which are focused at the nose cone of the projectile by the un-separated target material. When the authors introduce a perturbation to the forces at the projectile tip the projectile can turn drastically and even rotate a full 180 degrees. This analysis illustrates the unstable nature of penetrators when the target material is only interacting with the tip of the projectile.

Bishop et al.[23] used the Arbitrary Lagrangian Eulerian (ALE) code Alegra to model penetration of 7.1mm diameter 10 l/d ogive nosed projectiles into semi-infinite aluminum targets. Even though these simulations do not involve geologic media, they are of some value. Two simulations of interest involve 4340 steel penetrators impacting with a 2 degree angle of attack. Traveling at speeds of 570 m/s and 1580 m/s, the penetrators show drastically different results. The penetrator with the lower velocity performs much like a perfectly normal impact, while the high velocity penetrator turns and deforms so excessively that the simulation terminates early. This result indicates that small perturbations greatly increase in importance with penetration speed.

The above approaches are useful and make good use of available experimental data. However, what is lacking is the detailed description of the geologic target being penetrated. Because geologic media are intrinsically heterogeneous (or particulate), they

contain features which can contribute to projectile instability. It is the inclusion of the heterogenous features, inherent in geologic media, though the use of a mesoscale simulation technique that serves as the basis of the work reported here.

2.3 Mesoscale Description

While penetrating a geologic media such as sand, complex interactions of a system of heterogeneous interacting particles need to be considered. This particulate system cannot be properly described by complex continuum models developed to model two phase or porous materials[24-28]. Continuum models such as the P-α model[28] and Resnyansky's model[25] focus on mean stress volume relationships completely neglecting deviatoric stresses. Both dual-phase models work by averaging the properties of the two constituent materials (solid and void in this case) for application in a continuum framework. Because these models do not explicitly consider the interactions between the two phases, material surface effects such as wave reflections and complex material interactions at interfaces are neglected. These types of continuum models are not appropriate for penetration events in granular media.

A mesoscale or particulate representation, shown in Figure 2.1, is the more appropriate description of the target. This description is completed by explicitly considering individual constituents (grains) in a target. In the mesoscale approach, individual grains are allowed to interact with their neighbors and with the penetrator during the numerical simulations. The mesoscale approach automatically includes phenomena which are related to complex particle interactions and to local material boundary reflections that occur in the bulk of the material. These complex phenomena

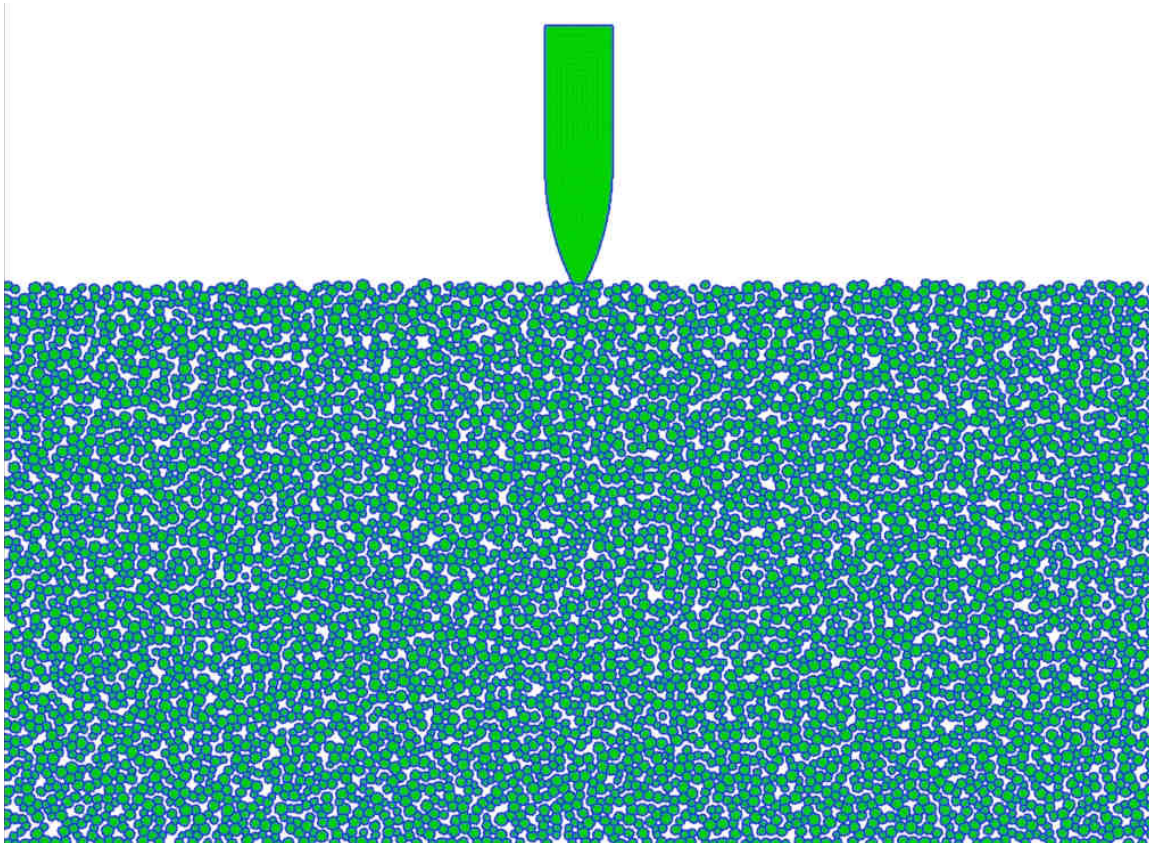

Figure 2.1: Penetrator positioned above a sand target. Individual sand grains and porous regions are represented explicitly in the mesoscale approach.

cannot be included in continuum simulations where the particulate target is replaced by a continuum.

Conducting mesoscale simulations is difficult and requires two main elements. The first component is a finite element hydrocode[29] capable of simulating multi-body contact, material nonlinearity, transient response, and the boundary conditions applied to each individual body. This requirement is fulfilled by the finite element code ISP-TROTP[13], developed and maintained at the Institute for Shock Physics (ISP) by Dr. Sunil Dwivedi. To date, ISP-TROTP is a two-dimensional (2-D) code. This issue is discussed in the next section.

The second requirement is a preprocessor to rapidly produce mesoscale target geometries. This role is filled by the program ISP-SAND, developed as part of this work from new algorithms and portions of another code ISP-VORN. ISP-SAND can produce targets with variable grain size, grain size distribution, porosity, and granular clustering.

SECTION 3
Methodology

Although many different types of geologic media are of interest for penetration studies, the present work is restricted to a particular granular material (dry sand). Dry sand was chosen as the target material for the following reasons:

1. Penetrator instability has been observed experimentally during penetration of granular media.
2. Each discrete sand particle can be modeled using an available single phase material model. Bulk material parameters are automatically implemented by considering targets at a granular level.
3. Because the granular media consists of a discrete set of bodies, simulation of penetration is facilitated without applying numerical techniques such as target erosion or projectile erosion.
4. Target parameters can be changed by simply changing the inter-granular properties of the grains or the grain morphology in the target.

The 2-D plane strain finite element simulation setup featuring penetration in a sand target can be seen in Figure 3.1. In these simulations, both the projectile and sand grains have been scaled down from experimental sizes. This was done so that a reasonable number (400,000) of plain strain triangular elements could be used while retaining numerical accuracy. In all cases, the projectile is a 3.5 caliber radius head (CRH) (discussed later) ogive projectile with a length to diameter ratio (l/d) of 3.85 where the length is defined

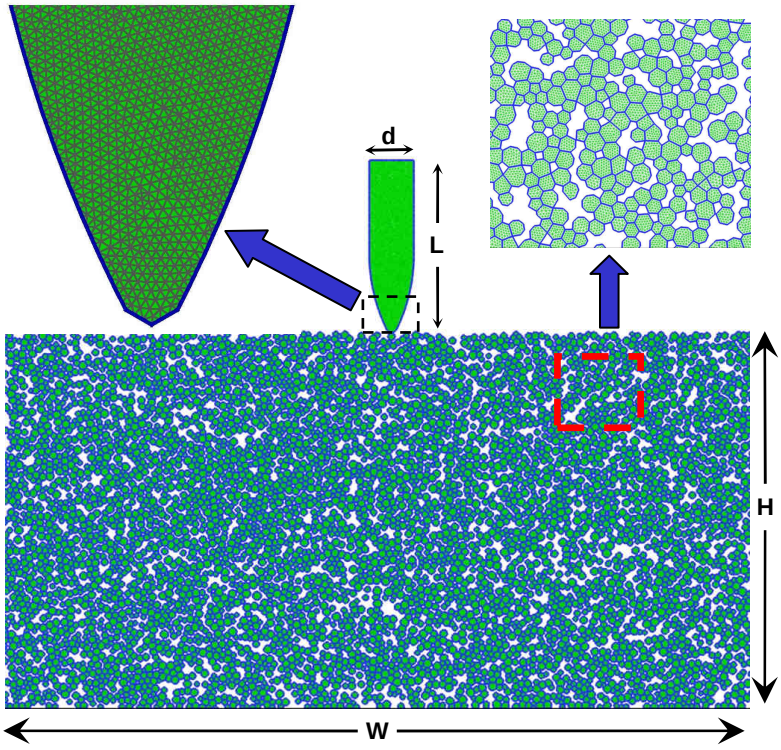

Figure 3.1: A typical 2D projectile and sand target created by ISP-SAND. The target has a porosity of 30% and each grain is modeled as simple (no phase change and non-damaging) quartz. The projectile is hardened steel having a tip modified 3.5 CRH Projectile with an l/d ratio of 3.85 and is modeled as hardened steel.

from projectile tip to projectile rear surface. The length of the actual simulated projectiles is 1.7 mm, which is scaled down from bullet sizes by about 10 to 15 times.

In many of the simulations, the sand grains comprising the target range in size from 45 – 75 μm. When scaled up by 10 - 15 times, these sand grains would be about .6 - .9 mm representing a medium to coarse sand.

As stated previously, these simulations consider 2-D projectiles and sand grains. Physically this means that the projectile is not a cylinder and the grains are not closed 3-D polygons. Instead, all the materials shown in Figure 3.1 are rods extending to infinity normal to the plain of the paper.

Selection of the finite element mesh size is complicated by the contact algorithm and the simulation of a chaotic environment. In these simulations, a 10um mesh size was used throughout; a justification is provided in appendix A. To give a scale of the mesh size, there are four element faces across each small flat section of the modified projectile tip shown in Figure 3.1.

A standard feature of wave propagation codes is the use of artificial viscosity [30-33] to avoid formation of shocks and to remove high frequency oscillations in the simulations. In a mesoscale code, artificial viscosity becomes particularly important because the contact algorithm cannot tolerate high frequency vibrations. The artificial viscosity values used here are typical values and were found to be acceptable for mesoscale simulations by Dwivedi et. al.[13] who used ISP-TROTP to simulate shock response in polycrystalline aluminum. The linear and quadratic artificial viscosity terms used here are listed in Table 3.1.

Table 3.1: Artificial viscosity values

Linear Artificial Viscosity Coeff.	q_L	0.5
Quadratic Artificial Viscosity Coeff.	q_q	4.0

3.1 Target Size and Boundary Conditions

Experimental evidence has shown projectile instability within one depth of penetration [8]. Because of these findings, it is assumed that simulated projectiles will show signs of instability within one complete depth of penetration. To simulate one penetration depth, the target has to behave as a semi-infinite body during the simulation time. To produce the required target dimensions (H and W in Figure 3.1), the size of the sand box was fixed so that a projectile traveling at 500 m/s (lowest projectile velocity requires the longest simulation time and the largest target) could complete one full length of penetration prior to edge effects influencing the simulations. The required target depth and height were approximated using the elastic wave speed of quartz, and this proved to be sufficient. Using this method, the standard target width was 7.076 mm and the height was 3.538 mm.

Fixed boundary conditions were applied to nodes at the left, right, and bottom edges of the target. However, these boundary conditions proved unnecessary as the particulate nature of the target slowed the transmission of stresses, and they never reached the target boundaries during simulation times.

Projectile placement was complicated by the changing surface geometry depending on the grain morphology used. To produce unbiased results, the same projectile placing procedure was used throughout the simulations. First, the x location of the projectile tip was positioned at the center of the target (W/2). Second, the y location of the tip was found by placing the projectile above the target and moving it down until contact was made between the sand grains and the projectile.

3.2 Penetrator Geometry

There are a large number of penetrator tip geometries which have been used. These include conical, bi-conic, power series, tangent ogive, secant ogive, elliptical, and parabolic[34]. This work only considers tangent ogive projectiles. The ogive tip, shown in Figure 3.2, is constructed by drawing two equal radii intersecting circles, creating a surface of revolution from the intersecting geometry; ρ is the circle/tip radius and D is the projectile diameter. With the ogive nose cone defined, two types of projectiles can be created. A tangent ogive is created when the location where the tip and shaft of the projectile meet (shoulder) are tangent to one another. This is not the case for the alternative nose shape called a secant ogive, where the projectile shoulder is moved forward making the nose cone shorter.

The ogive geometry shown in Figure 3.2 is expressed using Equations 3.1 and 3.2 below,

$$\rho = \frac{D^2 + L^2}{4D} \tag{3.1}$$

$$y = \sqrt{\rho^2 - (x - L)^2} + (\frac{D}{2} - \rho) \tag{3.2}$$

where L is the nose length from tip to shoulder and x is centered at the projectile tip. In this case y represents the upper curve of the projectile tip.

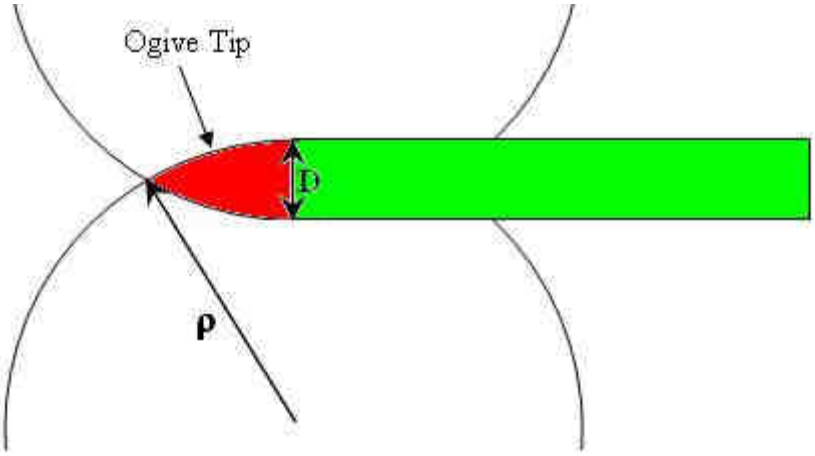

Figure 3.2: Geometric construction of a tangent ogive projectile

Ogive type projectiles are often characterized by a measure called caliber radius head (CRH) which is defined[35] as the nose cone ballistic length(tip to shoulder) divided by the nose cone radius of curvature ρ. The higher the CRH value, the sharper the nose cone. The smallest CRH value is 1 for which the projectile tip would be perfectly hemispherical.

3.3 Material Models

As indicated earlier, single phase and relatively simple material models were used to describe the individual grains in the mesoscale simulations. The complexity of the simulations is not due to the material models but due to the interaction of thousands of discrete interacting grains. The material models used in this work are fairly standard models, and the material properties were compiled by Dwivedi [36] from various literature sources. The material properties of a sand grain are not known precisely and quartz properties were used. The purpose of this work was to simulate penetration into a reasonable granular target and to determine the features that facilitate projectile instability. A brief description of the material models is given next.

The steel impactor was modeled as an elastic-plastic solid[37, 38] with material properties taken from Dwivedi et al. [39]. In the linear elastic region of the material the stresses are represented using Hook's law, shown in incremental form in Equation 3.3.

$$\dot{\sigma}_i = \lambda \frac{\dot{V}}{V} + 2\mu\dot{\varepsilon}_i \tag{3.3}$$

In this case λ and μ are Lamé material constants, V is the volume, and ε_i is the strain in the three principal directions (direction where shear stresses are not present).

As is standard practice, stress can be considered in two separate portions[31]. Stresses which contribute to a dilatation of the material (hydrostatic stresses) and the stress which correspond to shear distortion (deviatoric stress) of the material, shown in Equation 3.4,

$$\sigma_{ij} = p\delta_{ij} + S_{ij} \tag{3.4}$$

where σ_{ij} is the stress tensor (no longer in principal coordinates) and p is the mean stress or pressure, δ_{ij} is the identity matrix, and S_{ij} is the deviatoric stress tensor. The mean stress p was modeled using the Mie-Gruneisen equation of state (EOS) [31, 40-42] which takes the form of Equation 3.5.

$$p = (K\mu + K_1\mu^2 + K_2\mu^3)(1 - \frac{\Gamma\mu}{2}) + \Gamma\rho E \tag{3.5}$$

The terms in the Mie-Gruneisen EOS are as follows K, K_1, K_2 are bulk modulus constants and can be found in Table 3.2. Γ is the Gruneisen parameter and can also found in Table 3.2. The terms ρ and E are material density and internal energy defined by Equation 3.6.

$$E = \frac{1}{2}(K\mu + K_1\mu^2 + K_2\mu^3)(V_o - V) \tag{3.6}$$

Finally, μ is a ratio of initial to final density as defined by Equation 3.7.

$$\mu = \frac{\rho}{\rho_o} - 1 = \frac{V_o}{V} - 1 \tag{3.7}$$

In Equation 3.7, V and V_o is the volume at the compressed and initial states. Deviator stresses are calculated using Equation 3.8.

$$S_{ij} = 2Ge'_{ij} \tag{3.8}$$

In this model the material is assumed to have a constant shear modulus G which can be found in Table 3.2. In equation 3.8 e'_{ij} is the deviatoric strain tensor.

Plastic flow was incorporated through a Von-Mises plasticity rule. Using this rule the material transitions to elastic/plastic when the effective stress (a measure of distortional energy in the body) shown in Equation 3.9 exceeded the materials yield strength[31, 33, 37, 42].

$$\sigma_{eff} = \sqrt{\frac{3}{2} S_{ij} S_{ij}} \tag{3.9}$$

The yield strength used for the steel penetrator is a function of effective stress and was modified from the power form found in [39] to make a linearly increasing yield strength. This manipulation can be seen in Figure 3.3.

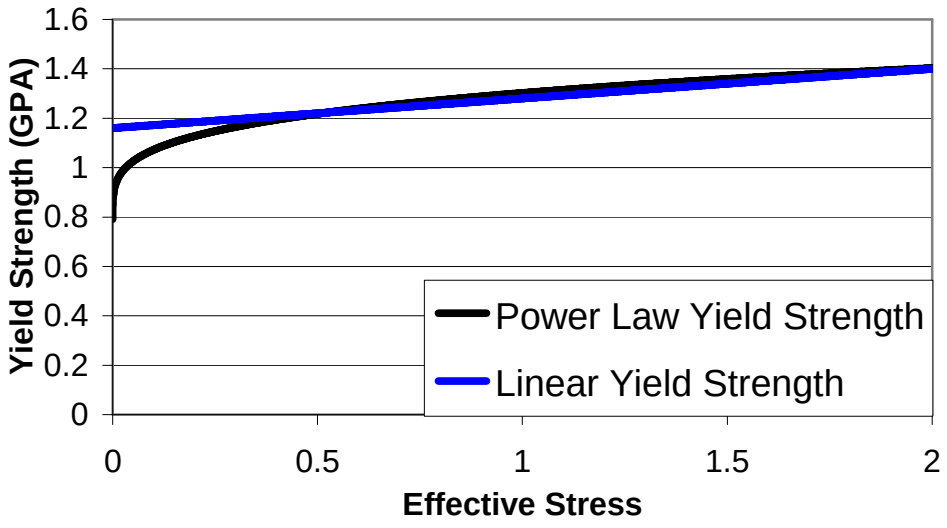

Figure 3.3: Linear fit of power law yield strength

The material model for the sand grains employs the same stress decompositions and Hook's law relations as in the steel model above, with a few key differences. In the sand grain model, the shear modulus is no longer constant and varies with mean stress.

The relationship between the shear modulus and the mean stress can be seen in equation 3.10.

$$G = G + G_1\bar{P} + G_2\bar{P}^2 \tag{3.10}$$

Here G, G_1,and G_2 are constants found in Table 3.3 and $\bar{P}$ is defined by equation 3.11.

$$\bar{P} = K\mu + K_1\mu^2 + K_2\mu^3 \tag{3.11}$$

The parameters for these two relations were taken from Winey [43] and are from work done on quartz single crystals.

The sand grain strength model is a time and mean stress dependent overstress model discussed in references [40, 44, 45]. The time dependency enters into the calculation through the deviator stresses in equation 3.12.

$$S_{ij} = S_{ij}^i \left[1 - \left(1 - \frac{\sqrt{S_{ij}^i S_{ij}^i}}{\sqrt{S_{ij}^e S_{ij}^e}} \right) \frac{\Delta t}{T_R} \right] \tag{3.12}$$

Where Δt is the current time increment, T_R is the relaxation time, superscript i denotes instantaneous values, and superscript e denotes equilibrium values.

The equilibrium yield strength is of a bilinear form which is a function of mean stress rather than effective strain. These material strength properties as summarized by Dwivedi[36] were taken from a number of sources pertaining to quartz[46-48]. Prior to these strength parameters, material parameters from work done by Hari and Gupta[45] on soda-lime glass were used. However, excessive deformation in the sand grains hampered the simulations. Figure 3.4 shows a plot of the equilibrium yield strength used in the simulations, the numerical values can be found in Table 3.3 where the yield strength is defined in the following way $Y = \sqrt{3J_2^{'}}$.

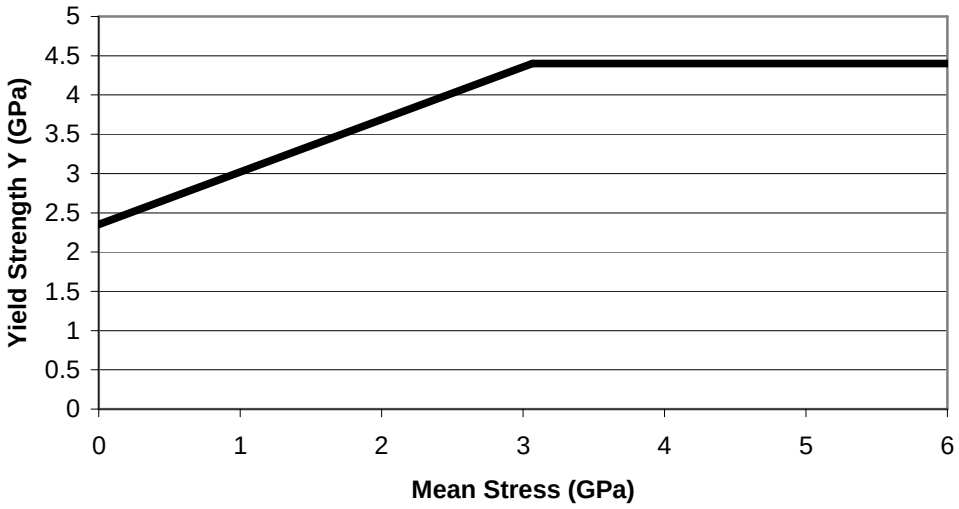

Figure 3.4: Mean stress dependent equilibrium yield strength

Table 3.2: Material properties for the steel projectile

Properties		Steel	Unit
Density	ρ	7823.0	Kg/m^3
Shear Modulus	G	77.50	GPa
Initial Yield Strength	Y	1.160	GPa
Hardness Parameter	M	.120	GPa
Bulk Modulus	K	163.9	GPa
First Order Bulk Modulus	K_1	294.3	GPa
Second Order Bulk Modulus	K_2	500.0	GPa
Gruneisen Parameter	Γ	1.16	-
Pressure Cut-off	K_c	0.0	GPa

Table 3.3: Material properties used for the quartz sand grains

Properties		Quartz	Unit
Density	ρ	2648.5	Kg/m^3
Shear Modulus	G	46.92	GPa
First Shear Stress Coefficient	G_1	1.873	-
Second Shear Stress Coefficient	G_2	3.459e-10	-
Midpoint for Mean Stress Dependent Yield	Y_1	4.4	GPa
Yield with Zero Mean Stress	B	2.353	GPa
Hardness Parameter with Mean Stress Dependence	M	.667	-
Relaxation Time	T_R	3.5	ns
Bulk Modulus	K	43.19	GPa
First Order Bulk Modulus	K_1	156.2	GPa
Second Order Bulk Modulus	K_2	48.6	GPa
Gruneisen Parameter	γ_o	.675	-
Pressure Cut-off	K_c	0.0	GPa

3.4 Measures of Instability

After one penetration depth, instability can be seen qualitatively as a turning or unsymmetric deformation of the projectile in many cases. To gauge the instability, quantitative methods are required for establishing and comparing projectile instability. In this work, whenever quantities are plotted over the entire penetration event they are nondimensionalized by dividing the penetration depth by the penetrator length. Penetration depth is considered as the deepest point of penetration on the projectile, and the penetrator length refers to the initial length of the penetrator. This can become important if penetrators experience large deformations.

One measure of instability is projectile deviation from its path. If during penetration, the center of mass of the projectile shifts laterally it must have experienced a non-zero lateral force. In some cases, plots of lateral force during penetration will be presented.

A second measure of instability is characterized by projectile turning. To quantify projectile turning, the rotational momentum of the projectile was calculated throughout the simulations. The formula used to calculate the projectile rotational momentum at time t is shown in Equation 3.13

$$H_o^t = \sum_{i=1}^{i=n} (r_i^t \times m_i v_i^t) \tag{3.13}$$

where i is a node in the projectile, r is the vector connecting the projectile center of mass to node i, and m_i and v_i are the mass and velocity corresponding to node i.

A third method used to quantify projectile instability is to average the lateral forces applied on the projectile. As with projectile rotational momentum, the closer this

average is to zero, the more stable the penetration event was. The formula for calculating the average lateral forces can be seen in Equation 3.14

$$\bar{F}_x = \frac{1}{2}\sum_{i=1}^{i=n} F_{xi}(t_{i+1} - t_{i-1}) \tag{3.14}$$

where F_{xi} is the x component of the lateral force for time step i and t_i is the time at step i. It should be noted that equation 3.14 only holds for projectiles that remain nearly vertical. A projectile fired in the x direction would have a very large value of $\bar{F}_x$.

3.5 Parameters Studied

Mesoscale calculations increase tremendously the number of variables in the simulations. In solely continuum simulations, standard properties of interest are material properties. In mesoscale simulations, in addition to material properties, many other parameters influence the final simulation result. Here the focus was on the effects of the mesoscale parameters. Continuum material properties were not parametrically studied.

To understand the effects of the mesoscale properties on projectile instability, a baseline set of simulations was completed. The characteristics of these simulations were to some extent arbitrary, and are denoted as simulations 1-6 in Table 3.4. Simulations 1-3 were completed using the same sand target with three different projectile velocities. Simulations 4-6 were similar to 1-3. However, they considered a perfectly elastic penetrator in response to an interesting result found in simulations 1-3, where the projectile deformed more than expected at high velocity.

After completion of the baseline simulations, a number of variables were varied and results compared against the baseline tests. These variables were grain strength, grain size distribution, grain size, target porosity, Coulomb type inter-granular friction,

grain clustering, and the effects of random grain placement on instability. The results and more details of the simulation parameters are given in Section five.

In the present study, a number of assumptions were made. Essentially, these assumptions constitute the limitations of this work. A major assumption involves the use of a two dimensional representation of the projectile and grains for a 3-D problem. A second assumption or limitation is that thermal effects have not been included in these calculations. A third assumption or limitation is that granular failure and penetrator erosion were neglected.

Table 3.4: List of Simulations

	Grain Size	Projectile Velocity (m/s)	Projectile Type	Grain Type	Placement	Porosity	Friction (μ)		
1	42-78 μm	500	Plastic	Plastic	Regular	30%	0.3		
2	42-78 μm	1000	Plastic	Plastic	Regular	30%	0.3		
3	42-78 μm	1500	Plastic	Plastic	Regular	30%	0.3		
4	42-78 μm	500	Elastic	Plastic	Regular	30%	0.3		
5	42-78 μm	1000	Elastic	Plastic	Regular	30%	0.3		
6	42-78 μm	1500	Elastic	Plastic	Regular	30%	0.3		
7	42-78 μm	1500	Plastic	Elastic	Regular	30%	0.3		
8	42-78 μm	1500	Elastic	Elastic	Regular	30%	0.3		
9	60 μm	1500	Plastic	Plastic	Regular	30%	0.3		
10	60 μm	1500	Elastic	Plastic	Regular	30%	0.3		
11	84-156 μm	1500	Plastic	Plastic	Regular	30%	0.3		
12	84-156 μm	1500	Elastic	Plastic	Regular	30%	0.3		
13	42-78 μm	1500	Elastic	Plastic	Regular - 2	30%	0.3		
14	42-78 μm	1500	Elastic	Plastic	Regular - 3	30%	0.3		
15	42-78 μm	1500	Elastic	Plastic	Regular - 4	30%	0.3		
16	42-78 μm	1500	Elastic	Plastic	Regular - 5	30%	0.3		
17	42-78 μm	1500	Plastic	Plastic	Clustered	30%	0.3		
18	42-78 μm	1500	Elastic	Plastic	Clustered	30%	0.3		
19	42-78 μm	1500	Plastic	Plastic	Regular	40%	0.3		
20	42-78 μm	1500	Elastic	Plastic	Regular	40%	0.3		
21	42-78 μm	1500	Plastic	Plastic	Regular	30%	0.0		
22	42-78 μm	1500	Elastic	Plastic	Regular	30%	0.0		
3 Depths of penetration									
23	42-78 μm	1500	Elastic	Elastic	Regular	30%	0.3		
24	42-78 μm	1500	Elastic	Elastic	Regular	30%	0.0		
Variable mass simulations									
25	42-78 μm	1500	Elastic	Plastic	Regular	30%	0.3	Mass	Multiplied by 2
26	42-78 μm	1500	Elastic	Plastic	Regular	30%	0.3	Mass	Multiplied by 1/2

SECTION 4
Mesoscale Target Creation

Modeling of a granular media during impact loading required robust preprocessing capabilities. In these simulations each grain was modeled as a convex polygon, and each polygon was considered as its own continuum body. When constructing the grains, granular shape, grain aspect ratio, inter-granular friction, grain size, grain size distribution, porosity, and granular irregularity are important. These variables were specified and controlled in the preprocessing phase of the simulation and gave rise to additional requirements.

4.1 Overview of Mesoscale Target Development

The development of the sand generation process was conducted with the need to represent a sand target as closely as possible.

1. Grain distribution: The generation method need to produce targets containing both large and small grains [6, 49, 50].
2. Porosity: The method should be able to produce targets containing variable amounts of porosity [25, 26].
3. Random placement: grain placement needs to be random for unbiased results.
4. The grains need to be in a configuration.
5. Grain shape: the possibility of grain folding is increased if the grains are abnormally shaped or concave[51], this is not acceptable in the current simulation framework.

6. Boundary definition: Grains should be defined with straight boundary segments that are not smaller than the minimum mesh size (important for simulation efficiency).

To speed the development of the target creation software, a previously developed code at ISP for creating polycrystalline metal domains was used[52, 53]. The two main portions of the original code used for this work are the Voronoi tessellation algorithm and the Voronoi optimization algorithm. Other portions of the code are new and were written specifically for this work. What follows is a brief overview of the sand creation process used in ISP-SAND.

The production of a realistic sand domain begins with grain site (GS) and void site (VS) placement. Each GS corresponds to one grain and each VS corresponds to an area of porosity. The placement of these points affects the final grain sizes and shapes. The second process makes use of a Voronoi tessellation[54] (VT), a process that discretizes a domain containing a set of points in such a way as to encapsulate each point in a unique discrete sub domain (grain). The third process is the modification of the VT to enhance the ability to match the required grain size distribution. After modification, the sub domains corresponding to VS's are removed and the remaining sub domains corresponding to sand grains are then processed by CUBIT (Sandia mesh generation code) for meshing.

This process has been refined many times and is encapsulated in the code ISP-SAND. Initially, the process required approximately 24 hours to create targets with 20,000 grains and meshing with Cubit was not possible. Currently, the code is capable of producing a large number of sand grains (1,000,000) in a short time (2-4 hours).

Meshing has also become possible due to a batch processing technique that has been developed. In the following section, a detailed description of the sand generation process is given.

4.2 ISP-SAND

4.2.1 Initial Grain Site Placement

Grain sites are points that are used by the VT and define the locations of the individual grains. Because the placement of these sites controls grain size, shape, and porosity, the placement of GS plays a major role in the production of the target. The creation of the grain placement algorithm was facilitated by a few assumptions:

1. Grains can initially be assumed to be circles with a specified grain diameter.
2. The number of grains needed to fill a target could be found by dividing the area of the target by the area of the circular grains.
3. Placing grains in the target to minimize their radial tolerance conflicts would result in the final VT producing grains with reasonable diameters.

An initial attempt at grain placement spreads points randomly throughout the domain. The only placement criteria was on the grain diameters associated with each GS. For example, if 3 sites are placed in the domain, GS1 would be randomly placed. GS2 would be randomly placed and checked for proximity with respect to GS1. If the average of the two radii are greater than the distance (D) between the two points, then point two will be removed. If D is greater than the average radii, GS2 will be accepted. Next, GS3 will be randomly placed and proximity checked against all of the previously accepted GS. This process would be carried out until all of the grains are placed and checked. The

points which are removed would then be randomly placed again until all of the sites are placed in the domain or a specific number of placement cycles had been reached.

This process was sufficient for generating grains of comparable size. However, the process failed to accurately reproduce a grain size distribution. Another drawback of this process was that the method could only produce grains larger than those specified. Consequently, a bit of guess and check work was required to make grains of a specific size.

A second and more sophisticated process yielded the currently used method for placing points. This method uses an iterative technique to move the GS in a way that best satisfies the overall grain diameters at each point.

The first step in this process is the specification of the desired target properties: target size, grain size, and porosity. With this information, the number of GS needed to fill the domain is calculated assuming circular grains. Each site is then randomly placed throughout the target irrespective of the other grains. Porosity is addressed at this stage by adding a number of void sites (VS). The VS have diameters smaller than the mean grain size and are treated similarly to GS. The difference being that these sites represent porous area. From this point forward, no distinction will be made between grain sites and void sites and all points will be called GS.

As GS are initially randomly placed, a great deal of overlap between the grains can occur. In order to minimize this overlap, the grains are each assigned a potential function in the shape of a Gaussian[55] and incrementally moved in directions that minimize their tolerance conflicts (overlap). The process is outlined as follows.

- Distance Checking: GS1 is checked for proximity with every other site.

- Gaussian Assignment: If a GS is closer than the average radii of the two points then a tolerance conflict value is calculated as follows.

A Gaussian function is assigned to GS1 and is used to scale the magnitude of the GS displacements. Figure 4.1 shows a 2-D representation of the Gaussian

- function where the radius of the Gaussian function is determined by the average of the two grain diameters. The point labeled GS2 is the point which is encroaching upon GS1. The Gaussian function is defined in Equation 4.1

$$G = e^{-\frac{1}{2\sigma^2}\left(\frac{2\pi\sqrt{(x_i-x_j)^2+(y_i-y_j)^2}}{r_i+r_j}\right)^2} \tag{4.1}$$

where σ^2 is the variance, assumed here to be 1. x_i, y_i, x_j, y_j correspond to the spatial location of the points being checked while r_i and r_j are the grain radii assigned to the two points. It can be seen from Equation 4.1 that if the two points one on top of another, G will equal 1. If the points are perfectly separated (their separation matches their combined radii) then G will equal 2.6×10^{-9}.

- The direction that will most rapidly minimize the tolerance conflict between the grains is found by taking the gradient of the Gaussian surface which gives the direction of steepest descent[55]. The gradient of the Gaussian is calculated at the location of the encroaching GS using Equations 4.2 and 4.3.

$$\frac{\partial G}{\partial x} = \frac{-(x_1-x_2)\exp(-\frac{\sqrt{(x_1-x_2)^2+(y_1-y_2)^2}}{2\sigma^2})}{2\sqrt{\pi((x_1-x_2)^2+(y_1-y_2)^2\sigma^2}} \tag{4.2}$$

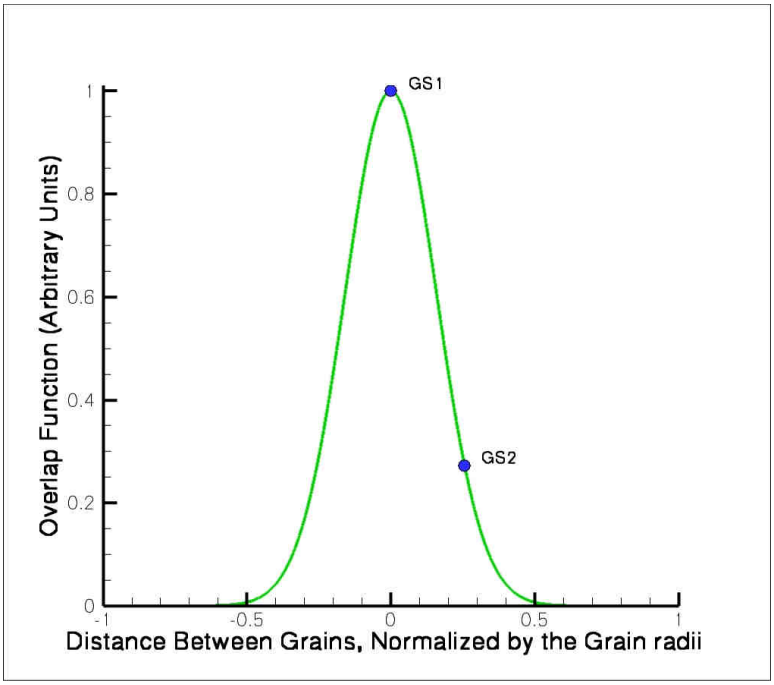

Figure 4.1: 2-D Gaussian function centered at GS1 and showing overlapping GS2.

$$\frac{\partial G}{\partial y} = \frac{-(y_1 - y_2)\exp(-\frac{\sqrt{(x_1 - x_2)^2 + (y_1 - y_2)^2}}{2\sigma^2})}{2\sqrt{\pi((x_1 - x_2)^2 + (y_1 - y_2)^2\sigma^2}} \quad (4.3)$$

- The direction vectors are then converted into unit vectors. This vector is then scaled by the previously calculated magnitude of the Gaussian and stored for future use as a conflict vector.

- Loop through each point: This process is repeated until the conflict vectors for each point have been calculated. GS with more than one conflict vector have their vectors summed together to produce a composite conflict vector that gives the direction that will minimize GS overlap.
- Normalize: At this stage of the process, each GS has a vector assigned to it that will define the direction and the relative magnitude of the GS displacement. Prior to displacing the grains the vectors must be normalized as they were defined irrespective to any scale. To do this, the vector with the maximum magnitude is found and used as a scaling factor for the displacement of all other grains. After scaling, the vector magnitudes are all less than or equal to one. These vectors are again scaled to incorporate the length scale of the problem. This final scaling factor is 1/100 of the average grain diameter.
- Displacement: GS are displaced according to their displacement vectors.
- Iterate: The entire process is then repeated until the system reaches a local minimum overlap value.

Snapshots of this process are shown in Figure 4.2 through Figure 4.5. These figures show the GS after progressively more displacement iterations. The arrows denote the direction in which the points will be displaced and are proportional to the magnitude of the displacement. By the 100^{th} iteration, an obvious structure can be seen. The domain shown in these figures was specified to have 30% porosity. The porosity is manifested as the clusters of GS interspersed with the larger GS.

Because grain placement is an explicit process (stepping forward), the size of each step is important. If the points are moved a large distance (corresponding to a large final scaling factor) in one iteration, they will not converge to a local minimum. However, if the points are moved too small a distance, the number of steps to convergence will grow and increase the run time of the code.

Figure 4.6 is a plot of overlap magnitude versus iterations, and illustrates convergence behaviors of different step sizes. Each step size corresponds to the mean grain diameter multiplied by a scaling factor. Once the optimum scaling factor is determined, it can be used for a domain containing grains of any diameter. The pink line corresponds to the largest step size tested and demonstrates that convergence will not occur when the scaling factor becomes too large. The lack of convergence is expected as grains will not be able to take the gradual steps to convergence. Instead, they will be moved with large displacements that do not minimize the tolerance conflicts between grains. As the scaling factor decreases, the energy converges quickly in less than 100 steps. As expected, when the step size is decreased further, the overlap continues to converge, but requires many more steps. Figure 4.6 shows that a scale factor ranging between 1 and 0.1 produces the fastest convergence.

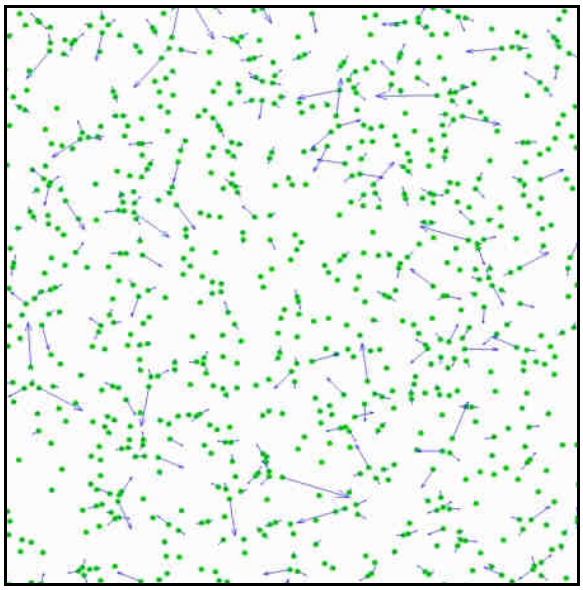

Figure 4.2: Grain sites shown after initial overlap checking. Vectors represent the direction of displacement.

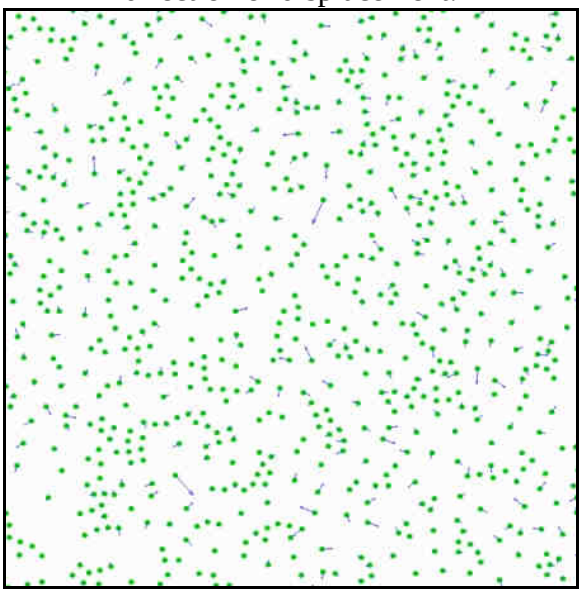

Figure 4.3: Grain sites shown after 20 displacement iterations.

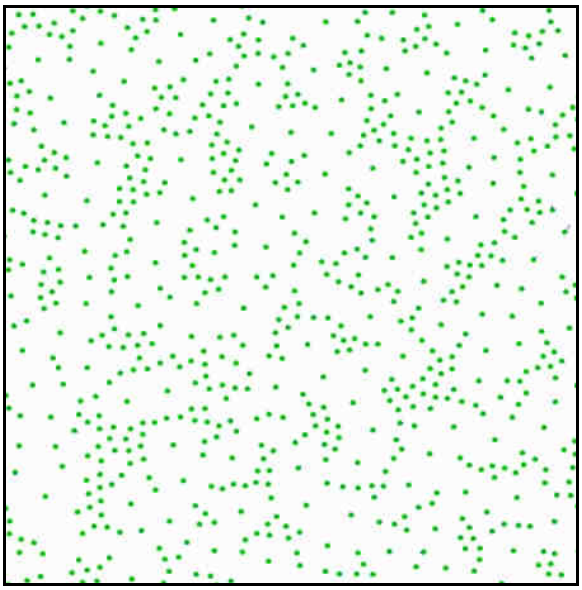

Figure 4.4: Grain sites shown after 40 displacement iterations.

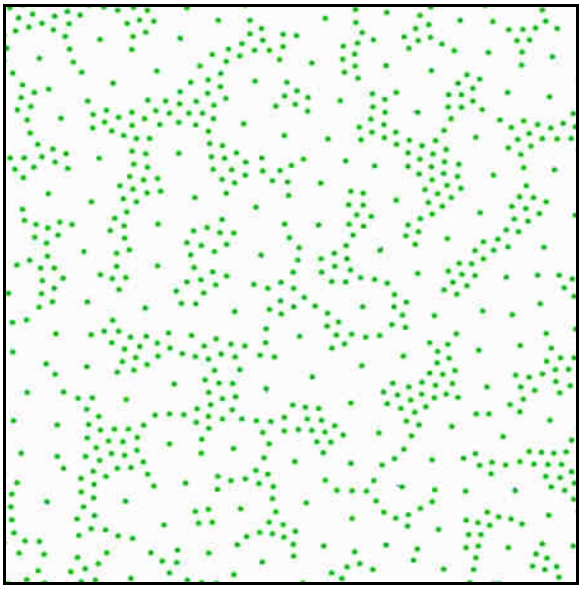

Figure 4.5: Grain sites shown after 100 displacement iterations. Patterns can now clearly be seen in the grain sites.

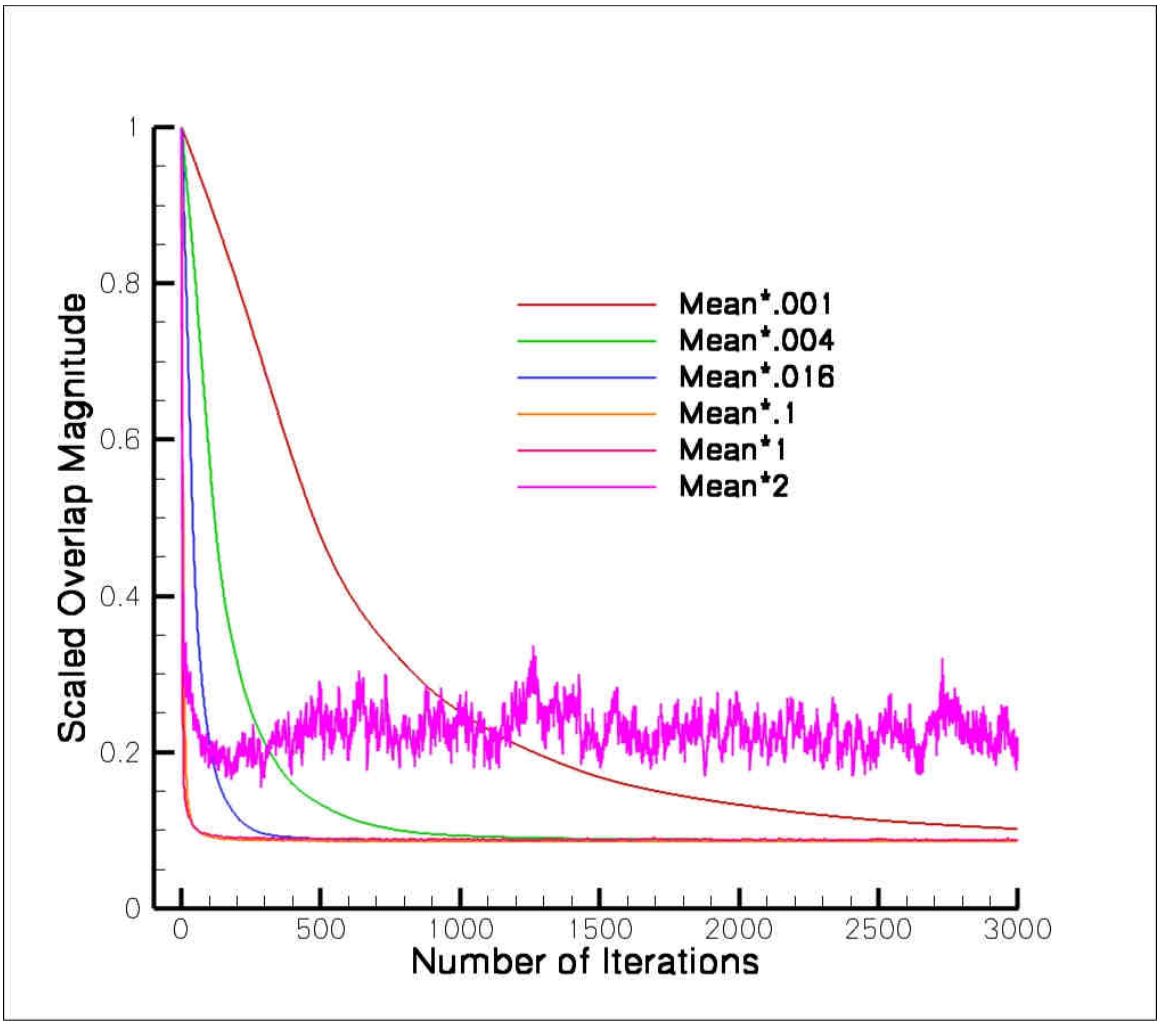

Figure 4.6: Overlap energy as a function of iterations. Each line shows different maximum step sizes which correspond to the mean grain size multiplied by a scaling factor. As step size increases, the convergence rate increases until a point at which convergence no longer occurs.

Because GS greater than their average diameter apart do not interact, a significant performance increase can be attained by selectively checking for tolerance conflicts. A minimal checking option was created to segment the target into several smaller domains. Segmenting the target enables the large domain to be bisected into smaller domains which have an edge length equal in size to that of the maximum grain diameter. When bisecting the domain in this manner, points need only be checked against sites located within their specific domains and with the sites in adjacent domains (Figure 4.7). The orange colored box contains sites being checked for tolerance conflicts and the green boxes contain points which can possibly interact with those in the orange box.

To demonstrate the increase in speed, 356 GS and 1485 void sites were subjected to 1000 iterations. When the selective checking algorithm was implemented the domain was segmented into 169 small domains and ran for approximately 17 seconds. Without selective checking the algorithm ran for 194 seconds, an increase of nearly 11.5 times. This difference in run time is dramatic and increases with the number of GS that are placed. One unfortunate property of this type of domain sorting is that with increasing grain size distribution, the improvements are diminished as sub-domains must not be smaller than the largest grain radii.

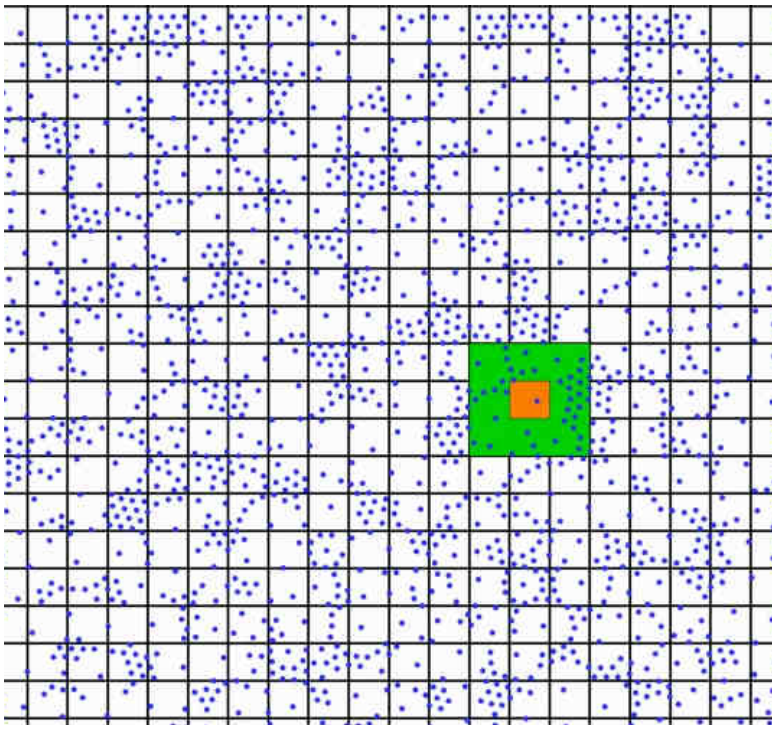

Figure 4.7: Large domain segmented into smaller sub domains. The orange box contains points that are being checked and the green boxes contain points that can interact with the points in the orange box.

4.2.2 Modified Voronoi Tessellation

The second major process in the generation of the sand grains uses a VT. A VT is a process that can be used to bisect a space into a set of unique subspaces[54]. Figure 4.8 shows a simple schematic of the tessellation process. In Figure 4.8 A the grains sites that are to be tessellated are displayed. In this schematic view only the site located in the center will be tessellated. The initial step in the tessellation determines the nearest sites relative to the site being tessellated (see Figure 4.8B). Next, bisecting lines are created at the midpoints between the center site and the contributing sites as seen in Figure 4.8C. These bisecting lines and their intersections, called Voronoi points (VP) make up the tessellation of the center grain which, in this case, takes the form of the octagon in Figure 4.8E. This process can be performed on any arrangement of points with the only restriction being that the points do not lie directly upon one another.

Figure 4.9 shows the tessellation of the GSs in Figure 4.5 and demonstrates the capability of the tessellation process. The tessellation shown in Figure 4.9 contains grains sites as well as void sites and highlights one aspect of the VT that is not desirable. Due to the way in which the Voronoi tessellation is produced (perpendicular bisectors), there is an averaging effect between bordering large and small grains. When a small cell is in contact with a large cell the two are distorted so that the large cell loses area and the small cell gains area. In order to minimize this effect, the tessellation goes though an augmentation process which relocates the Voronoi points to best match the surrounding GS tolerances.

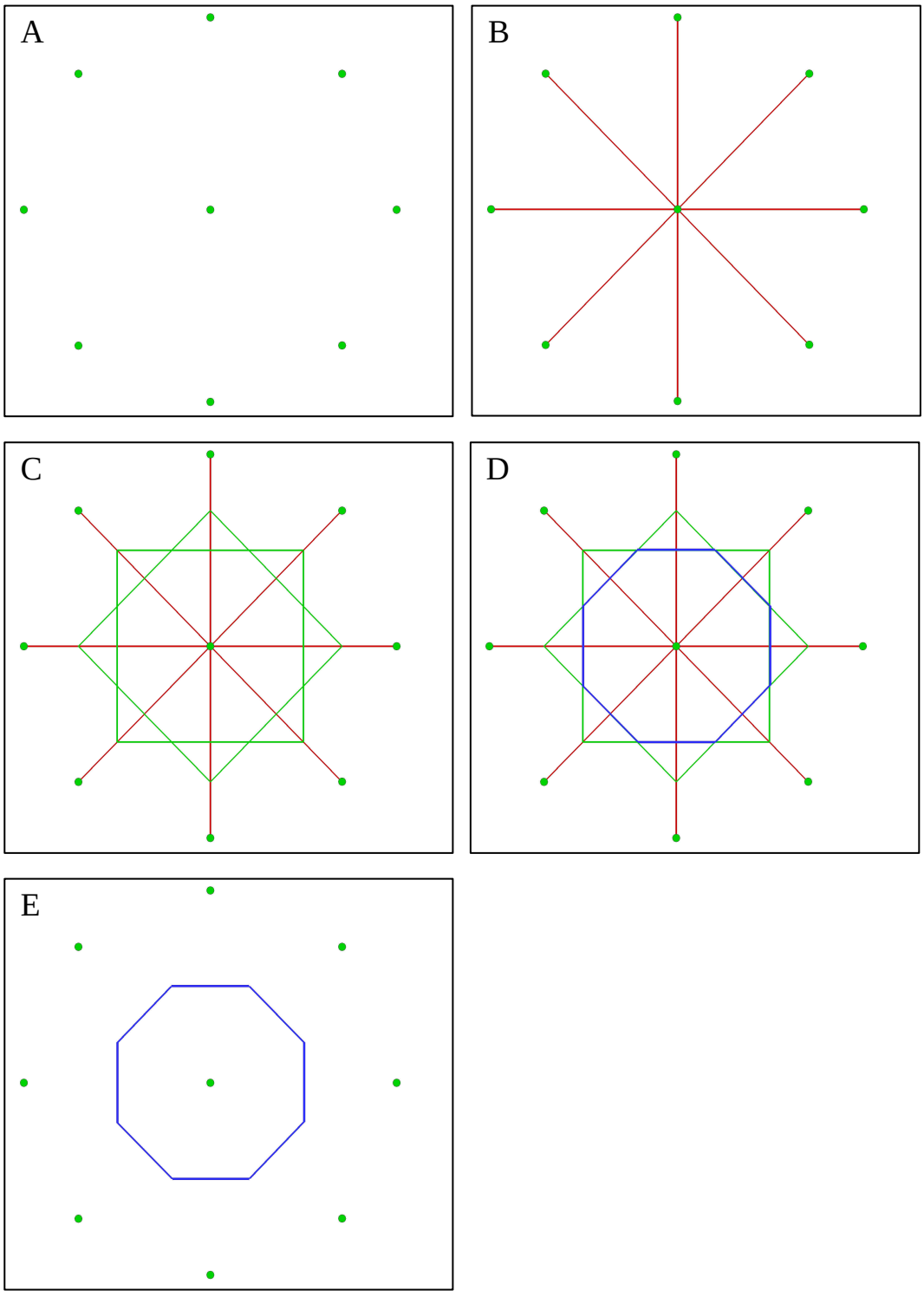

Figure 4.8: Schematic of steps used to produce a Voronoi tessellation. A: Points that will be tessellated, B: Neighbor search to define contributing points, C: Bisection of lines connecting contributing points. D: Location of bisector intersections, E: Final tessellation

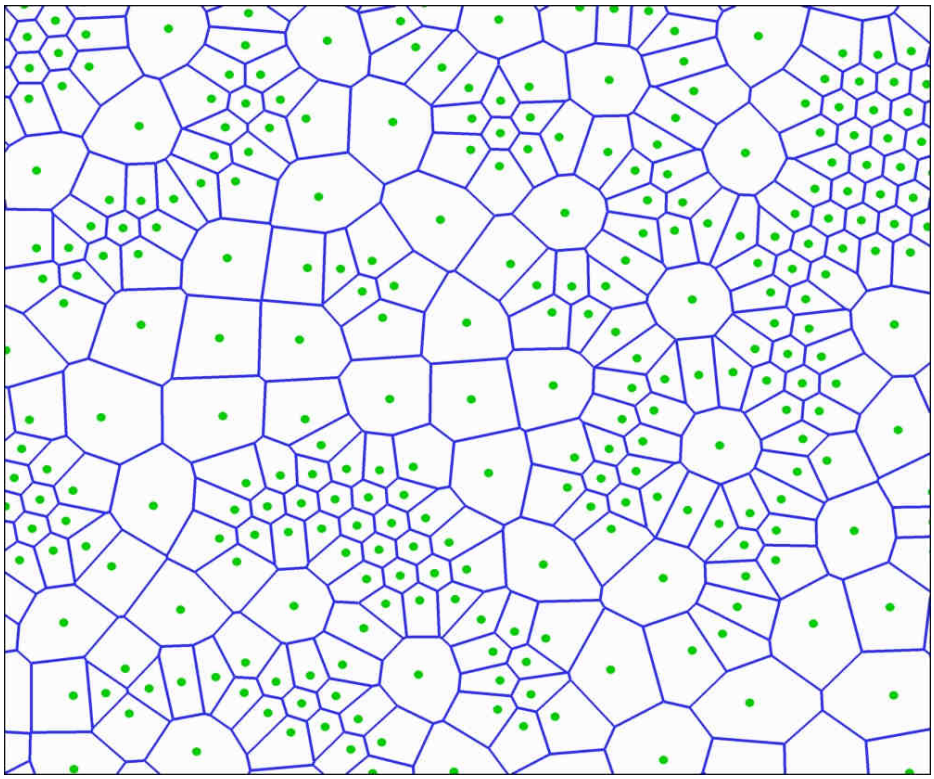

Figure 4.9: VT of sites generated with ISP-SAND. Dots represent the sites and the lines represent the VT. In this domain, the small sub zones will be removed to yield a porous sample. Notice that the tessellation has an averaging effect on the grain size. Grains and voids that border one another have been distorted in a way that decreases the grain size and increases the void size.

The augmentation is carried out with an iterative approach that converges to a minimum residual error. Figure 4.10 shows the difference between the Voronoi tessellation (green) and the post augmentation tessellation (blue). In this case, GS1 was assigned a smaller radius during point placement than GS2 and GS3. However, because a tessellation is created irrespective of the point radii the Voronoi cells are distorted and not of the correct size. The process to enforce the grain radii is as follows:

- The association between each GS and VP are found. In Figure 4.10, the VP is associated with GS1, GS2, and GS3 because it lies on the boundaries of their Voronoi cells.
- The distance D between each GS and the VP are checked against the grain site radii to produce error terms for each GS and VP pair. The error term E between GS1 and the VP is displayed in Equation 4.4,

$$E_{GS1-VP} = \sqrt{(GS1_x - VP_x)^2 + (GS1_y - VP_y)^2} - r_{GS1} \quad (4.4)$$

  where the subscripts denote the x and y coordinate of the points.
- A unit vector parallel to a line connecting the VP and GS is created and scaled by the error term E.
- The error vectors created for each VP are added together and the final error vector is non-dimensionalized by the minimum grain diameter multiplied by .01.
- Each VP is then moved according to the corresponding composite error vector.
- The process of moving this point is repeated until the error vector becomes approximately 0 denoting a minimum error between all the surrounding GS and the VP.
- The process is then repeated for each VP.

The end result of this process can be seen in Figure 4.11. In this augmented tessellation, grain sites as well as void sites are easily distinguishable and match the input diameters reasonably well (to be demonstrated later).

Two difficulties were discovered with the augmentation process. First, the process is capable of producing overlapping grains. This problem was simply solved by combining the two overlapping points and submitting the new site to the augmentation algorithm. Second is the issue of concave grains. Concavity can be found in real sand grains [49, 50] and increases the likelihood of a grain folding upon itself [51]. This cannot currently be simulated with ISP-TROTP. This problem is addressed by simply removing the point causing concavity from the target. The result of this is straight faces where the concave portions previously occurred. This simple solution works well when concavity is minimal. However, strangely shaped grains can be produced when concavity is extreme. In this process, concavity is associated with the breadth of the size distribution between placed points and can be minimized by keeping the size difference between GS and VS relatively small. Void sites that are ¼ the size of the grains produce reasonable porosity results. As can be seen in Figure 4.11, concavity does not appear, even when grains are surrounded by voids 25% of their size.

As with the GS placement in the previous step, the tessellation process can be made more efficient by only considering the points closest to the point being tessellated. To implement this strategy, the same approach is taken as in the grain placement algorithm of dividing the domain into a set of smaller domains. The sizing of these domains is not as straightforward as in the grain placement process. This is because there is not an exact criterion for point interaction. Points which may interact in the

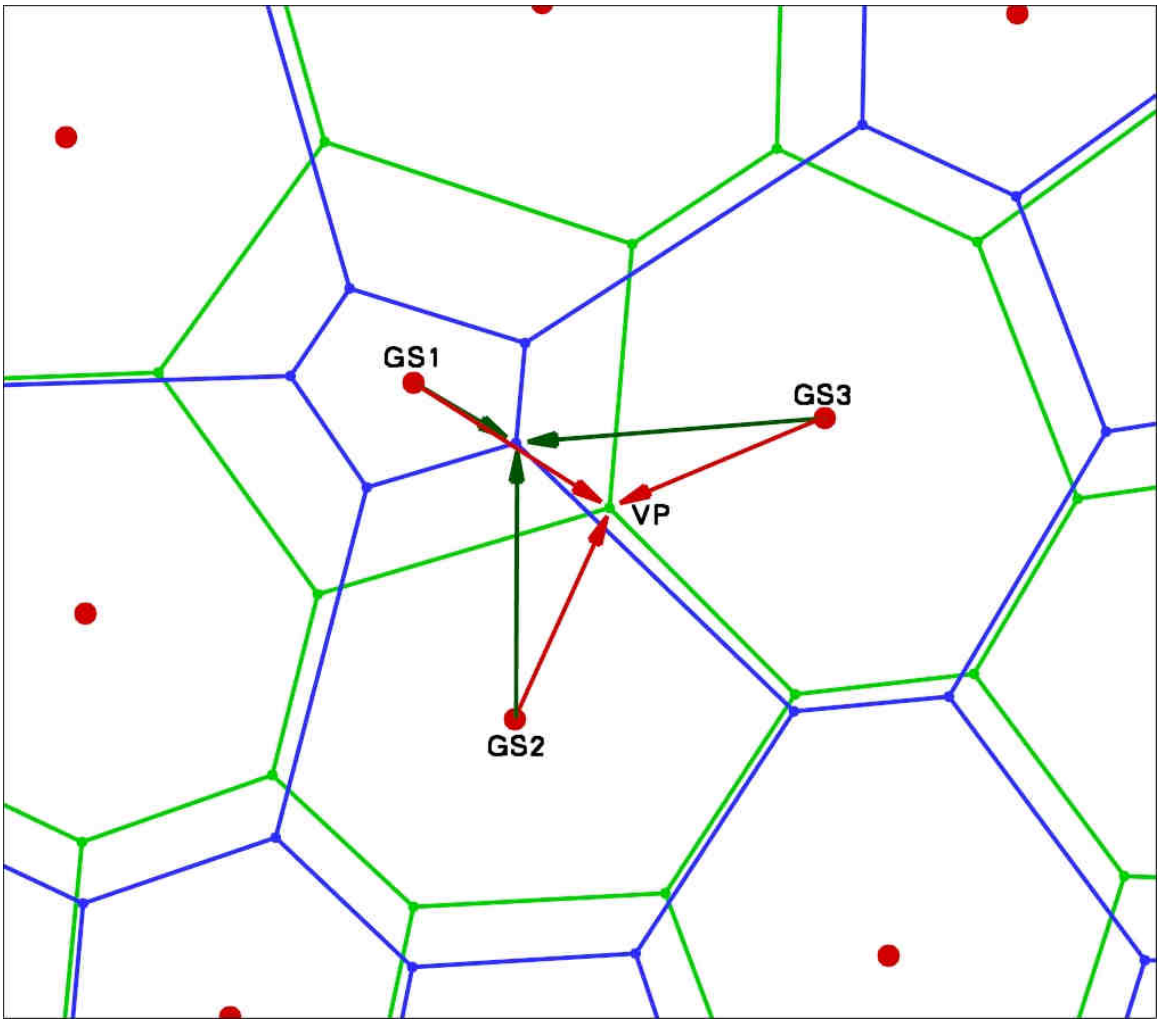

Figure 4.10: Optimization of Voronoi tessellation. The VP is shifted to minimize the difference between the assigned radius of the GS and the distance between the GS and the VP.

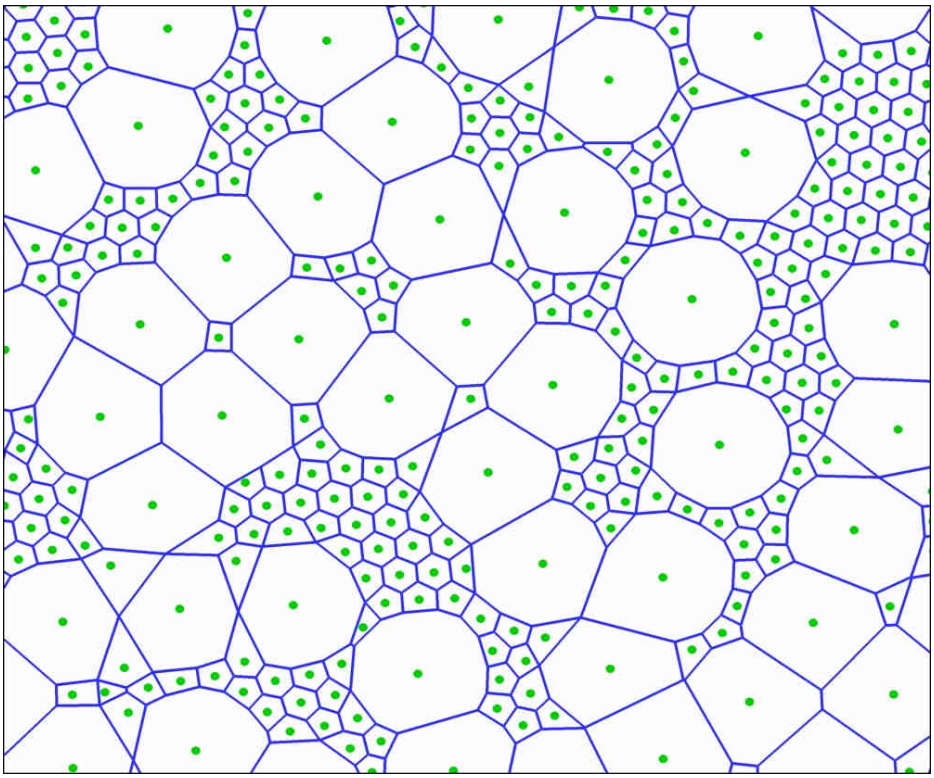

Figure 4.11: Modified VT of sites generated with ISP-SAND. Grain and void sites are clearly visible. Grain sites are expanded to their assigned diameters and void sites have been condensed to their assigned diameters.

tessellation could be farther away than their average grain diameters. To ensure an adequate sub domain size, the sub domains were given dimensions twice the size of the largest grain diameter. To validate the adequacy of the sub domain size, a number of cases were run comparing tessellations with and without the smaller sub domains. Each case was found to yield the same tessellation. This algorithm increased the speed of tessellation immensely. For example, when a tessellation of 3,183 uniform sized grains was completed, the tessellation which divided the domain created 576 boxes and took 5 seconds. The undivided domain took approximately 180 seconds. The necessity of this optimization grows with the number of grains being tessellated. The sub domain size is dependent upon the largest grain in the domain. Unfortunately, the algorithm effectiveness diminishes with increased grain size distribution or with a small number of large grains in the domain.

With the tessellation phase completed the void grains are removed from the target, and VP that are closer together than that the desired mesh size are combined. Combining points is a necessary step to ensures that the finite element mesh will not be excessively small in any location. After these two steps, the sand generation is complete and ready for mesh generation.

4.2.3 Mesh Generation

These simulations used constant strain triangles which were created in one of two ways. If a course mesh was desired, a simple algorithm was used which connected the centroids of the grains to each of their associated VPs, as shown in Figure 4.12. This can produce mesh elements that are elongated wedges if the grain has more than six divisions

around its circumference or is distorted. If a refined mesh was desired, Sandia National Laboratories code Cubit 9.1 was used. Initially, meshing with Cubit was found to be slow (possibly greater than 24 hours for 20,000 grains) and unreliable (caused the workstation to crash). However, a substantial speed increase was achieved by meshing each grain individually and disabling Cubits display window. This process was completed by creating a script file for each grain. These script files were then executed in Cubit and produced a small mesh file for each sand grain. The small files are then processed and combined to create the final mesh. Meshing in this way enables Cubit to complete a job of 20,000 grains in approximately 1 hour and also gives it the ability to create meshes with millions of elements. An added benefit is that numerous copies of cubit can work on the same sand target, enabling the efficient use of a multi-core workstation. A mesh produced in this manner is displayed in Figure 4.13.

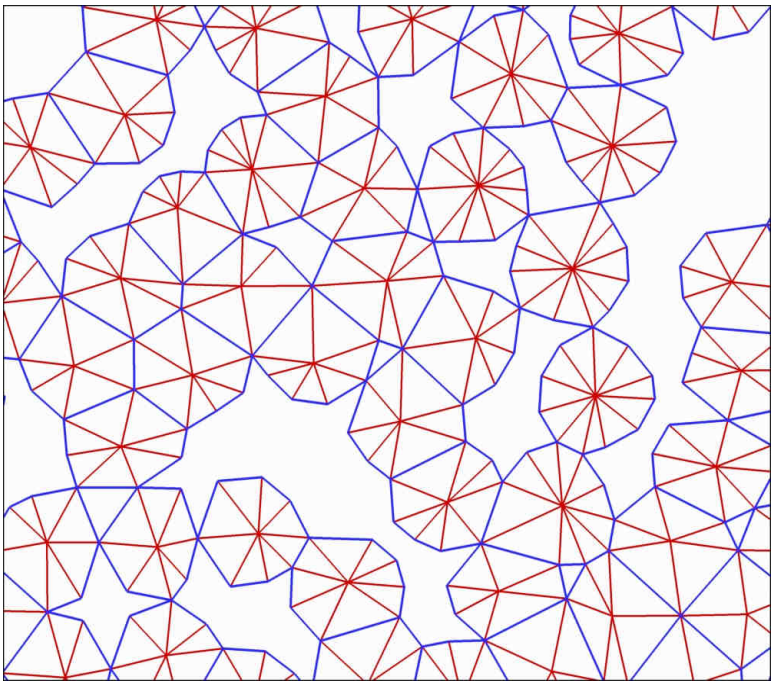

Figure 4.12: Mesh produced by connecting VPs to grain centers of area.

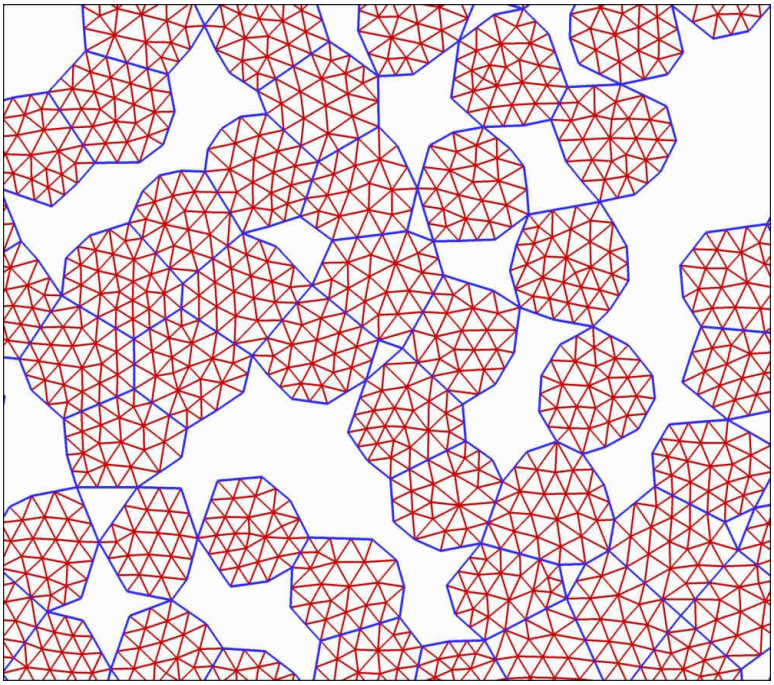

Figure 4.13: Tridelaunay mesh created using Cubit 9.1.

4.2.4 Process Validation

Due to the complexity of the process described above, it is necessary to compare the initial specifications for the target with those produced in the finished product. The two parameters that were initially specified were the grain size and target porosity. Grain size is found by calculating the area of the grain and making the approximation that the grain is equiaxed [56]. This allows for the diameter of the grain to be calculated using the simple area of a circle equation $D = \sqrt{\frac{4A}{\pi}}$. Target porosity is calculated by subtracting the total area of the grains from the rectangular target area as follows in Equation 4.5

$$p = \frac{A_T - A_G}{A_T} \tag{4.5}$$

where A_T is the area of the target and A_G is the combined area of the grains.

One test to demonstrate the code capability was to input a uniform grain size and a specified porosity value. In this case, a grain diameter of 60μm and a porosity of 30 percent were used with the over all target size specified as a 5mm by 5mm box. The finished target contained 6189 grains and a porosity of 30.32 percent. The mean diameter of the grains was 59.87, and the grain size distribution is shown in Figure 4.14. The distribution shown in Figure 4.14 has a standard deviation of 1.73μm assuming that a normal distribution, about 68%[55] of the grains, lie within plus or minus 1.73μm of the mean diameter. The sand grains produced in this test can be seen in Figure 4.15.

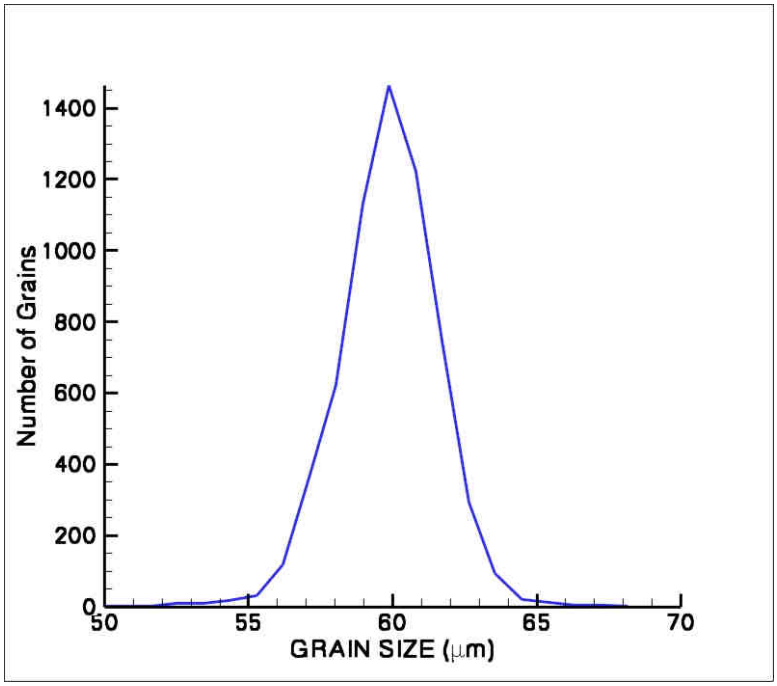

Figure 4.14: Grain size distribution for input of 60μm grain size. The mean grain size is 59.87 and shows close correspondence to input parameters.

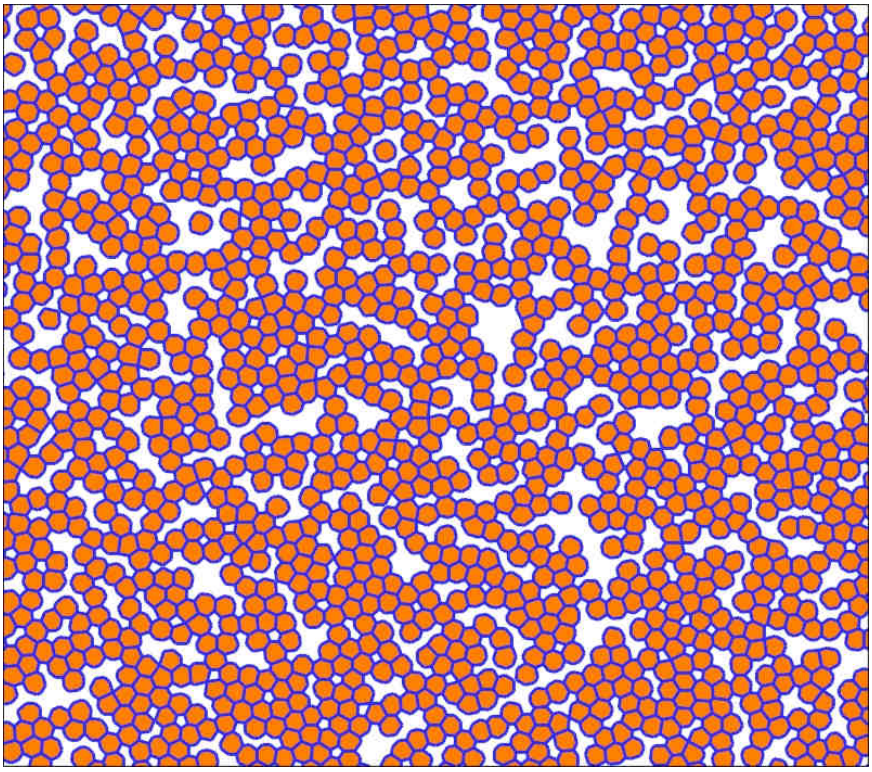

Figure 4.15: 60μm uniform grains

A second test of the validity involves a target with a distributed sand size. In this example, the porosity is again specified as 30 percent but instead of specifying a constant grain size, grains ranging in diameter from 45 – 75 μm are specified. The finished 5mm by 5mm target contained 6189 grains and had a porosity of 29.84 percent. When the grain sizes were calculated, the distribution shown in Figure 4.16 was produced. The grain size distribution had a standard deviation of 8.7 from the mean diameter of 60.07μm, which as expected, is much larger than the uniform grain size standard deviation. The sand grains in this target can be seen in Figure 4.17.

The above two tests demonstrate that for targets with 30% porosity and moderate grain size distributions, ISP-SAND produces targets with correct grain sizes and porosities.

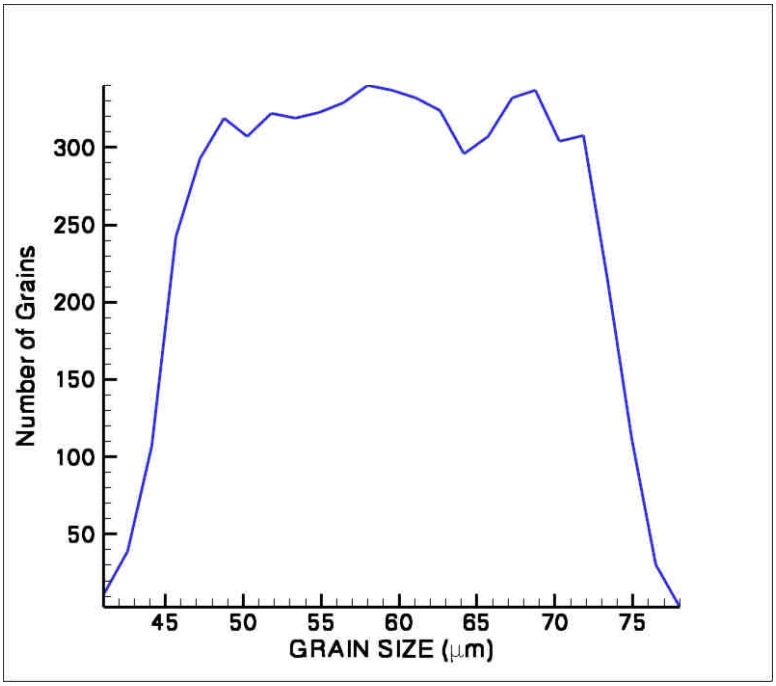

Figure 4.16: Grain size distribution for input of 45 -75um grain size. The mean grain size is 60.07um and shows close correspondence to input parameters

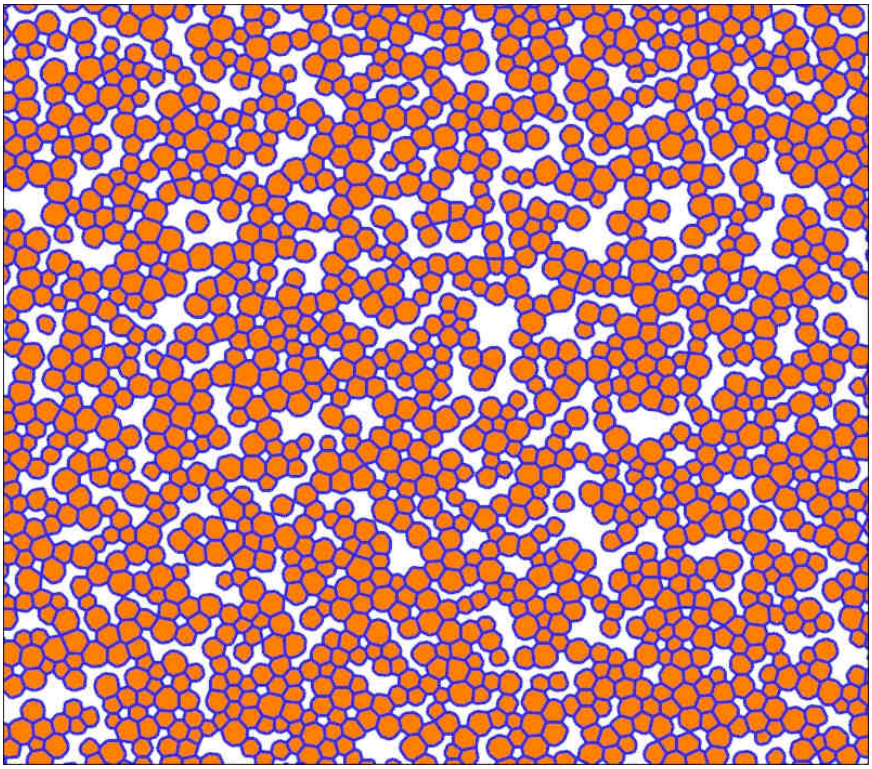

Figure 4.17: Grains ranging in size from 45 – 75 um

4.2.5 Regular and Irregular Grain Placement

Experimental characterization of sand samples can produce data on grain size and sample porosity[56]. These two properties are bulk parameters and can be satisfied by an infinite number of sand grain layouts. Without any modifications, ISP-SAND produces targets with grains that are clustered together producing relatively large concentrations of grains surrounded by large porous regions as can be see in Figure 4.15 and Figure 4.17. To study the effects of targets with less grain clustering, a small change was made to ISP-SAND. The addition was made to the grain placement algorithm and it changed the way in which grains were placed in the target. In the standard technique, grains were initially placed randomly throughout the target. When the change was implemented, the target was divided into N subsections where N is the number of grains. Within each subsection, one grain was randomly placed and V/N void sites were placed where V is the number of void sites. If the target could not be divided evenly, extra points were randomly placed in the target.

When this change was implemented, grains still satisfied the bulk distribution and porosity parameters but were more dispersed than before. A test case is shown here with the same parameters as given previously with 45-75 μm grains. The grain size distribution in the 5mm by 5mm target can be seen in Figure 4.18 and compares closely to the distribution shown in Figure 4.16. The target was calculated to have a porosity of 29.5% and a mean grain size of 60.19μm. The standard deviation of this distribution is 8.6μm which is close to the standard deviation in the non distributed grains. Figure 4.19 shows the actual grains that were produced. Comparing Figure 4.19 with Figure 4.17 shows that grains are more evenly spread and large clusters of grains no longer occur.

Grains produced when this algorithm was implemented will be referred to as regular grains otherwise the grains will be referred to as clustered.

4.2.6 ISP-SAND Conclusion

ISP-SAND was tested and it demonstrated the ability to produce large numbers of grains (in excess of 1,000,000) that can reproduce input grain sizes and porosities. ISP-SAND can produce different grain layouts in which grains can either be clustered or evenly spread throughout the target. By changing the initial random seed used in the grain placement algorithm, the code is able to produce an infinite number of different targets with relatively similar bulk parameters.

4.3 Projectile Properties

The projectile used in the simulations, shown in Figure 4.20, was a tip modified 3.5 caliber radius head (CRH)[35] tangent ogive[34] projectile with a l/d ratio of 3.85. The tip of the projectile is modified so that $\theta = 60^{o}$. This modification was completed to limit the deformation at the projectile tip. Similar modifications can be seen in the literature[57, 58]. The projectile, like the grains, was meshed using Cubit 9.1. A number of different meshing schemes were compared and Tridelaunay was determined to be optimal. This assertion was made as no mesh biasing and only minimal mesh seams (two seams can be seen formed at the back end of the projectile) were produced. The mesh used on the projectiles is the same size as that used on the grains and consists of triangles with edge lengths of approximately 10μm.

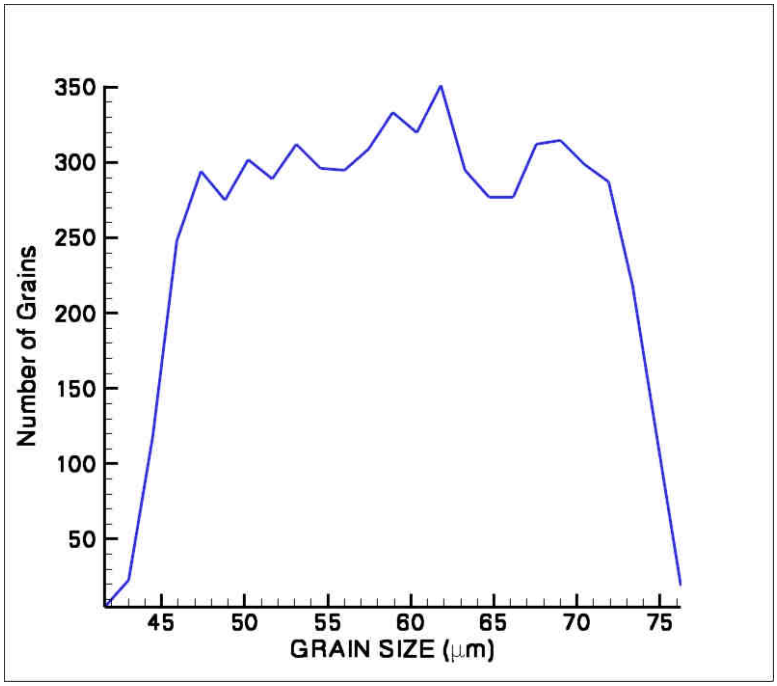

Figure 4.18: Grain size distribution for input of 45-75μm grain size. These grains were placed initially in a more normal way than those seen in previous tests.

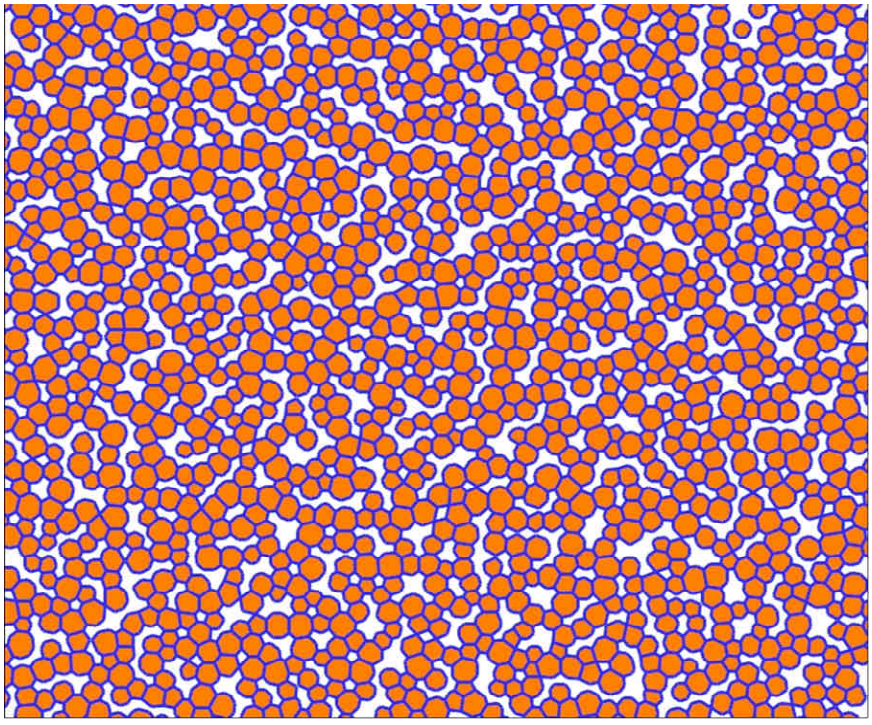

Figure 4.19: Grains ranging in size from 45-75 μm with more homogeneous porosity and grains.

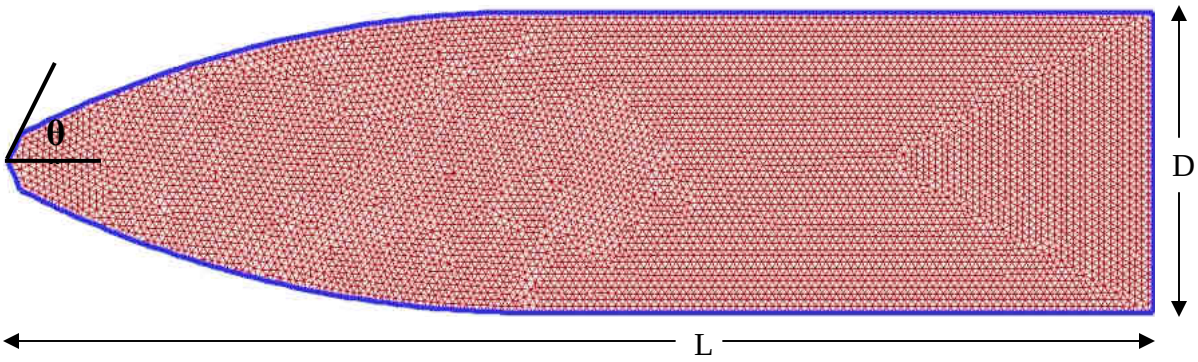

Figure 4.20: Tangent ogive projectile with 10um triangular mesh.

SECTION 5
Results and Discussion

This section displays and discusses the results from the numerical simulations. In most cases, snap shots of the penetrator and surrounding sand grains will be displayed after one full depth of penetration. These plots will be discussed and the important features found in them will be described. Plots of the instability parameters calculated during the penetration will be displayed and the various differences seen between simulations will be highlighted. For each simulation the average lateral force applied to the projectile and the final x displacement for the projectile are displayed in Table 5.1

5.1 1-3 Baseline Simulations (inelastic grains, plastic impactor at three velocities)

The baseline simulations, 1-3, considered elastic-plastic projectiles and inelastic sand grains. The targets were all identical and had a porosity of approximately 30%. Sand grains ranged in size between 45-75μm. Inter-granular friction was implemented using a Coulomb friction law with a coefficient of μ=.3. Snapshots of these simulations at one depth of penetration (except the 1000 m/s case) are shown in Figure 5.1 and Figure 5.2. These figures show the same three simulation results with different contour values being displayed. The 1000 m/s simulation did not achieve a full depth of penetration due to a contact problem in ISP-TROTP. It is shown at its deepest penetration prior to the contact problems (approximately 60% of one penetration length).

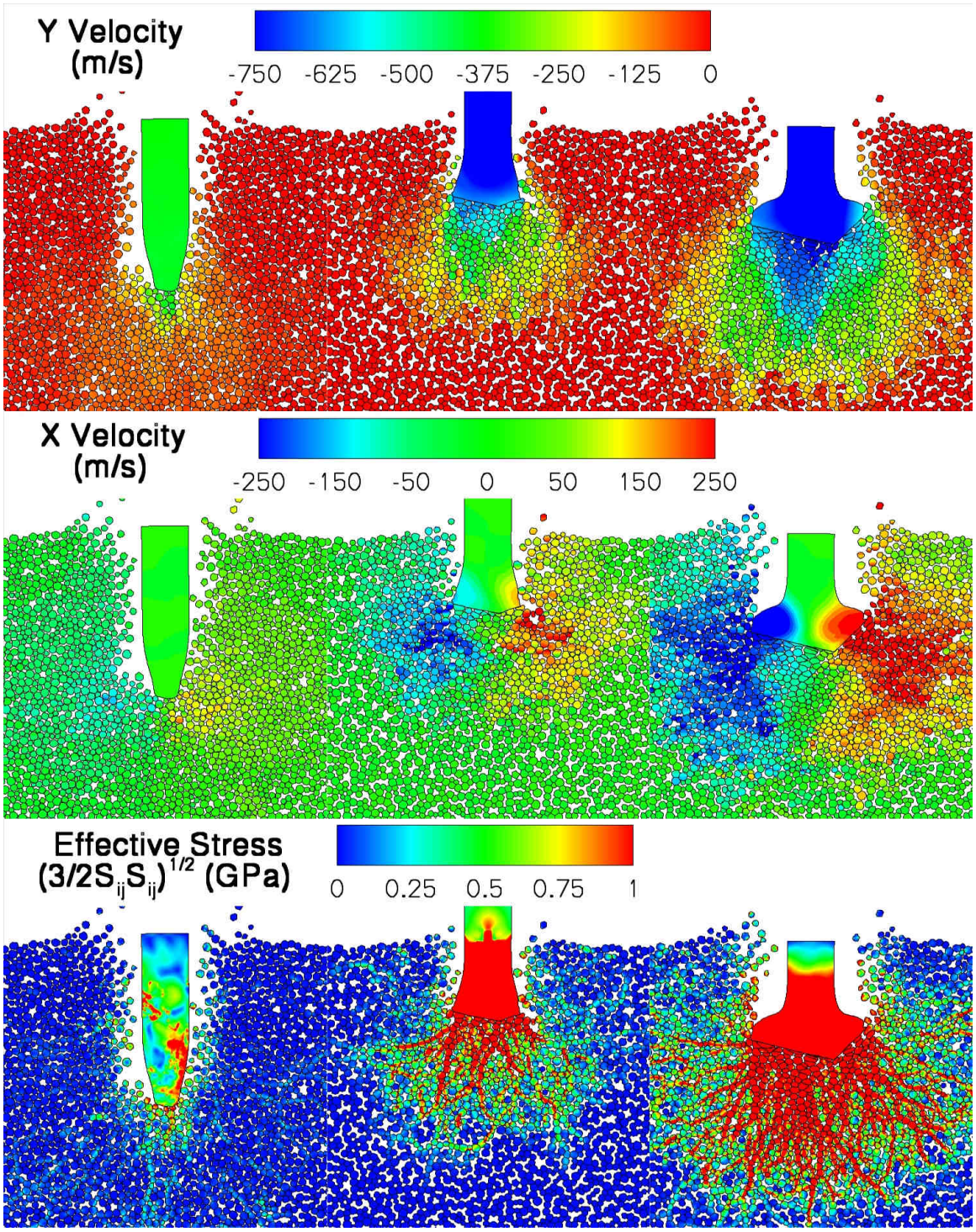

Figure 5.1: Plastic penetrator entering inelastic grains at, left 500 m/s, center 1000 m/s, right 1500 m/s. Showing contours of Y velocity, X velocity, and effective stress.

Table 5.1: List of simulations displaying average lateral forces and final x displacements.

	Grain Size	Projectile Velocity (m/s)	Projectile Type	Grain Type	Placement	Porosity	Friction (μ)	Average Lateral Force (N)	x Diplacement (mm)
1	42-78 μm	500	Plastic	Plastic	Regular	30%	0.3	2950	0.0053
2	42-78 μm	1000	Plastic	Plastic	Regular	30%	0.3	-38800	-
3	42-78 μm	1500	Plastic	Plastic	Regular	30%	0.3	-35390	0.0055
4	42-78 μm	500	Elastic	Plastic	Regular	30%	0.3	2850	0.0003
5	42-78 μm	1000	Elastic	Plastic	Regular	30%	0.3	-19650	0.0004
6	42-78 μm	1500	Elastic	Plastic	Regular	30%	0.3	-58630	0.0054
7	42-78 μm	1500	Plastic	Elastic	Regular	30%	0.3	105000	0.0062
8	42-78 μm	1500	Elastic	Elastic	Regular	30%	0.3	11240	0.0013
9	60 μm	1500	Plastic	Plastic	Regular	30%	0.3	25980	0.0062
10	60 μm	1500	Elastic	Plastic	Regular	30%	0.3	102200	0.0157
11	84-156 μm	1500	Plastic	Plastic	Regular	30%	0.3	67350	0.0126
12	84-156 μm	1500	Elastic	Plastic	Regular	30%	0.3	63800	0.0176
13	42-78 μm	1500	Elastic	Plastic	Regular - 2	30%	0.3	17720	0.0035
14	42-78 μm	1500	Elastic	Plastic	Regular - 3	30%	0.3	-73590	0.0020
15	42-78 μm	1500	Elastic	Plastic	Regular - 4	30%	0.3	41660	0.0045
16	42-78 μm	1500	Elastic	Plastic	Regular - 5	30%	0.3	37950	0.0039
17	42-78 μm	1500	Plastic	Plastic	Clustered	30%	0.3	-23670	0.0094
18	42-78 μm	1500	Elastic	Plastic	Clustered	30%	0.3	-130700	0.0147
19	42-78 μm	1500	Plastic	Plastic	Regular	40%	0.3	56280	0.0054
20	42-78 μm	1500	Elastic	Plastic	Regular	40%	0.3	-30890	0.0012
21	42-78 μm	1500	Plastic	Plastic	Regular	30%	0.0	46200	0.0035
22	42-78 μm	1500	Elastic	Plastic	Regular	30%	0.0	13510	0.0001
3 Depths of penetration									
23	42-78 μm	1500	Elastic	Elastic	Regular	30%	0.3		
24	42-78 μm	1500	Elastic	Elastic	Regular	30%	0.0		
Variable mass simulations									
25	42-78 μm	1500	Elastic	Plastic	Regular	30%	0.3	Mass	Multiplied by 2
26	42-78 μm	1500	Elastic	Plastic	Regular	30%	0.3	Mass	Multiplied by 1/2

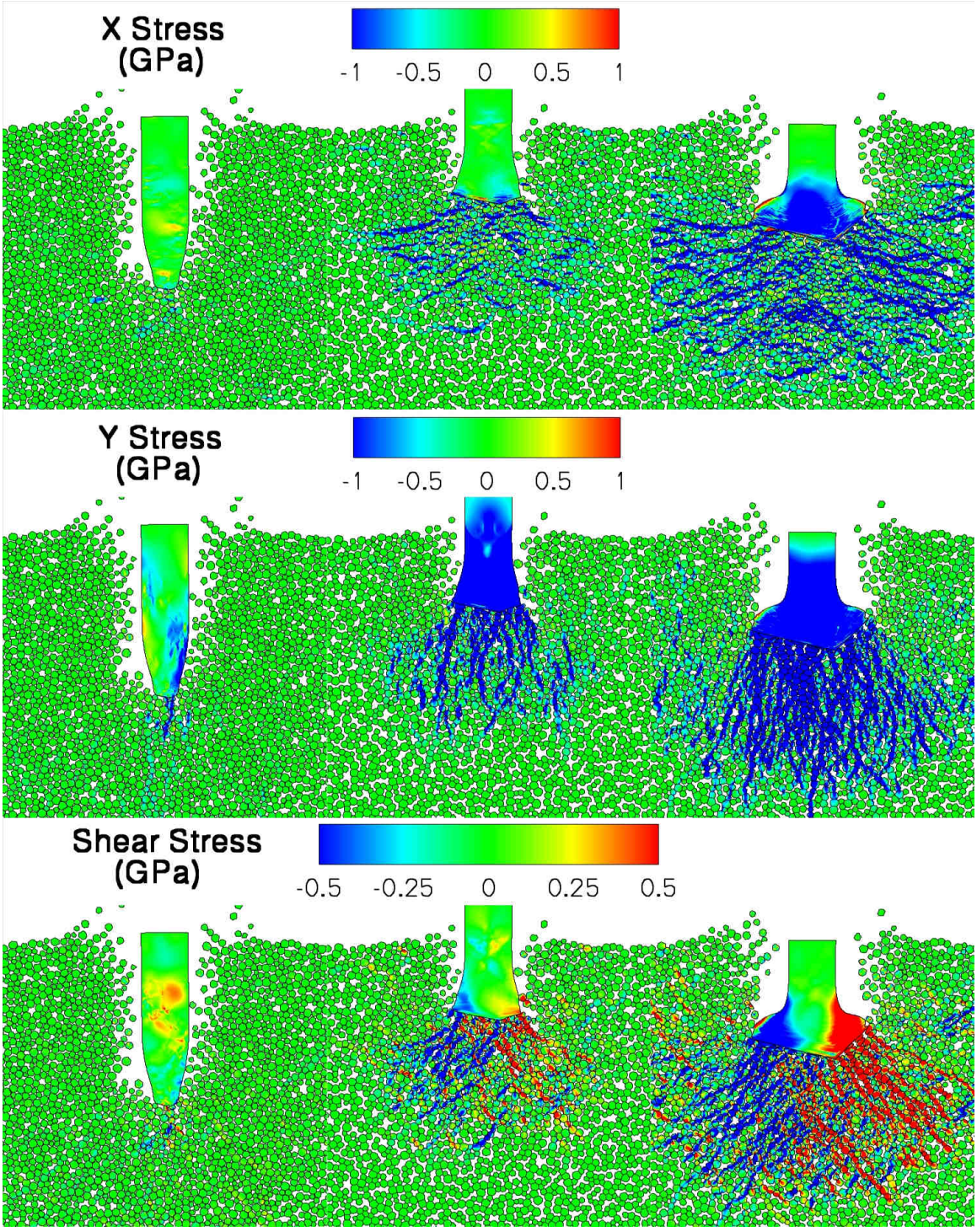

Figure 5.2: Plastic penetrator entering inelastic grains at, left 500 m/s, center 1000 m/s, right 1500 m/s. Showing contours of X Stress, Y Stress, and shear stress.

5.1.1 Inelastic Deformation of the Projectile

A notable feature in Figure 5.1 and 5.2 is the increasing inelastic deformation of the projectile with increasing velocity. The type of deformation shown here has been seen by Forrestal et al. [58] who conducted reverse ballistic shots using a gas gun. In Forrestal's work, foundry core impactors were fired at tungsten projectiles and showed increasing deformation with impact velocity. However, this large mushrooming effect is likely not physical in semi infinite target penetration as a number of other authors do not report such deformation [1, 7, 9, 11, 14].

The large projectile deformation could be caused by a number of factors. One reasonable explanation may be a flaw in the material models being used. As stated previously, the material model for a sand grain is not known. Another explanation may be the lack of projectile erosion and grain fracture. Neglecting erosion and failure may affect the penetration resistance of the media and lead to the greater than expected deformations. A third cause of the deformation may be an effect of the 2-D geometry. 2-D simulations may constrain the sand to displace under the projectile in only two directions. This may lead to a media that is more difficult to penetrate.

Whatever the cause of the deformation, it can be understood as a self-proliferating process. As the penetrator becomes deformed, its tip broadens and the amount of material which must be displaced increases. This further increases the penetration resistance and the inelastic deformation of the penetrator. To study the effects of target parameters without such large projectile deformations, each simulation used both inelastic and elastic projectiles.

The deformed projectile in the 1500 m/s case has taken on a wedge shape that is not centered at the projectile axis. This strange deformation is characteristic of a mesh effect. To check if this feature was a mesh based effect an alternate simulation was performed. In this alternate simulation, the projectile mesh was changed by using a different Cubit meshing algorithm. When the second simulation was completed, the deformation fields were similar and the wedge point on the deformed projectile occurred at the same location. Upon examining step by step simulation snap shots it was found that during the simulation, a region of empty space formed under one portion of the projectile and caused the formation of this deformed tip. This shows that this deformation is not merely a mesh effect but caused by the sand target.

5.1.2 Stress Fingers

Another qualitative feature shown in Figure 5.1 and Figure 5.2 is the presence of stress fingers. Stress fingers are commonly seen in granular materials [59, 60] and are caused by networks of individual grains which line up and transmit stresses along their length. Stress fingers may be an important indicator of instability as they are a direct evidence of the inhomogeneous loads placed on the projectile. When grains are not symmetrically placed around the impactor, differences will be manifested in the size of the stress finger networks. Large stress chain networks allow for the efficient transmission of stresses away from the projectile and will result in the application of increased loads on the sides of the projectile. This may cause deviation from the path and result in projectile bending.

Another feature of interest is the deformation zone around the penetrator. Unfortunately, the 1000 m/s simulation terminated early. Comparing the zones in the

500 and 1500 m/s cases is still informative. The affected zone in the 500 m/s case is larger than in the 1500 m/s case. This is reasonable as the grains have had three times as much time for displacment in the lower velocity simulations. This added displacement time may help to stabilize the projectile as the grains have had added time to become more homogonous.

5.1.3 Instability Measures

As previously discussed, a number of quantitative measures were used to gauge projectile instability. Figure 5.3 shows the lateral forces in kilonewtons incurred by the projectiles in the 500 and 1500 m/s simulations. From this figure it can be seen that the 500 m/s projectile experiences smaller lateral forces than the 1500 m/s projectile. Also, forces are applied evenly to both sides of the 500 m/s projectile while this is not the case in the 1500 m/s projectile. This is demonstrated by the average lateral force applied to the projectile throughout the simulation, presented in Table 5.1. The average lateral force applied to the 1500 m/s projectile is more than an order of magnitude larger than that applied to the 500m/s projectile.

The total projectile deviation from its path after one depth of penetration can also be used as a measure of instability. These values are displayed in Table 5.1. In this case, the deviation from the path for the two projectiles is relatively close. However, the deviation from the path in these simulations is obscured and may not implicate instability but rather the large asymmetric deformation of the 1500m/s projectile.

Another measure of instability, the projectile rotational momentum, is shown in Figure 5.4. Examining the projectile rotational momentum shows that, increasing projectile velocity results in increasing rotational momentum. The rotational momentum shown is

again obscured by the large inelastic deformation of the projectile. However, the trend of increasing instability with increasing velocity remains when considering elastic projectiles.

5.2 4-6 Baseline Simulations (inelastic grains, elastic impactor at three velocities)

As just discussed, elastic-plastic penetrators display an unrealistic amount of mushrooming. To investigate the stability of projectiles which retain their original shape, plastic deformation was removed artificially by increasing the yield strength of the projectile material. Figure 5.5 and Figure 5.6 shows various contour plots for simulations 4-6. These simulations again show the "finger" effect seen in the elastic/plastic simulations. In these simulations, the highest stresses are focused at the projectile tip and are more localized than in the case with the highly deformed penetrator. Comparing simulations 3 and 6 shows that the affected zone size around the projectile is similar in size, but the elastic projectile has penetrated into the highly stressed grains while the plastic penetrator has deformed laterally.

The deformation in the affected zones of the high velocity simulations can be qualitatively compared with experiments shown by Grantham et al. [61] who tracked the deformation fields produced during penetration using speckle correlation methods. Speckle correlation is a technique using X-ray detectable particles (lead) imbedded in a media which can be tracked using X-ray cameras and correlation software. This method allowed the authors to study the deformation fields around flat nosed projectiles during penetration experiments into sand at 1500 m/s. Grantham's experiments have features that are qualitatively similar to these simulations and show material flowing initially

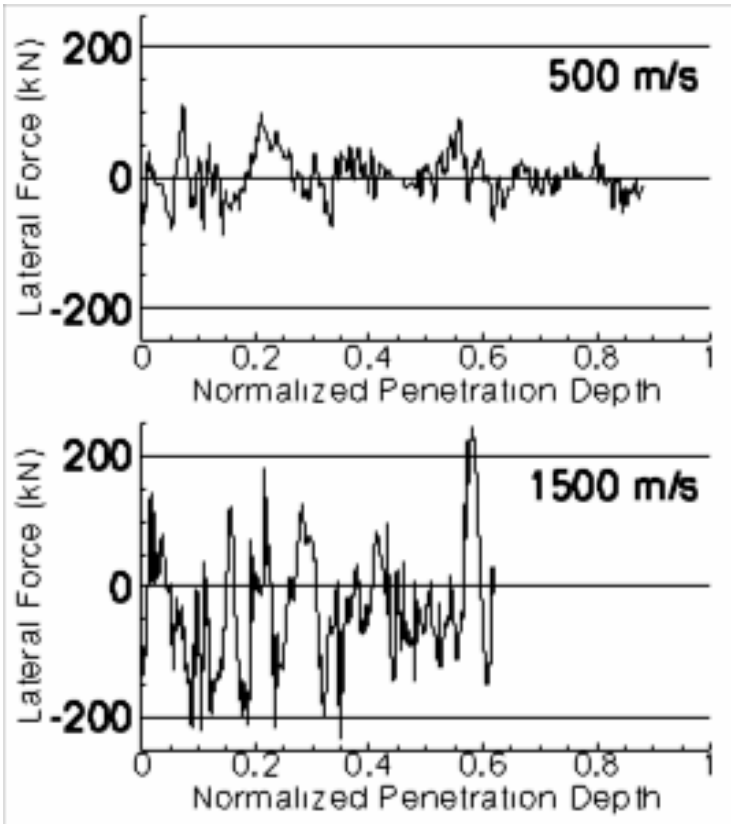

Figure 5.3 Lateral forces on the plastic penetrator from simulations 1 and 3 show large lateral forces at increased penetration velocity.

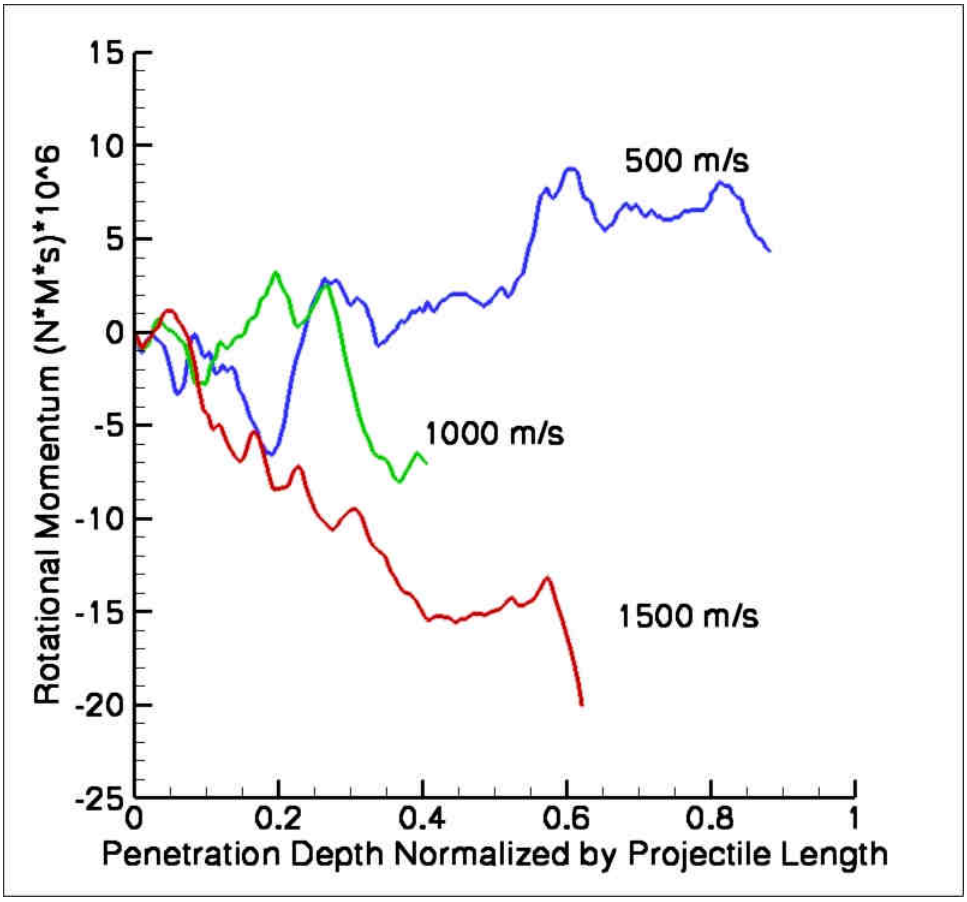

Figure 5.4 Rotational Momentum curves corresponding to the projectiles in simulations 1-3

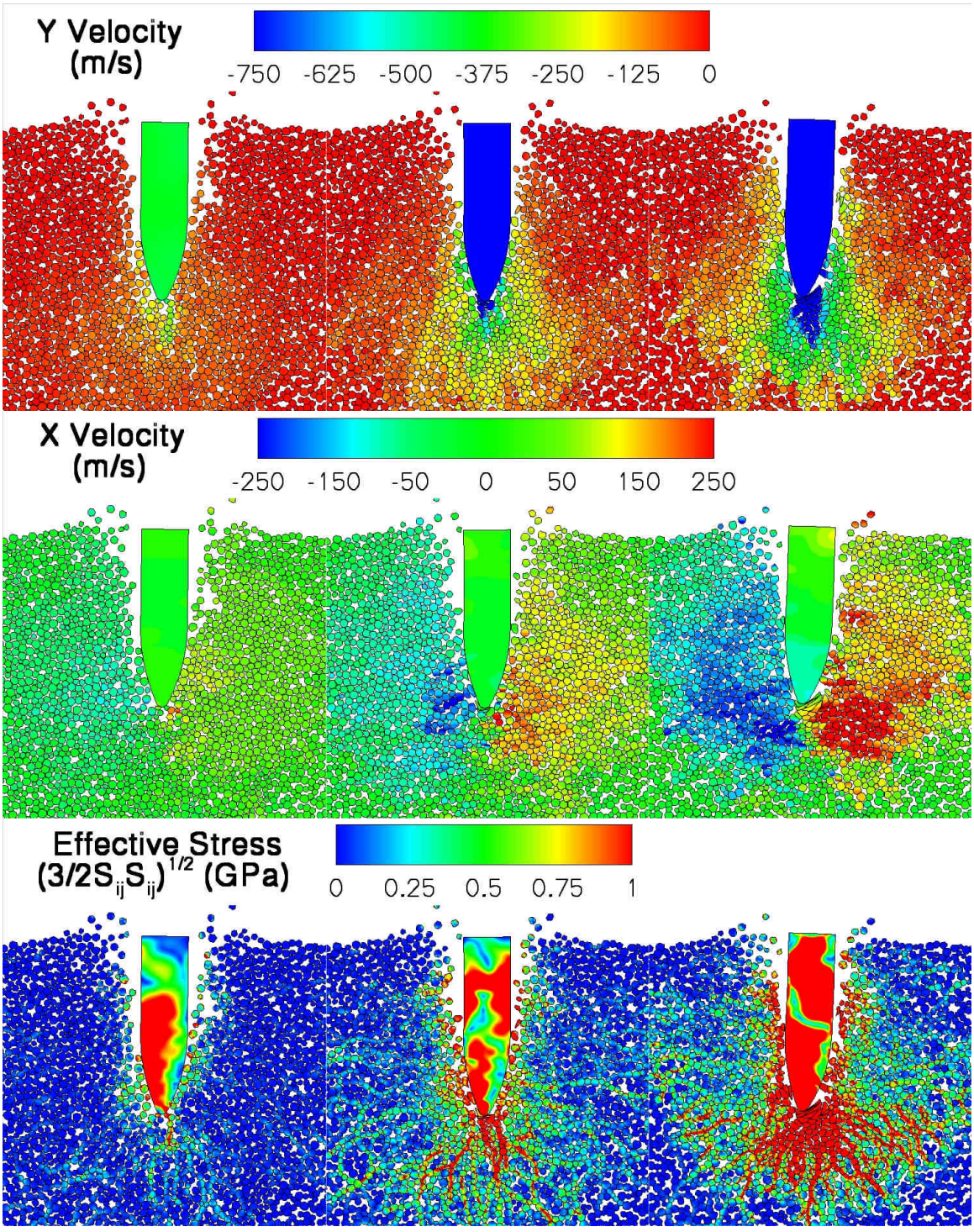

Figure 5.5 Elastic penetrator entering inelastic grains at, left 500 m/s, center 1000 m/s, right 1500 m/s. Showing contours of Y velocity, X velocity, and effective stress.

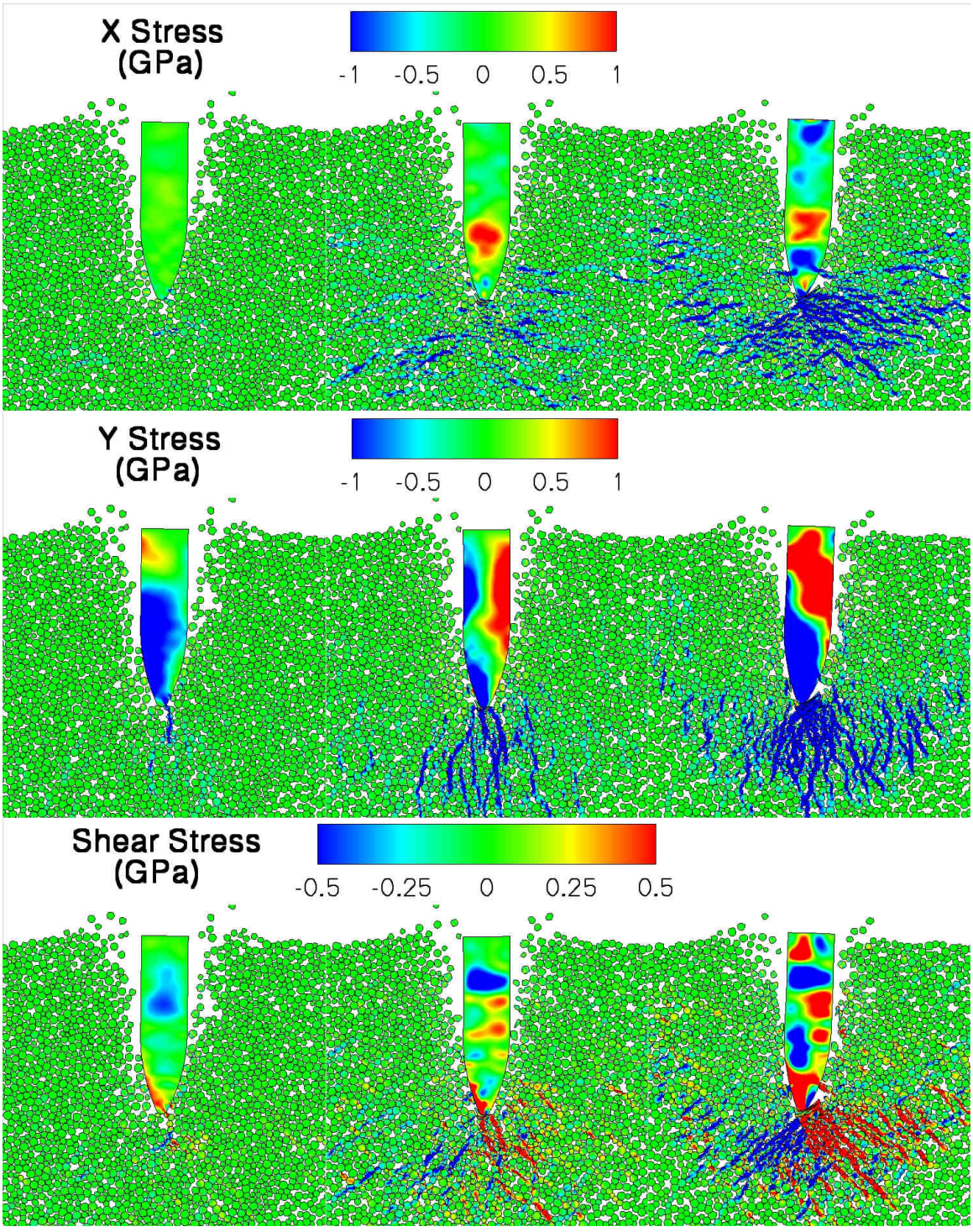

Figure 5.6: Elastic penetrator entering inelastic grains at, left 500 m/s, center 1000 m/s, right 1500 m/s. Showing contours of X Stress, Y Stress, and shear stress.

vertically with the projectile and then laterally outwards as the projectile continues to move into the media.

In these simulations, there is a region of highly stressed and compressed grains directly under the undeformed projectile tip. The location of this region is far away from the projectile center of mass. Because of this, the forces created by this region on the projectile have a large moment arm, and the ability to impart large changes in rotational moment to the projectile. This effect is seen in Figure 5.7 and can be compared with the rotational momentum of the plastic projectile fired into the same medium shown in Figure 5.4.

Lateral forces applied to the projectile through out the simulations were plotted for these simulations and can be seen in Figure 5.8. Similar to simulations 1-3, lateral forces increase with projectile velocity showing an increased tendency towards instability at high velocities. Also, with increasing velocity the forces become less centered about the zero axis. The average lateral forces on the projectile show that increasing penetration velocity causes the forces to become more focused on one side of the projectile than the other. This can be seen by comparing the average lateral forces in Table 5.1.

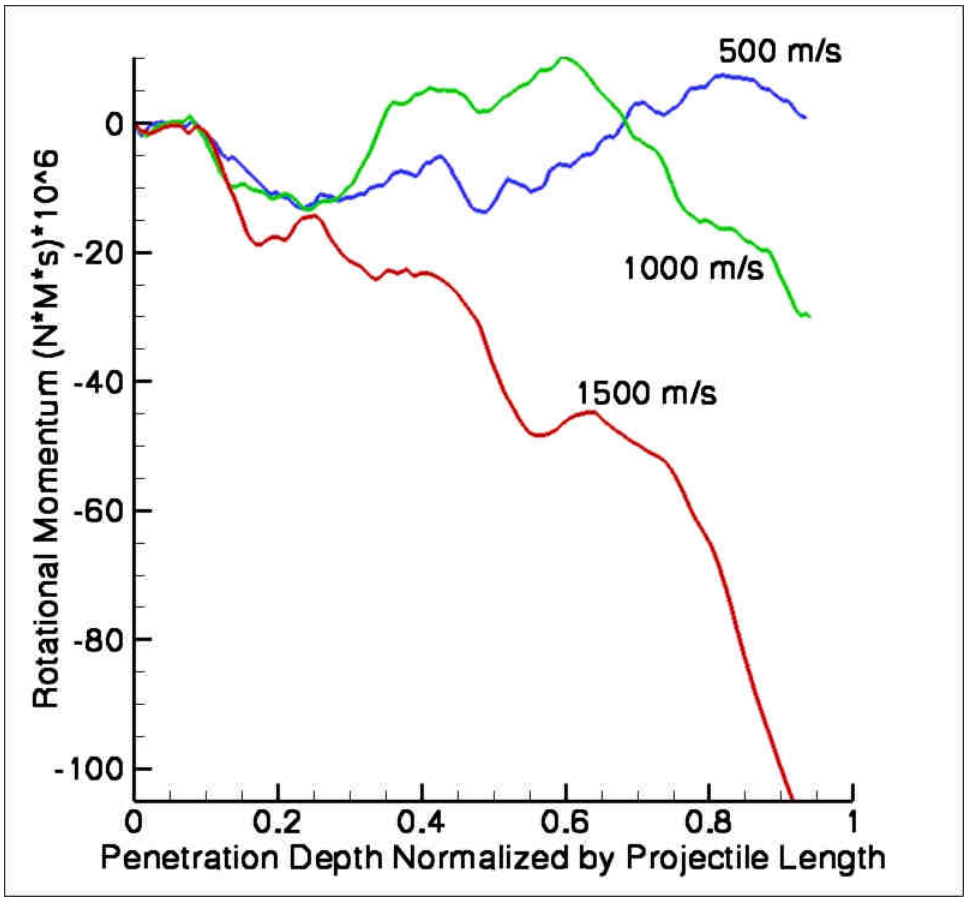

Figure 5.7 Rotational momentum curves corresponding to the projectiles in simulations 4-6 showing greater instability at higher velocities

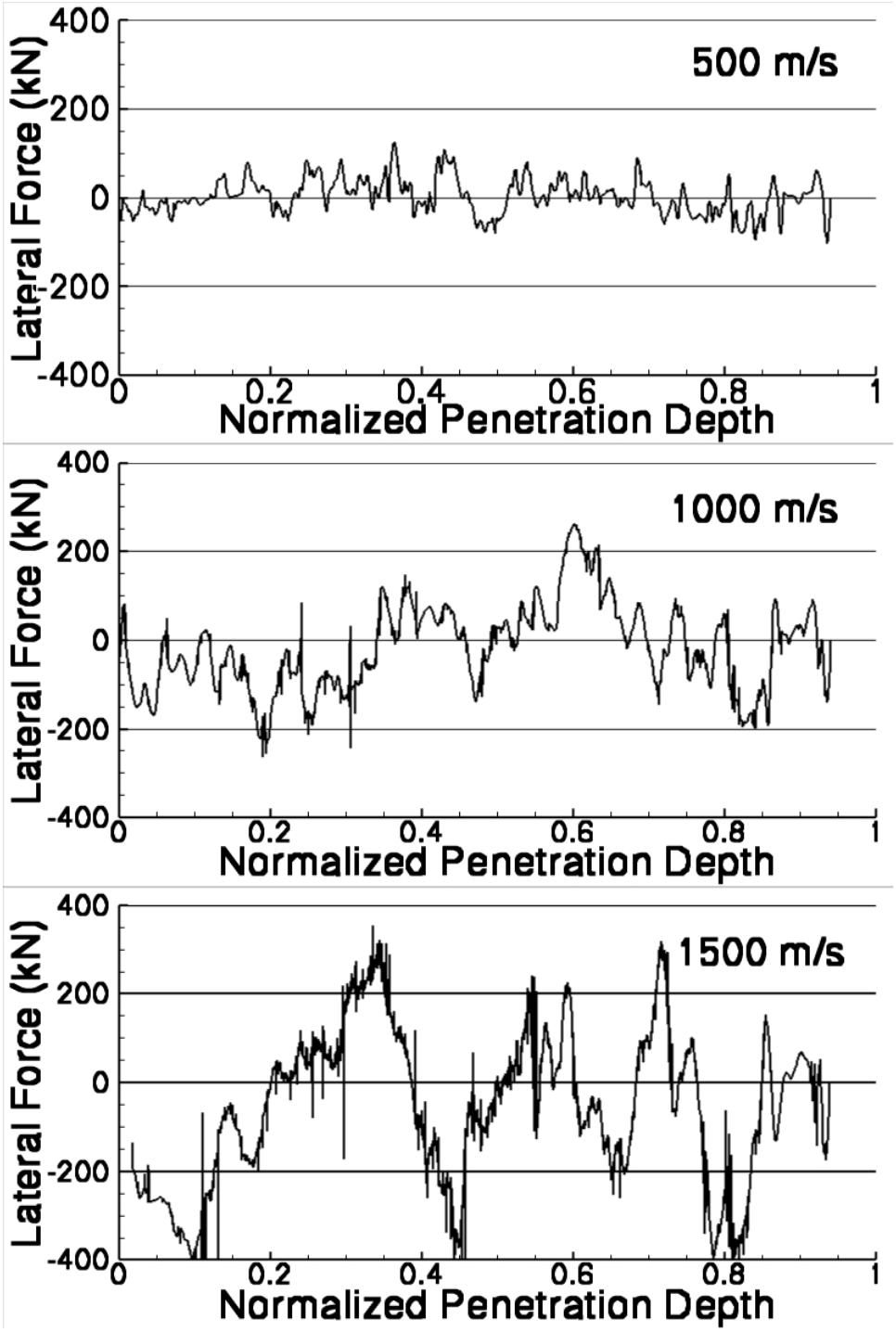

Figure 5.8: Lateral forces applied to elastic projectile in runs 4-6. Forces increase significantly with velocity

5.3 Effect of Sand Grain Strength:

To investigate the effects of grain strength on instability, two cases were considered in which the grains were defined as an elastic material (simulations 7 and 8 in Table 5.1). Plots at one depth of penetration showing velocity and effective stress contours are shown in Figure 5.9. Rotational momentum for these two cases is displayed in Figure 5.10.

In simulation 7 it can be seen that penetration resistance has increased and caused larger deformation if the projectile than in the case considering inelastic grains. In simulation 8, there is a focused region of stressed grains under the penetrator tip; however, to a lesser extent than in case 6 with elastic projectile and inelastic grains. This is notable because the penetrator shows less instability and may allude to one cause of instability: the formation of non-centered accumulation of compacted soil particles under the projectile tip. This type of formation would increase the amount of off-axis forces on the projectile and cause instability.

The rotational momentum plots show that the projectiles in these simulation are relatively stable as compared to the previous case with inelastic grains. In this case, the elastic-plastic projectile has received a relatively large amount of rotational momentum as compared to the elastic penetrator case. However, this can again be explained by the large asymmetric plastic deformation experienced by the projectile. The rotational momentum of the elastic projectile remains low when compared to the previous cases.

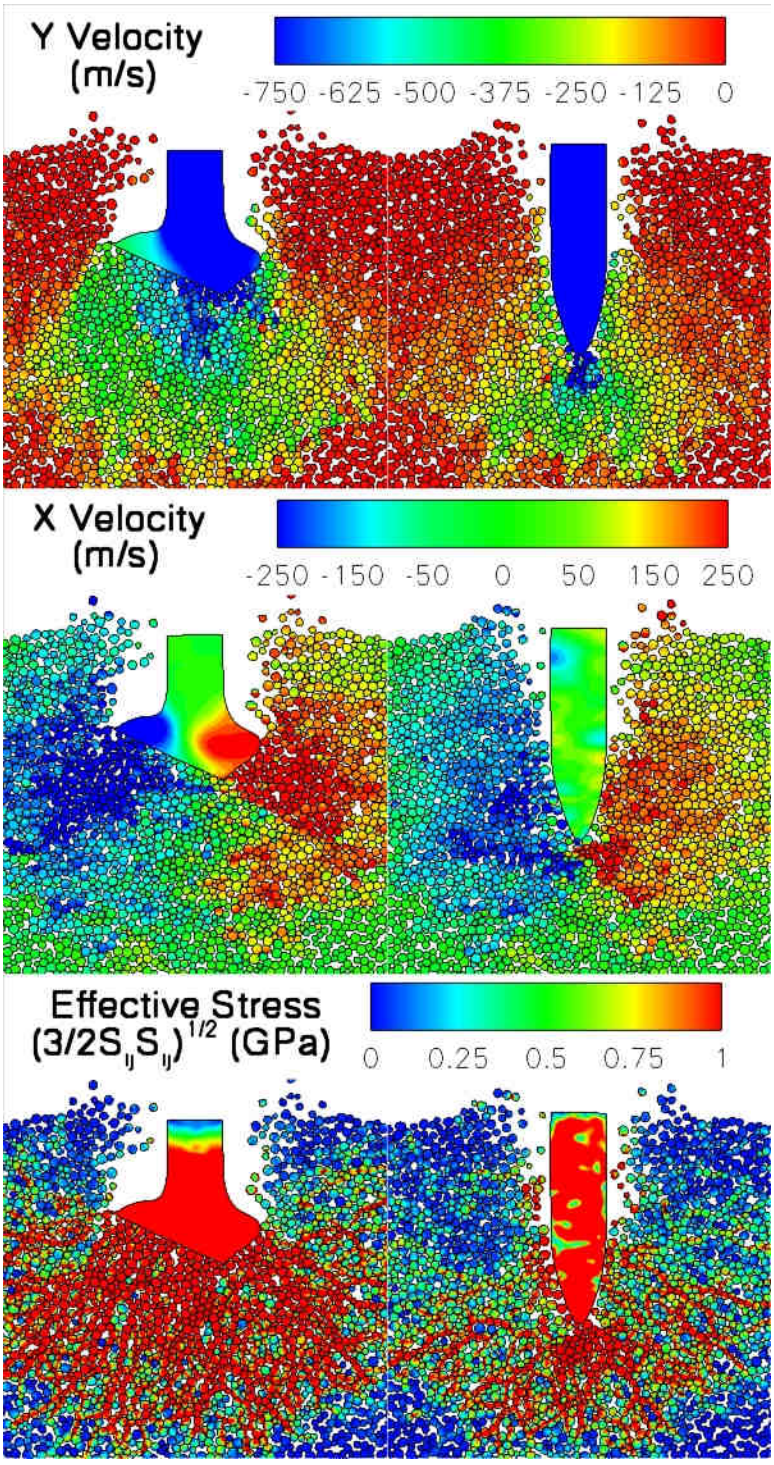

Figure 5.9: Plastic (left) and elastic (right) penetrators entering elastic grains at 1500 m/s. Showing contours of Y velocity, X velocity, and effective stress.

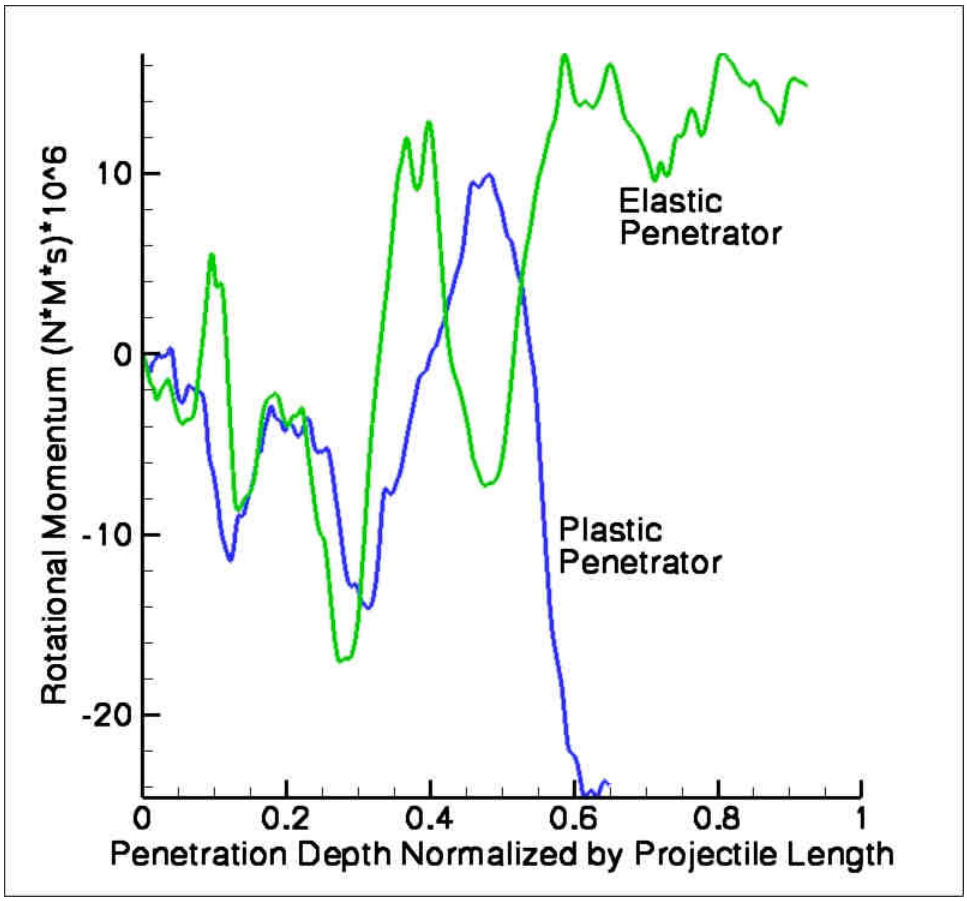

Figure 5.10: Rotational momentum for plastic and elastic penetrators entering elastic grains at 1500 m/s.

5.4 Effect of Grain Size and Grain Size Distribution:

Sand grains have different shapes and sizes. To probe the effects of grain size distribution, simulations 9 and 10 were performed with a uniform 60μm grain size. An interesting result occurred in simulation 10, as shown in Figure 5.11. It seems that the grains were not able to shift and move as easily as in the distributed grain size case. This effect is manifested in the large cluster that formed under the projectile tip.

It is clear that some numerical effects occur that influence the cluster size and shape. At this point, it is unlikely that grains would have failed (fracture). This said, the simulation can be compared with the case considering distributed grains. Although the same type of clustering occurs in both cases, the cluster size is much larger in this case. As seen in Figure 5.11, the large cluster happens to be off axis from the projectile and creates a large lateral force on the projectile as seen in Table 5.1. The rotational momentum of the projectile seen in Figure 5.12 also shows the effects of this large cluster as a large increase in projectile rotational momentum.

In these simulations, the effects of grain size was found to have a marked effect on instability. In simulations 11 and 12, projectiles were fired into grains ranging between 84 – 156 μm. As seen from the angle of projectile tilt in Figure 5.11, the larger grains produce an increased amount of instability. The instability caused by the large grains is comparable to the instability caused in the case of uniform grains, even though a large grouping of grains does not form.

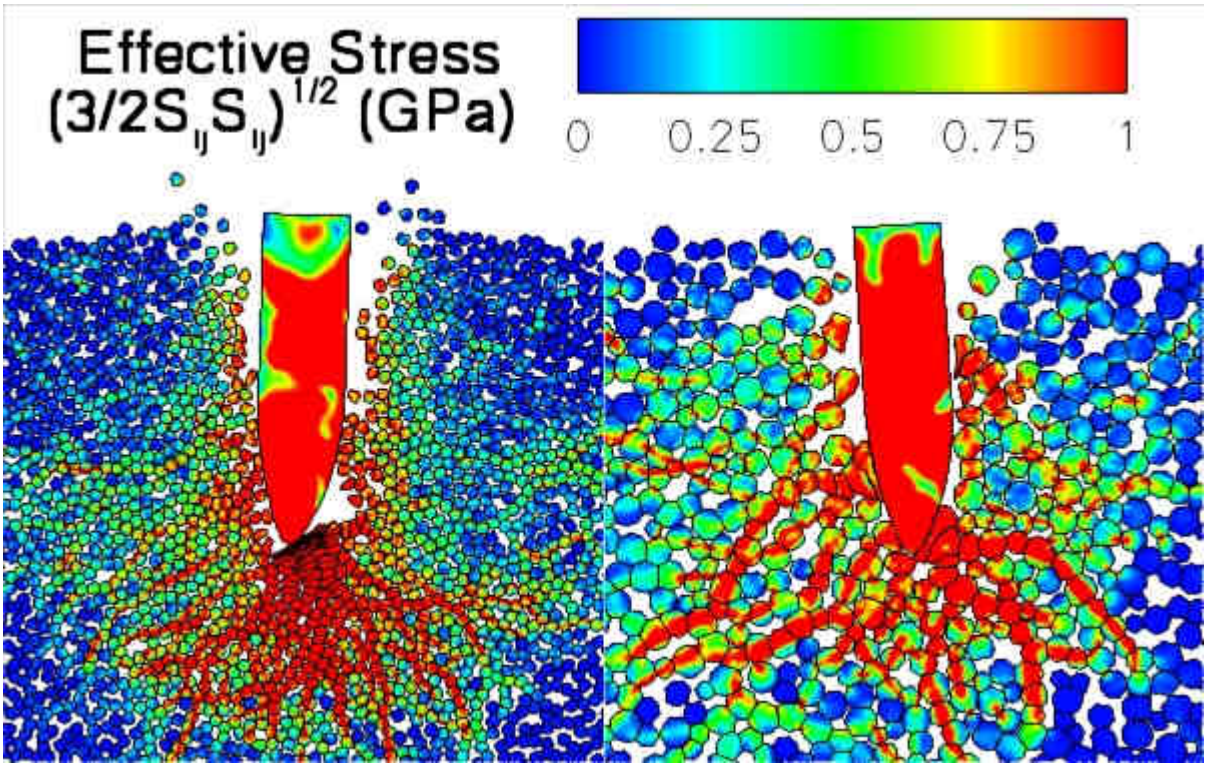

Figure 5.11: showing contours of effective stress Left: Elastic Penetrator into inelastic 60μm uniform grains (Run 10), Right: Elastic Penetrator into 84-156 μm grains (Run 12)

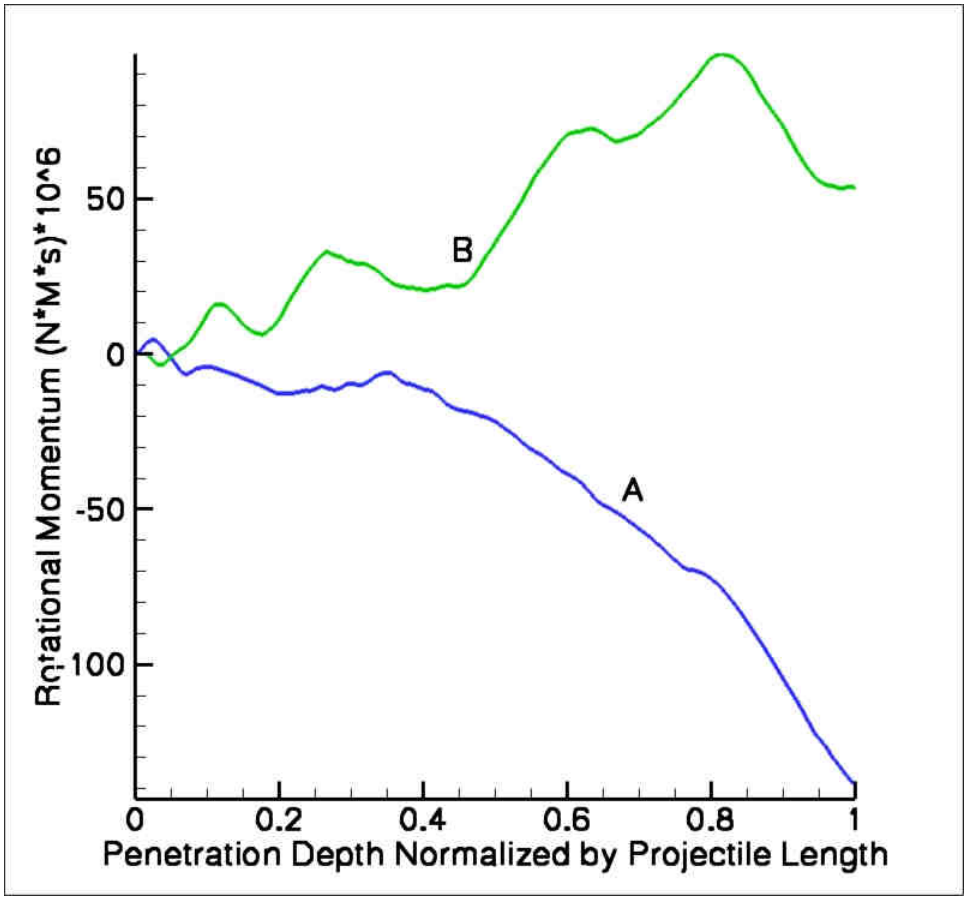

Figure 5.12: Rotational momentum curves for A: Elastic penetrator entering inelastic 60μm uniform grains (Run 10), B: Elastic penetrator entering inelastic 84-156 μm grains (Run 12)

5.5 Effect of Random Placement of Sand Grains:

To probe the effects of variations in grain placement, simulations 13 – 16 were completed. These simulations consider elastic projectiles with initial velocities of 1500 m/s. Targets have similar porosity and grain size distributions are those in simulation 6 but have a different granular arrangement. Three snapshots of these simulations are displayed in Figure 5.13 and can be compared with Figure 5.5. All the simulations have similar "finger" patterns and show variable amounts of rotational momentum displayed in Figure 5.14. As expected, these simulations demonstrate that different arrangements of sand particles affect the simulation results. However, instability seems to still occur regardless of the granular layout.

To further examine the effects of grain placement, targets were modified to produce grains with the same porosity and size distribution as before: but with larger clusters of sand grains and larger regions of empty space. These grains can be seen in Figure 4.17. The rotational momentum results for these simulations (17 & 18) displayed in Figure 5.15 show increased instability when compared to the cases with a more uniform distribution of grains and porosity.

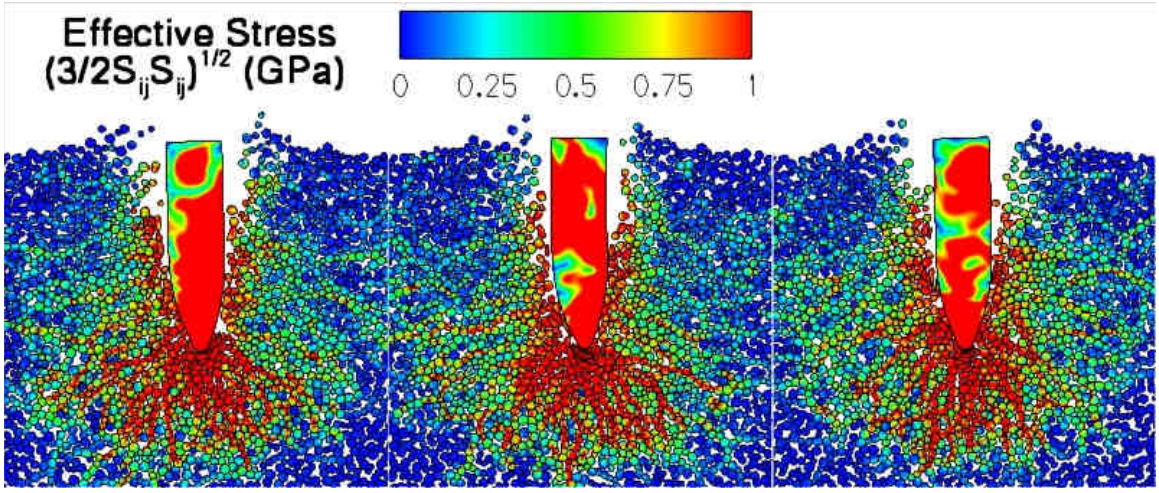

Figure 5.13: Elastic penetrators fired into 42-78μm targets with random seed variation, showing contours of effective stress. Runs 13, 15, and 16.

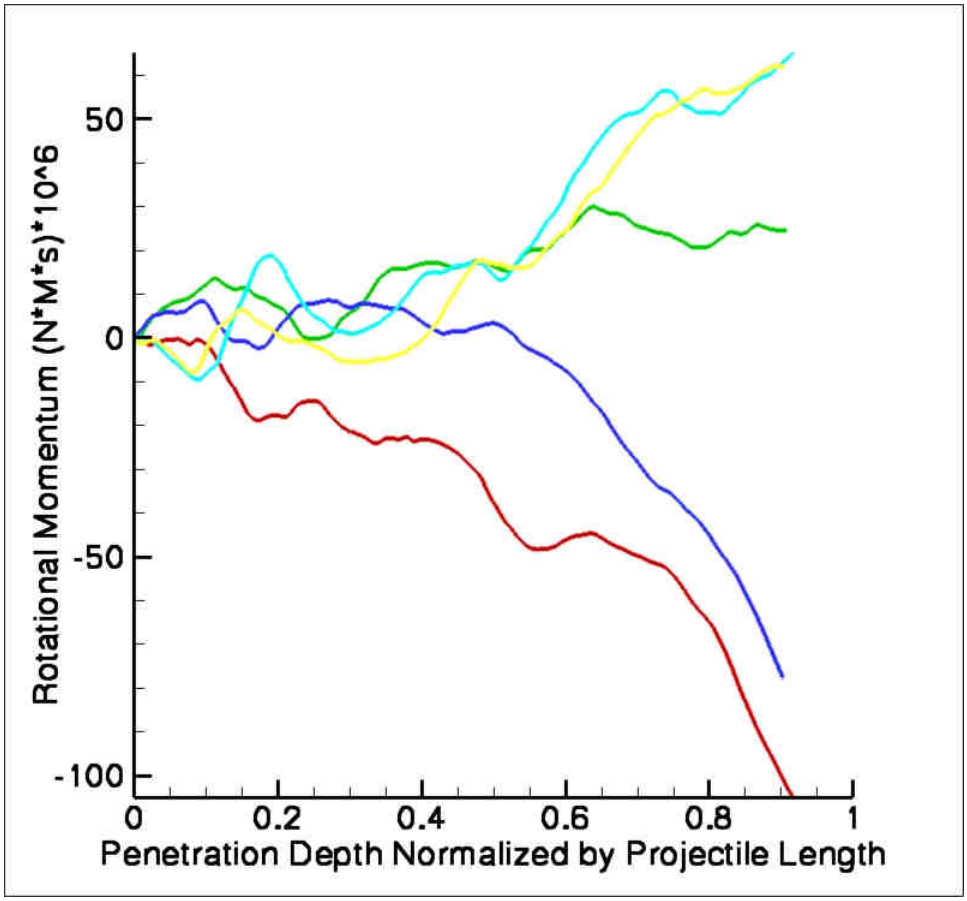

Figure 5.14: Rotational Momentum of 5 projectiles fired into targets with similar grain sizes and porosities.

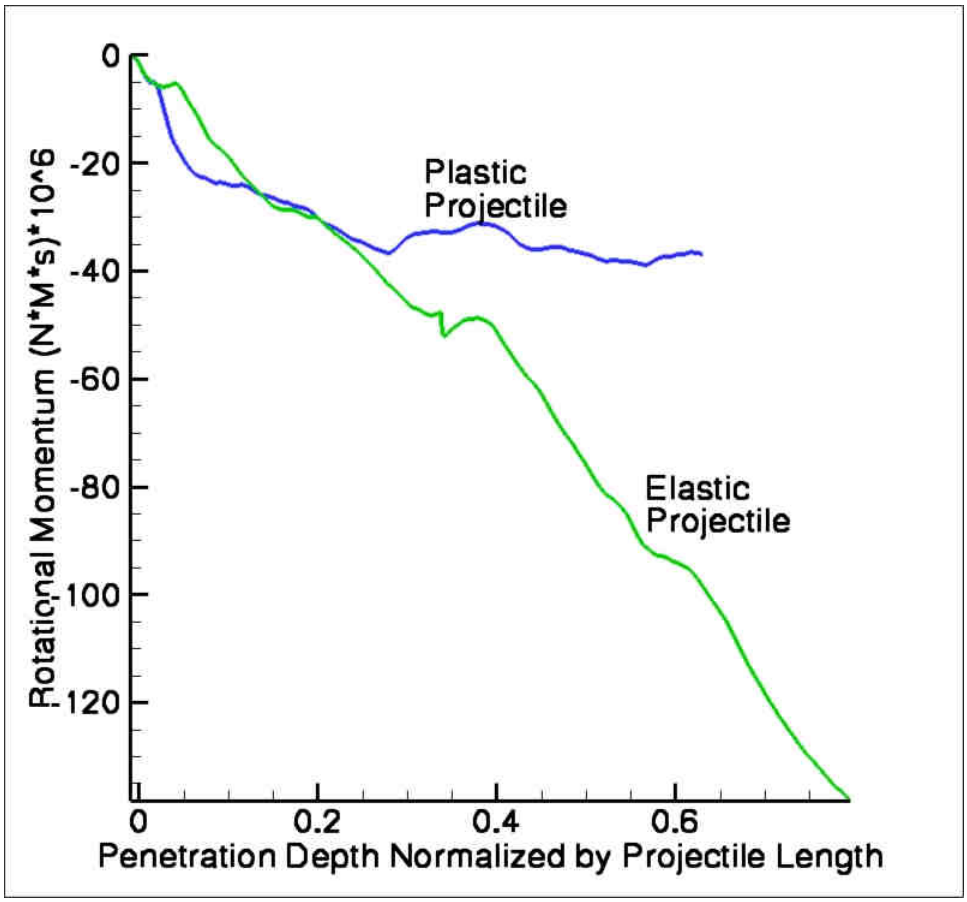

Figure 5.15: Rotational momentum of penetrators fired into clustered grains. Showing 1: Plastic Penetrator (Run 17) and, 2: Elastic Penetrator (Run 18)

5.6 Effect of Porosity:

The porosity of sand is variable. To examine the effects of target porosity two simulations were given with 20% and 40 % porosity. Upon testing the 20% porous targets deformation was so severe the simulations could not be completed. Simulations involving 40% porous targets can be seen in Figure 5.16 and are given as simulations 19 and 20. The plastic projectile shows less deformation than the 30% porous simulation shown in Figure 5.5. Also, stress and deformation fields surrounding the projectile are greatly reduced. Figure 5.17 shows the rotational momentum of the projectiles. It can be seen that the elastic projectile displays less instability than in simulation 6 considering targets with 30% porosity.

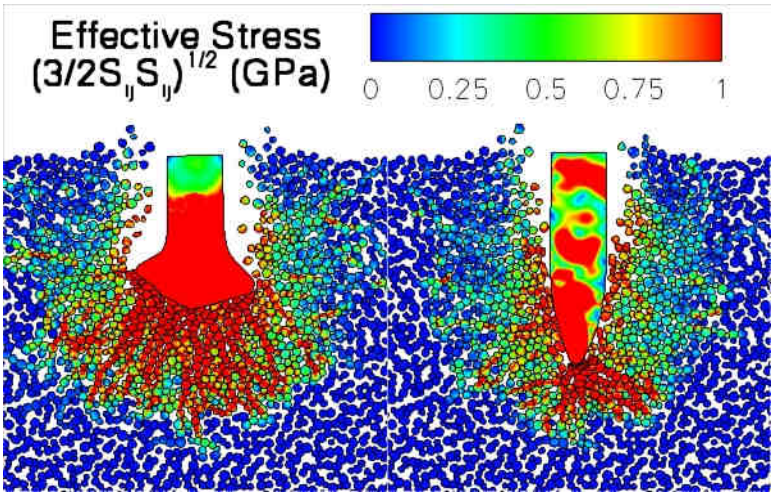

Figure 5.16: plots showing effective stress at one depth of penetration in 40% porous target Left: Plastic Projectile (Run 19), Right: Elastic Projectile (Run 20)

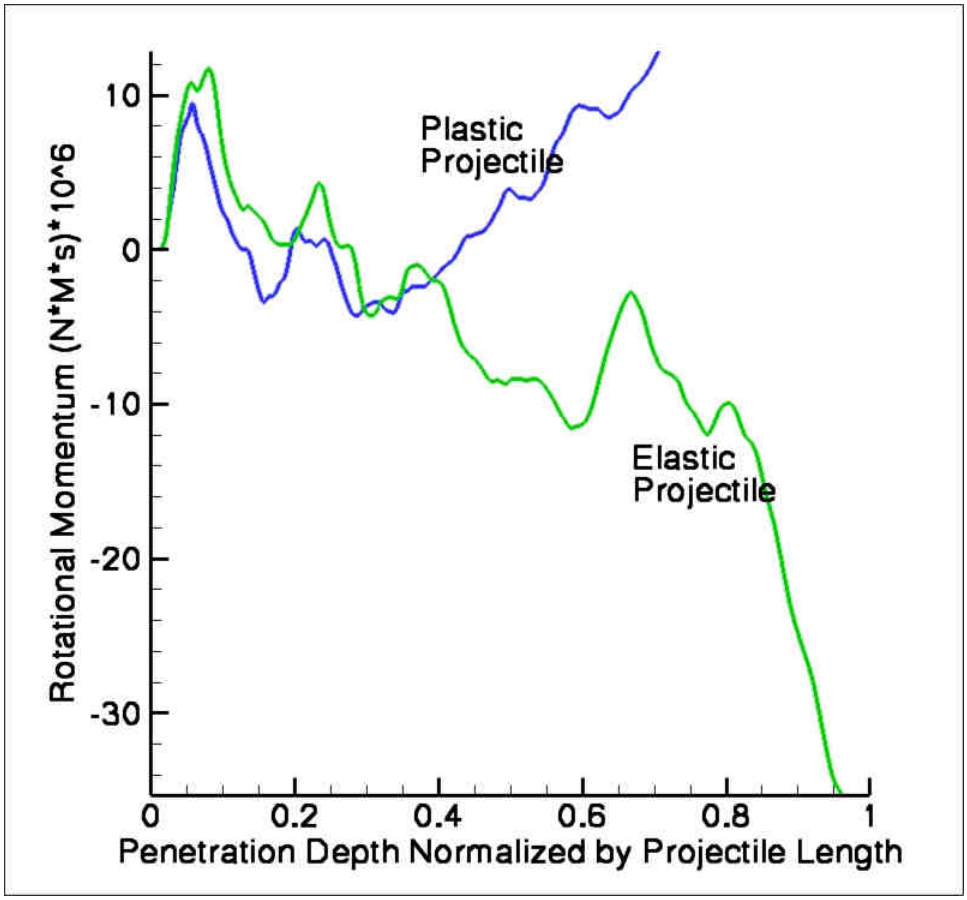

Figure 5.17: Rotational Momentum curves for plastic and elastic projectiles penetrating 40% porous targets.

5.7 Effects of Friction:

The frictional coefficient acting between grains during high speed sliding is not known. Friction [62-64] can be governed by a number of effects including surface roughness, contact velocity, localized heating, etc. For this reason, in all other cases a constant friction coefficient of .3 was used. To examine the effects of friction, simulations 21 and 22 were performed with frictionless grains and penetrator. The simulations shown in Figure 5.18 behave much like the higher porosity simulations. Deformation of the elastic-plastic projectile was reduced and the instability in the elastic projectile was reduced as demonstrated by the rotational momentum shown in Figure 5.19. One apparent feature is the relative lack of stress fingers. Compared with previous cases (Figure 5.13) these two runs show fewer long stressed chains of material demonstrating a more homogeneous target ahead of the projectile.

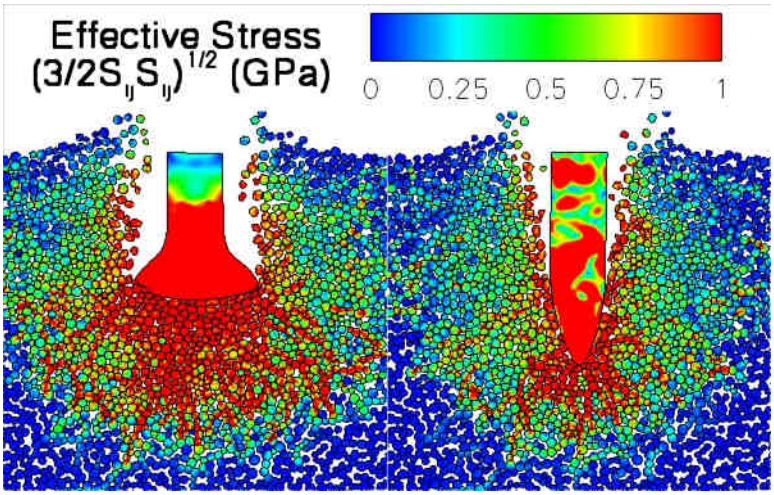

Figure 5.18: Plots showing effective stress at one depth of penetration in frictionless targets Left: plastic projectile (simulation 21), Right: elastic projectile (simulation 22)

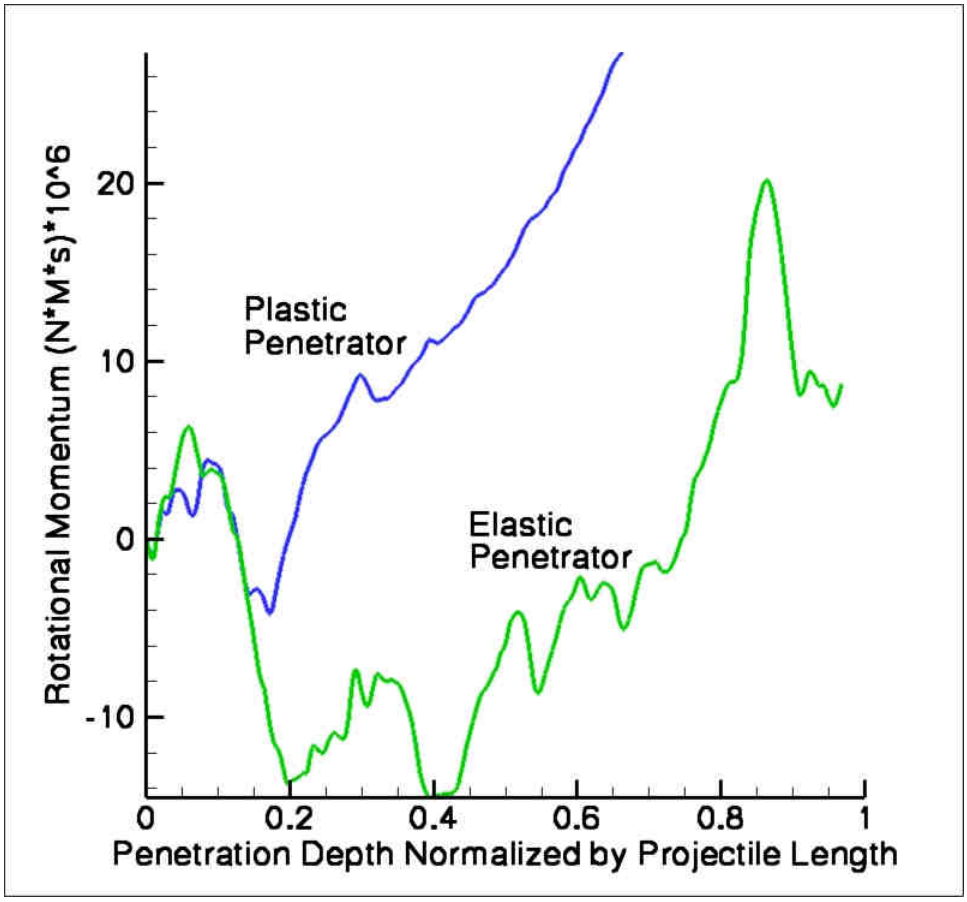

Figure 5.19: Rotational momentum plots of plastic and elastic projectiles penetrating frictionless targets

5.8 Deep Penetration Results

Up to this point only one depth of penetration has been considered. It has been shown that a single depth of penetration is enough to show the onset of instability. However, in pursuit of further evidence of instability, two simulations were performed that incorporated approximately 3 penetration depths. These simulations have over 20,000 grains and 800,000 finite elements. Because computation time becomes an issue with simulations of this magnitude, the two runs consider elastic penetrators and elastic grains. The target consisted of 42-78 um grains with a porosity of 30%. The only difference between the two runs was the coefficient of friction which was 0.0 and 0.3. These two runs can be seen in Figure 5.20. The effect of friction on instability is quite apparent as the frictional penetrator on the right has tilted to almost a 30 degree angle. Rotational momentum plots shown in Figure 5.21 show that in the frictional case the projectile gains rotational momentum at a rate grater than the projectile in the frictionless case. This leads to the projectile in the frictional case having a greater angle of tilt than in the frictionless case. Tilted projectile are direct evidence of projectile instability.

5.9 Examination of the Oscillations

An interesting feature can be found in many of the rotational momentum plots that consider elastic projectiles impacting at 1500 m/s. This feature is a periodicity in the rotational momentum seen in Figures 5.7, 5.10, 5.12, 5.14, 5.17, and 5.21. Periodicity can also be seen in the lateral force plots shown in Figure 5.8. In each plot, the periodicity was seen to occur at roughly the same frequency. Thus, the oscillations may correspond to the properties and geometry of the penetrator.

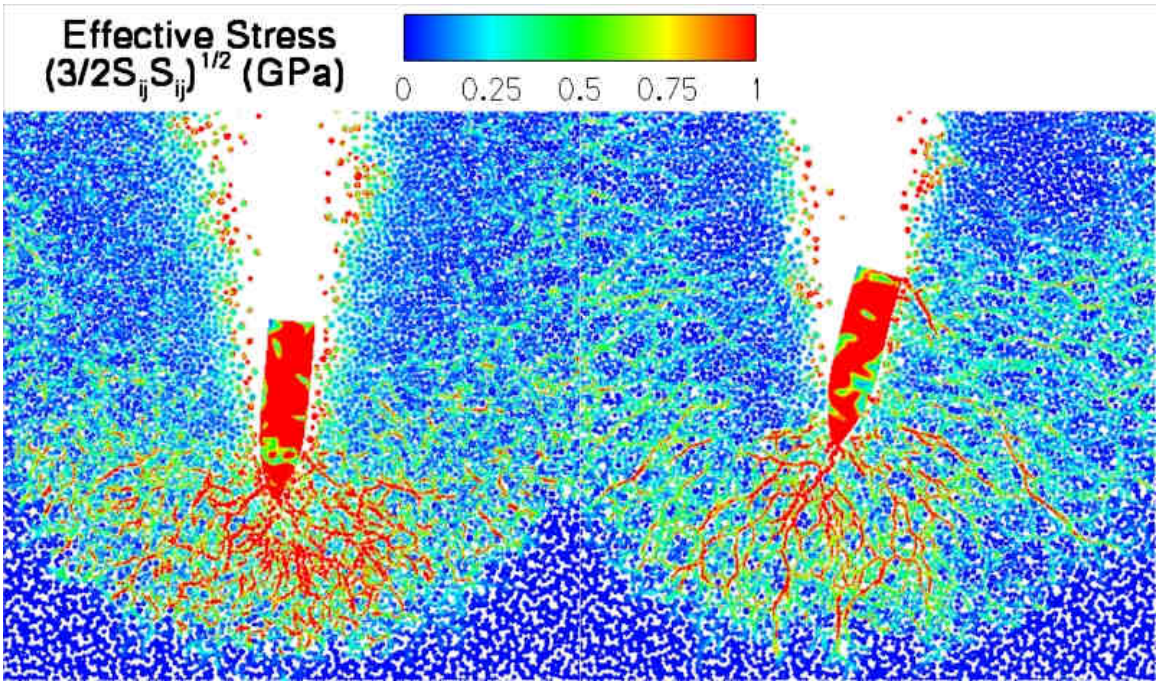

Figure 5.20: Deep penetration runs showing contours of effective stress, considering an elastic penetrator and elastic grains. A: frictionless penetration displays little instability B: frictional penetration shows instable behavior

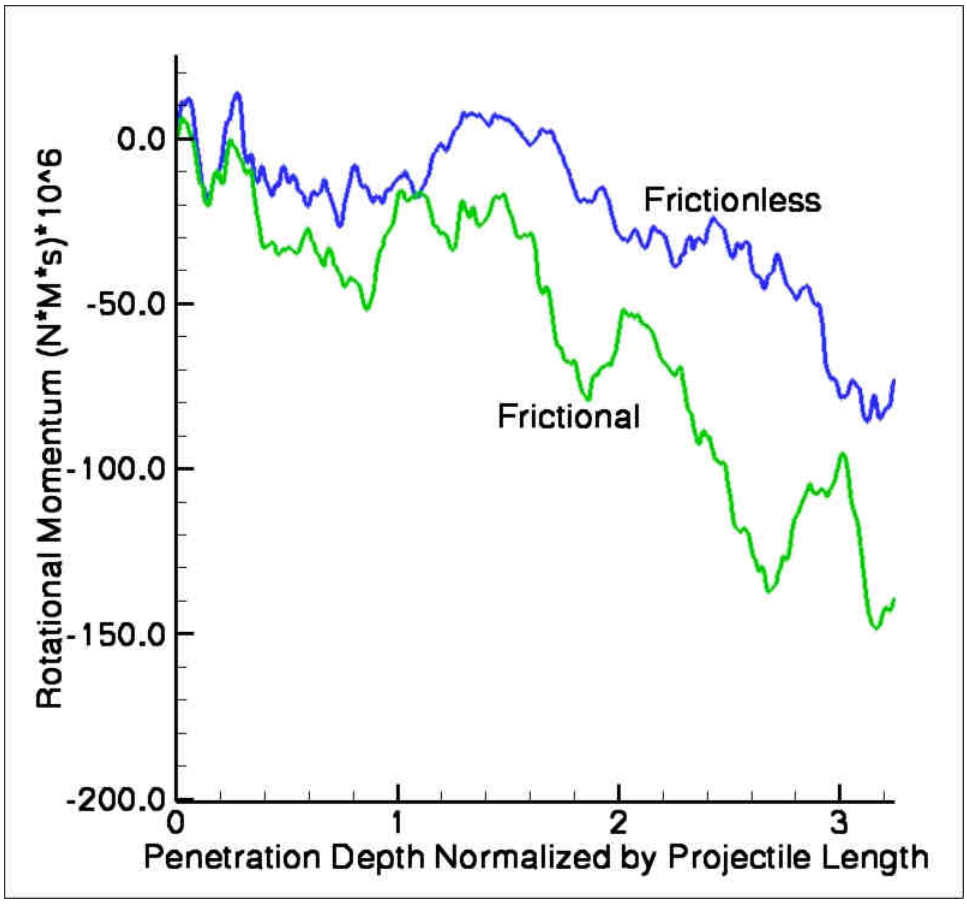

Figure 5.21: Rotational momentum curves of elastic penetrators impacting frictional and frictionless targets up to 3.5 penetration lengths.

5.9.1 Projectile Resonance

The physical phenomena that can cause such oscillations are not understood. However, it is useful to consider a projectile in contact with the sand grains, from the tip of the projectile to the end of the projectile. If this were the case, these oscillations could be explained simply. The projectile could begin to rotate and than be restored to its initial orientation by grains acting on the projectile shaft behind the center of mass. In this case, this idea is incorrect. Looking at the figures of the penetration event, it can be seen that the sand grains only contact the nose of the projectile. This being the case an alternate cause of projectile oscillation must be considered.

A possible solution to this question is that a resonant mode of the penetrator is becoming activated. To test the feasibility of this idea, resonant frequencies for the undamped free projectile were calculated by solving the Eigenvalue[16, 65] problem.

$$\left([K]-\omega^2[M]\right)[D]=0 \tag{5.1}$$

[K] and [M] are the finite element stiffness and lumped mass matrices, D is the displacement matrix for the nodes and ω is the modal frequency in Hz.

This calculation was completed using a program written in Matlab [66] which can calculate the Eigenvalues and Eigenvectors for a system with a large number of degrees of freedom. The code was validated by calculating the vibrational frequencies and mode shapes for a beam and comparing them with their analytic counterparts. This validation can be found in appendix B, the program itself can be found in appendix C.

The lowest three vibrational frequencies for the projectile were calculated and are shown in Table 5.2. Also shown in Table 5.2 are the depth of penetrations corresponding

to one complete resonant cycle of the modes (assuming a projectile velocity of 1500m/s). The first three resonant mode shapes are displayed in Figure 5.22 where the first two modes correspond to projectile bending and the third mode corresponds to projectile extension and compression. When these modes are compared to the oscillations shown in the rotational momentum plots, it can be seen that the first mode corresponds to the oscillations, while the 2nd and 3rd modes are not obviously visible.

Table 5.2: Projectile resonant modes

	Frequency MHz	**Depth of Penetration per cycle**
ω_1	**5.278**	**.17**
ω_2	**10.785**	**.084**
ω_3	**11.5**	**.078**
ω_1 **Mass x 2**	**3.732**	**.242**
ω_1 **Mass x 1/2**	**7.463**	**.121**

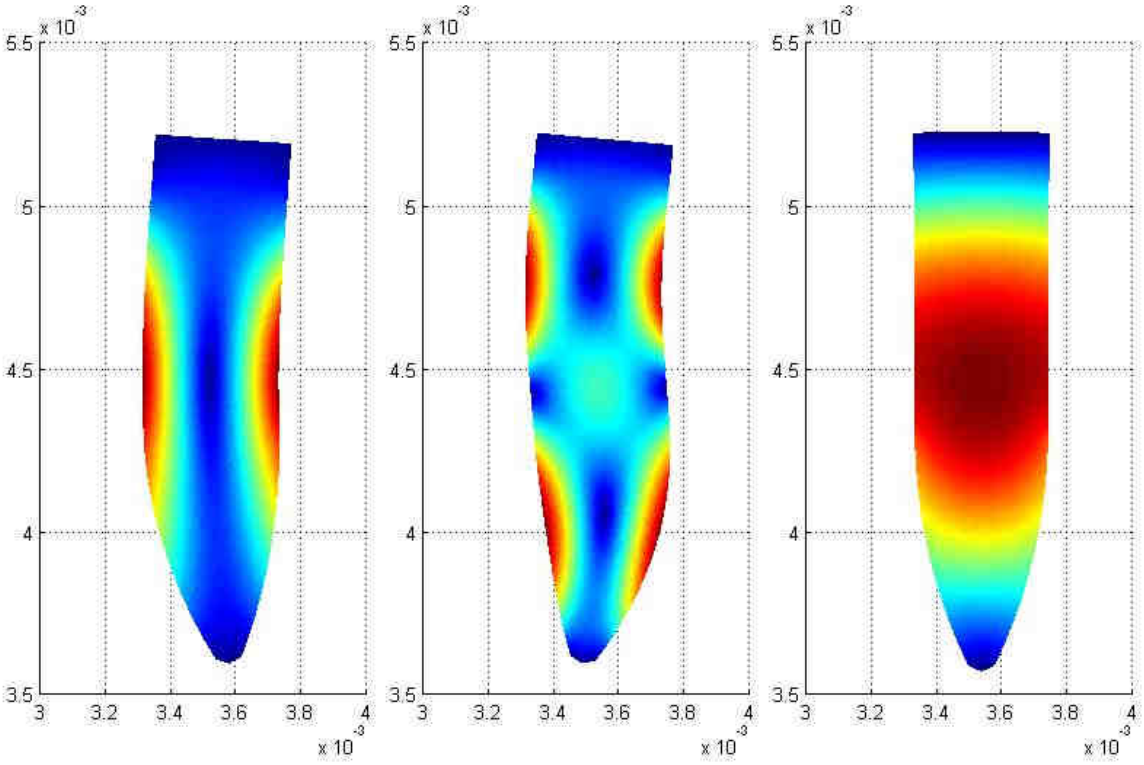

Figure 5.22: First three bending shapes arranged from lowest (left) to highest (right) showing contours of effective stress $\sqrt{\frac{3}{2}S_{ij}S_{ij}}$

To further probe these oscillations, simulations 25 and 26 were performed. These simulations have the same target and properties as those in simulation 6 with the variable of interest being the projectile density. Simulation 25 has a projectile with twice the density of steel and simulation 26 has a projectile with half the density of steel. This variable was examined as density affects the vibrational frequencies in beam bending theories.

In the Euler-Bernoulli beam theory, bending frequencies are given by.

$$\omega_i = c_i \sqrt{\frac{EI}{\rho A L^4}} \tag{5.2}$$

Where c_i is a constant, I is the projectile moment inertia, E is the projectiles modulus of elasticity, A is the projectiles cross sectional area, and L is the projectile length. Assuming that the projectile can be modeled with this equation, doubling the density of the projectile should decrease the modal frequencies by $1/\sqrt{2}$ and halving the projectile density should increase the modal frequencies by $\sqrt{2}$. Calculated lowest mode resonant frequencies from the Eigenvalue analysis compared well to the beam theory.

When the rotational momentum plot shown in Figure 5.23 is examined, a difference in the oscillation period can be seen. In the interest of comparing these oscillations with bending theory, a plot of radial momentum is shown in Figure 5.24 where the oscillations are more apparent. The trend of this difference is predicted by beam bending theory. The denser projectile showed oscillations with a larger period and the half dense projectile showed oscillations with shorter periods. Approximate periods were calculated from the points in Figure 5.24 and can be found in Table 5.3.

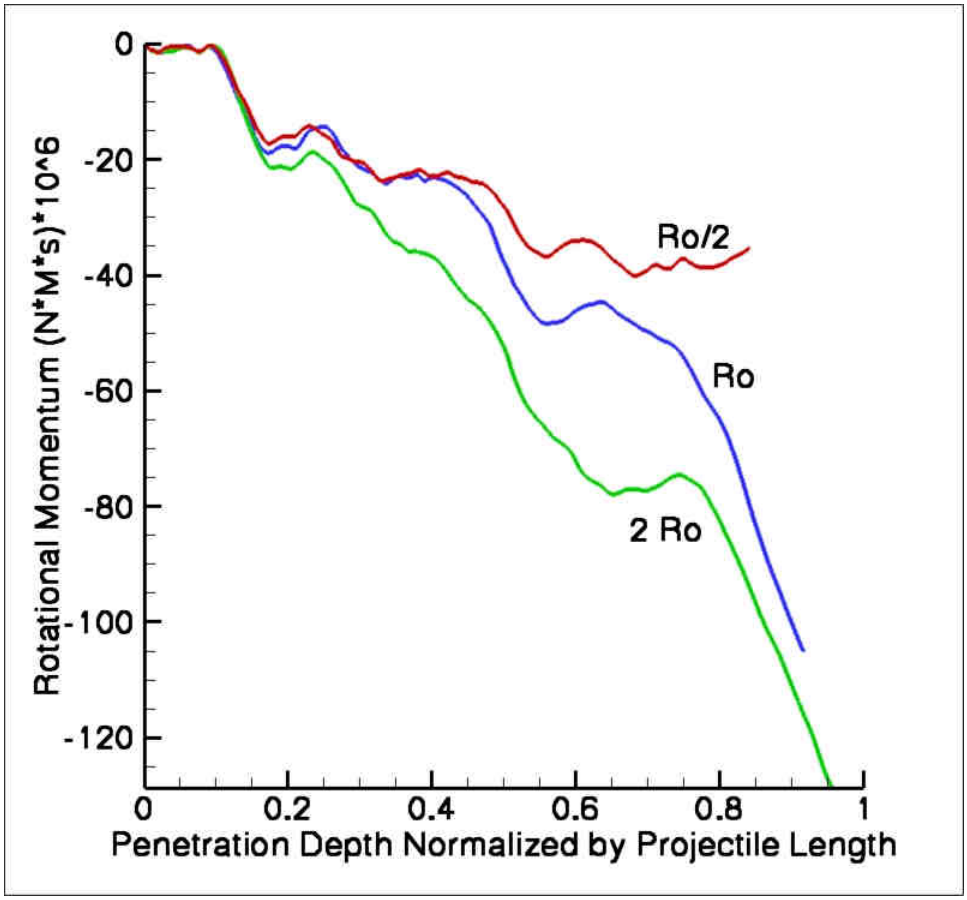

Figure 5.23: Calculated rotational momentum for projectiles with different densities

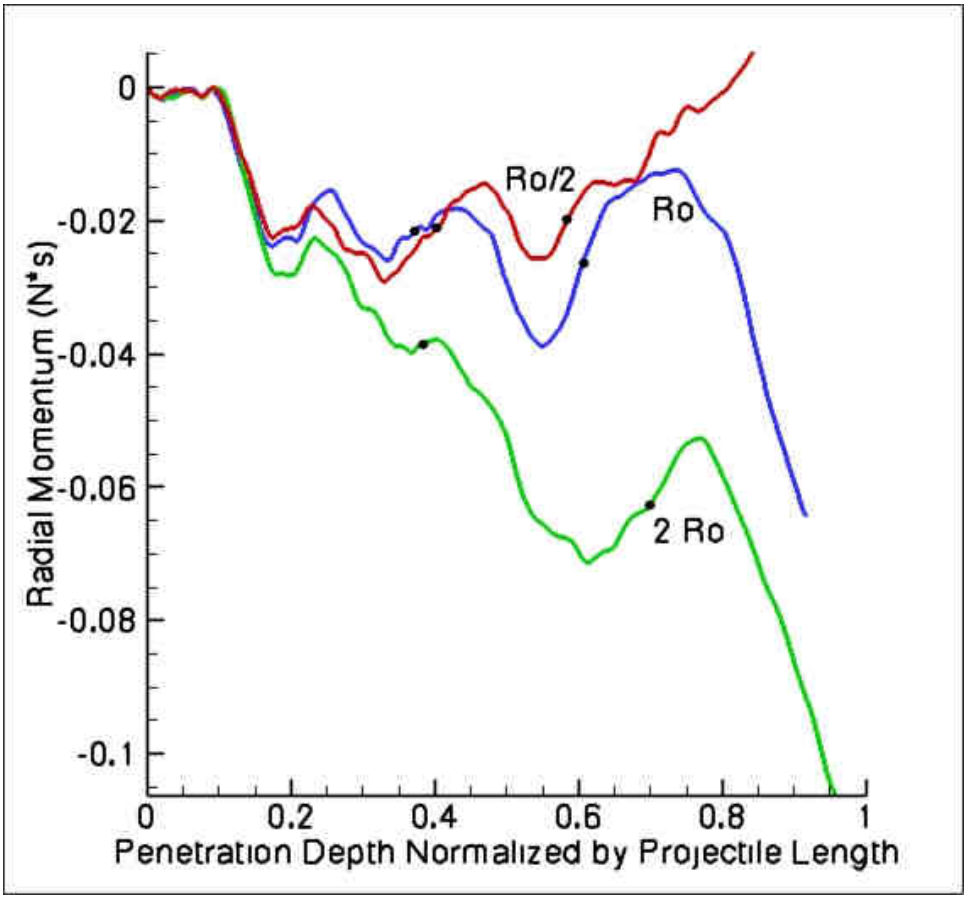

Figure 5.24: Calculated radial momentum for projectiles with different densities

Table 5.3: approximate oscillation periods for various density penetrators

Density kg / m^3	Scaled Depth of Penetration per Cycle
7823	.2347
15646	.3154
3911.5	.1790

It should be noted that the calculated modes correspond to a fully unconstrained projectile. In the mesoscale simulations the projectile will be constrained by its interactions with the sand grain; it is not known what effect this may have on the bending frequencies of the projectile.

These calculations cannot confirm the possibility of the projectile resonating during penetration. They also say nothing about resonance (if occurring) as a cause of instability. However, the correspondence of the period of oscillation found in the projectile rotational momentum plots with the first bending mode does support the idea of projectile resonance. If projectile resonance is occurring it supports the ideas of Jones et al.[10] and Graham et al.[17] who predict projectile instability using a simple buckling analysis.

SECTION 6
Summary and Conclusions

During high speed penetration of granular media, projectile motion becomes unstable due to divergence from initial path or projectile bending. To gain insight into the causes of projectile instability, a set of 2D mesoscale simulations was conducted accounting for the physical features in a sand target. In these simulations, the granularity of the media was incorporated by modeling each discrete particle as they moved and interacted during the simulations.

The mesoscale simulations were carried out using the 2D Lagrangian finite element code ISP-TROTP. The discrete sand targets were created using the code ISP-SAND, developed as part of this work. ISP-SAND can rapidly produce sand targets containing millions of sand grains with random morphologies.

Using the above capabilities penetration simulations were conducted and the effect of target parameters on projectile instability was examined. Projectile instability was quantified using projectile rotational momentum, average lateral forces applied to the projectile, and final projectile deviation from the expected path. It was demonstrated, through 2D simulations, that target granularity can produce projectile instability even for normal impact on the target.

Simulations predicted known phenomena such as stress fingers and highly compacted target regions under the projectile tip. Simulations considering elastic/plastic penetrators over-predicted projectile deformation. This may be due to deficiencies in material models, a lack of penetrator erosion and grain fragmentation, or 2D effects.

The heterogeneous response inherent in the mesoscale simulations, results in unbalanced forces on the impactor causing instability and deviation from the vertical path that increases with impact velocity. The simulations carried out in this work showed the following features of penetrator instability:

- Increases with projectile velocity
- Decreases with porosity
- Increases with grain size
- Increases with inter-granular friction coefficient
- Increases with uniform grain size distributions
- Is minimally affected by the random placement of sand grains with similar distributions
- Is affected by changing the distribution of grains and porosity

In many of the cases, the rotational momentum plots show oscillations with a similar length scale during penetration at 1500 m/s. These oscillations were found to correlate with the first unrestrained bending mode of the projectile, and they follow expected trends predicted by the Euler-Bernoulli beam theory (change depending upon projectile density). These two results suggest projectile resonance; however, further work is required to confirm this phenomenon and to determine its effects on instability.

BIBLIOGRAPHY

1. Allen, W.A., E.B. Mayfield, and H.L. Morrison, *Dynamics of a Projectile Penetrating Sand.* J. Appl. Phys., 1957. **28**(3): p. 6.

2. Robins, B., *New Principals of Gunnery*. 1742, London

3. Poncelet, J.V., *Cours de Mecanique Industrielle*. Vol. first edition. 1829.

4. Poncelet, J.V., *Introduction d la Mechanique Industrielle* 1839, Bruselles.

5. Davie, N.T., *A Method for Describing Nearly Normal Penetration of an OGIVE Nosed Penetrator into Terrestrial Targets*. 1979, Sandia Laboratories: Albuquerque NM. p. 60.

6. Feliece, C.W., *Personal Communication*. 2006: Pullman.

7. Biele, A., *An investigation of the terradynamic stability of a scaled-model projectile*, in *Mechanical Engineering*. 1976, Mississippi State University: Starkville.

8. Boulet, R.B. and C.W. Young, *Deep Earth Penetration Technology (DEPT)*. 1999, US Air Force Research Laboratory: Albuquerque.

9. Byers, R.K., P. Yarrington, and A.J. Chabai, *Dynamic Penetration of Soil Media by Slender Projectiles.* Int. J. Engng. Sci., 1978. **16**: p. 11.

10. Jones, S.E., et al., *Dynamic Buckling and Instability in Soil and Sand Penetration.* PVP, 2004. **489**: p. 6.

11. Savvateev, A.F., et al., *High-Speed Penetration Into Sand.* Int. J. Imp. Engng., 2001. **26**: p. 8.

12. Gupta, Y.M., C.W. Feliece, and S.K. Dwivedi, *Personal Communication*. 2006.

13. Dwivedi, S.K., J.R. Asay, and Y.M. Gupta, *Two-dimensional mesoscale simulations of quasielastic reloading and unloading in shock compressed aluminum.* J. Appl. Phys., 2006. **100**: p. 15.

14. Frew, D.J., M.J. Forrestal, and S.J. Hanchak, *Penetration Experiments with Limestone Targets and Ogive-Nose Steel Projectiles* J. Appl. Mech., 2000. **67**: p. 5.

15. Bathe, K., *Finite Element Procedures*. 2 ed. 1995: Prentice Hall.

16. Cook, R.D., et al., *Concepts and Applications of Finite Element Analysis*. 4 ed. 2002: Wiley.

17. Graham, C.H., et al., *Further Results on the Analysis of Penetrator Stability in Sand and Soil Targets.* PVP, 2005: p. 6.

18. Abrahamson, G.R. and J.N. Goodier, *Dynamic Flexural Buckling of Rods Within an Axial Plastic Compression Wave.* J. Appl. Mech., 1966: p. 7.

19. Gladden, J.R., et al., *Dynamic Buckling and Fragmentation in Brittle Rods.* PRL 2005. **94**: p. 4.

20. Lindberg, H.E., *Impact Buckling of a Thin Bar*. J. Appl. Mech., 1965: p. 8.

21. Lindberg, H.E. and A.L. Florence, *Dynamic Pulse Buckling*. 1987: Martinus Nijhoff Publishers.

22. Simonov, I.V. and K.Y. Osipenko, *Stability, Paths, and Dynamic Bending of a Blunt Body of Revolution Penetration into an Elastoplastic Medium.* J. Appl. Mech. Tech. Phys., 2004. **45**(3): p. 11.

23. Bishop, J.E., T.E. Voth, and K.H. Brown, *Semi-Infinite Target Penetration by Ogive-Nose Penetrators: Alegra/SHISM Code Predications for Ideal and Non-Ideal Impacts.* PVP, 2005: p. 10.

24. Resnyansky, A.D. and N.K. Borune, *Shock-wave Compression of a Porous Material*. J. Appl. Phys., 2004. **94**(4): p. 10.

25. Resnyansky, A.D. and N.K. Bourne, *Shock Compression of Dry and Hydrated Sand*, in *Shock Compression of Condensed Matter*. 2003.

26. Tsembelis, K., et al., *The Behavior of Sand Under Shock Wave Loading: Experiments and Simulations*, in *14 Technical Meeting, DYMAT*. 2002: Sevilla, Spain.

27. Vorobiev, O.Y., et al., *Simulation of Penetration into Porous Geologic Media.* International Journal of Impact Engineering 2007. **34**: p. 10.

28. Herrmann, W., *Constitutive Equation for the Dynamic Compaction of Ductile Porous Materials.* J. Appl. Phys., 1969. **40**(6): p. 10.

29. Zukas, J., *Introduction to Hydrocodes*. 2004: Elsevier Science.

30. Neumann, J.V. and R.D. Richtmyer, *A Method for the Numerical Calculation of Hydrodynamic Shocks.* J. Appl. Phys, 1950. **21**: p. 6.

31. Wilkins, M.L., *Calculation of Elastic-Plastic Flow*, L.R.L. University of California, Editor. 1963.

32. Wilkins, M.L., *Use of Artificial Viscosity in Multidimensional Fluid Dynamic Calculations.* J. Comp. Phys., 1980. **36**: p. 22.

33. Wilkins, M.L. and M.W. Guinan, *Impact of Cylinders on a Rigid Boundary*. J. Appl. Phys, 1973. **44**(3): p. 6.

34. Crowell, G.A., *The Descriptive Geometry of Nose Cones.* 1996.

35. DiGiulian, T. *Calculating CRH*. 2004 [cited 2006 7-19-2006]; Available from: http://www.navweaps.com/index_tech/tech-094.htm.

36. Dwivedi, S.K., *Material Model for Sand Grains*. April 24, 2007, Institute for Shock Physics: Pullman.

37. Khan, A.S. and S. Huang, *Continuum Theory of Plasticity*. 1995, New York: Wiley-Interscience

38. Malvern, L.E., *Introduction to the Mechanics of a Continuous Medium* 1969, Englewood Cliffs, New Jersey: Prentice-Hall.

39. Dwivedi, S.K., J.L. Ding, and Y.M. Gupta, *Computational Study of Interface Effect on Impact Load Spreading in SiC Multi-Layered Targets.* Int. J. Comp. Meth, 2005. **2**(3): p. 32.

40. Gupta, Y.M., *Physics 592, Wave Propagation Seminar* 2006.

41. Johnson, J.N., *Single-Particle Model of a Solid: The Mie-Gruneisen Equation* Am. J. Phys 1968. **36**: p. 3.

42. Seaman, L. and D.R. Curran, *TROTT Computer Program for Two-Dimensional Stress Wave Propagation*. 1978, SRI International: Menlo Park, CA.

43. Winey, J.M., R. Feng, and Y.M. Gupta, *Isotropic Material Models for the Elastic Response of Sapphire and Quartz Single Crystals Under Shock Wave Loading*. 2001, Institute for Shock Physics. p. 14.

44. Feng, R., G.F. Raiser, and Y.M. Gupta, *Shock Response of Polycrystalline Silicon Carbide Undergoing Inelastic Deformation.* J. Appl. Phys, 1996. **79**(3): p. 10.

45. Simha, C.H.M. and Y.M. Gupta, *Time-Dependent Inelastic Deformation of Shocked Soda-Lime Glass.* J. Appl. Phys, 2004. **96**(4): p. 10.

46. Frondel, C., *Dana's System of Mineralogy, Vol. III - Silica Materials* 1962, New York: John Wiley & Sons.

47. Swegle, J.W., *Irreversible Phase Transitions and Wave Propagation in Silicate Geologic Materials.* J. Appl. Phys, 1990. **64**(4): p. 17.

48. Ward, R.W., in *14th Piezoelectric Devices Conference and Exhibition*. 1992.

49. Krinsley, D.H. and J.C. Doornkamp, *Atlas of Quartz Sand Surface Textures*. 1973: Cambridge University Press.

50. Mahaney, W.C., *Atlas of Sand Grain Surface Textures and Applications*. 2002, New York Oxford University Press.

51. Dwivedi, S.K., *Personal Communication*, R.D. Teeter, Editor. 2005: Pullman.

52. Teeter, R.D., *Voronoi Tessellation with Varying Grain Sizes and Voids*. 2004, ISP: Pullman.

53. Teeter, R.D. and K. Perkins, *ISP-VORN*. 2005: Pullman.

54. Okabe, A., *Spatial Tessellations: Concepts and Applications of Voronoi Diagrams*. 2000, Chichester; New York: Wiley.

55. Kreyszig, E., *Advanced Engineering Mathematics*. 8 ed. 1999: John Wiley & Sons.

56. ASTM, *Manual on Test Sieving Methods*. Guidelines for Establishing Sieve Analysis Procedures, ed. C. E-29. 1972, Philadelphia, Pa: ASTM.

57. Allen, W.A., E.B. Mayfield, and H.L. Morrison, *Dynamics of a Projectile Penetrating Sand. Part 2.* J. Appl. Phys, 1957. **28**(11): p. 5.

58. Forrestal, M.J., L.M. Lee, and B.D. Jenrette, *Laboritory-Scale Penetration Experiments into Geological Targets to Impact Velocities of 2.1 km/s.* J. Appl. Mech., 1986. **53**: p. 4.

59. Bardenhagen, S.G. and J.U. Brackbill, *Dynamic Stress Bridging in Granular Material.* J. Appl. Phys, 1998. **83**(11): p. 9.

60. Geng, J., et al., *Memory in Two-Dimensional Heap Experiments.* Phys. Rev. E, 2001. **64**: p. 4.

61. Grantham, S.G., W.G. Proud, and J.E. Field. *The Study of Internal Deformation Fields in Materials Using Digital Speckle Radiography*. in *25th International Congress on High-Speed Photography and Photonics*. 2003: SPIE.

62. Bowden, F.P. and E.H. Freitag, *The Friction of Solids at Very High Speeds I. Metal on Metal; II. Metal on Diamond.* Proceedings of the Royal Society of London. Series A, Mathamatical and Physical Sciences, 1958. **A**: p. 17.

63. Bowden, F.P. and P.A. Persson, *Deformation, Heating and Melting of Solids in High-Speed Friction.* Proceedings of the Royal Society of London. Series A, Mathamatical and Physical Sciences, 1961. **260**(A): p. 25.

64. Jones, S.E., et al., *A One-Dimensional Analysis of Rigid-Body Penetration With High-Speed Friction.* Proceeding of the Institution of Mechanical Engineers, 2003. **217**(C): p. 11.

65. Sehmi, N.S., *Large Order Structural Eigenanalysis Techniques Algorithms for Finitie Element Systems*. 1989: Ellis Horwood Limited.

66. MathWorks, *Matlab 7.1*. 2007.

67. Bottega, W.J., *Engineering Vibrations*. 1 ed. 2006: Taylor & Francis.

Appendix A: Finite Element Mesh Size Selection

To probe the effects of mesh size on the simulation results, two simulations were run keeping all things constant varying only the mesh size in the penetrator. The simulations were run using the materials properties given in Table 3.1 and Table 3.2. The constant simulation parameters included an inelastic penetrator entering inelastic 60um grains at 1000 m/s. Mesh sizes used in the penetrators were 10 and 5μm.

Upon analyzing the results of the simulations it was found that there was some difference in the final result. This is as expected. These simulations are considering chaotic grain interactions and because of this, small changes in grain morphology or mesh size can have a large effect on the final result. As this is expected, in this work an emphasis has been put on the trends seen in the results rather than phenomenon seen in each individual result.

Figure A.1 and A.2 show the results for the 10 and 5 μm mesh sizes at approximately .4 depths of penetration. This time was chosen as contact problems arose in the 5 μm mesh sized projectile after this time. It can be seen that the deformation fields have some differences and that the projectile with the fine mesh is showing strange deformations at the tip where single elements have become highly deformed and protrude from the penetrator. Figure A.3 shows rotational momentum plots from the two cases. It can be seen that the trends are reasonably similar up to the termination point for the 5 μm mesh simulations. However, trends may continually grow apart at further times.

Small perturbations added to the initial simulations can cause differences in the final simulation results. Also these perturbations can be added from various factors such

as grain morphology, mesh size, mesh structure, initial penetrator position, as well as others. To eliminate mesh size as a variable a single mesh size was used. Due to the unrealistic deformation features (mesh folding) found in the 5 μm mesh size penetrator a mesh size of 10 μm was used through out the simulations.

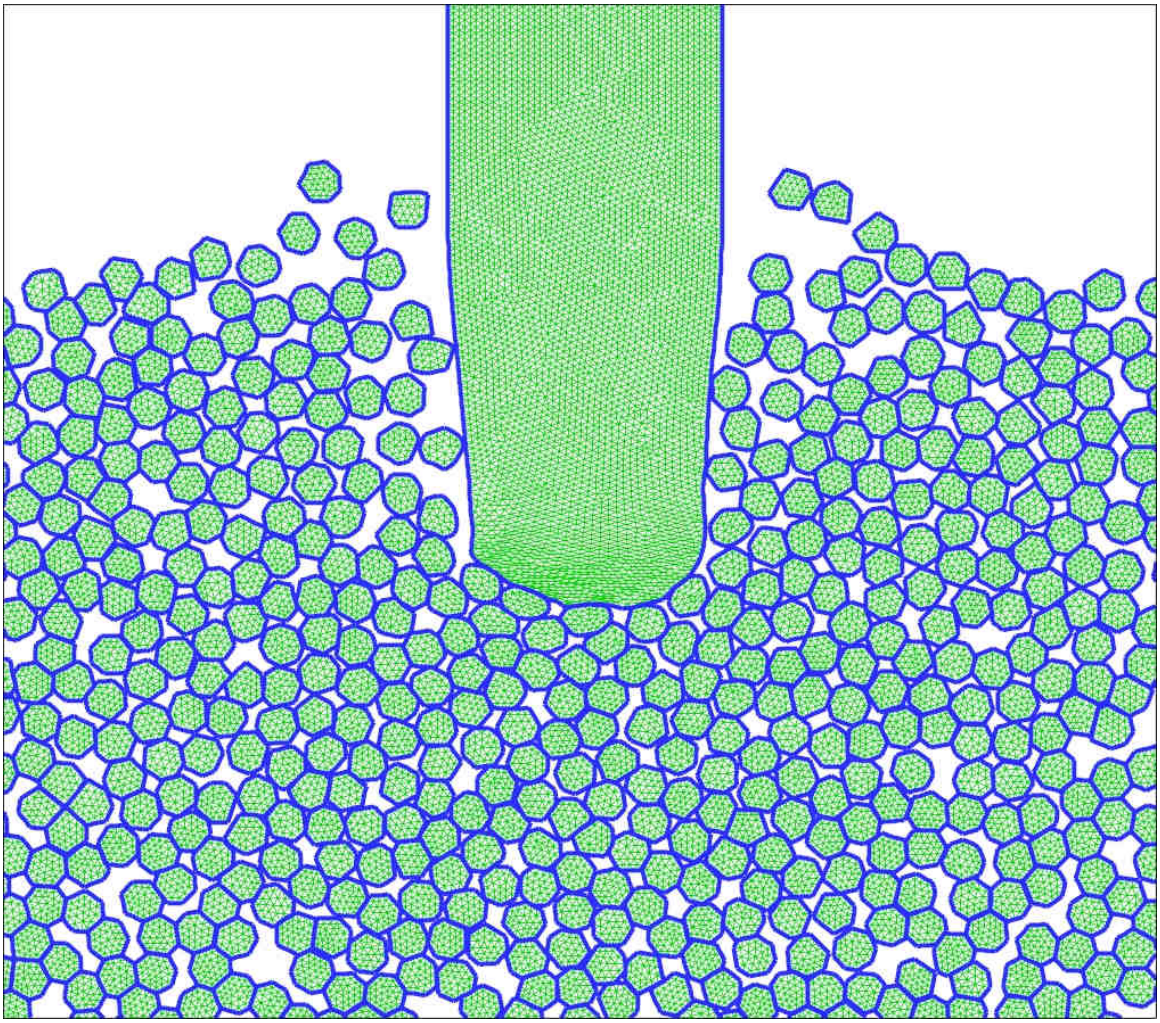

Figure A.1: Snapshot at .65 us showing the deformation field in the 10μm mesh size penetrator and grains.

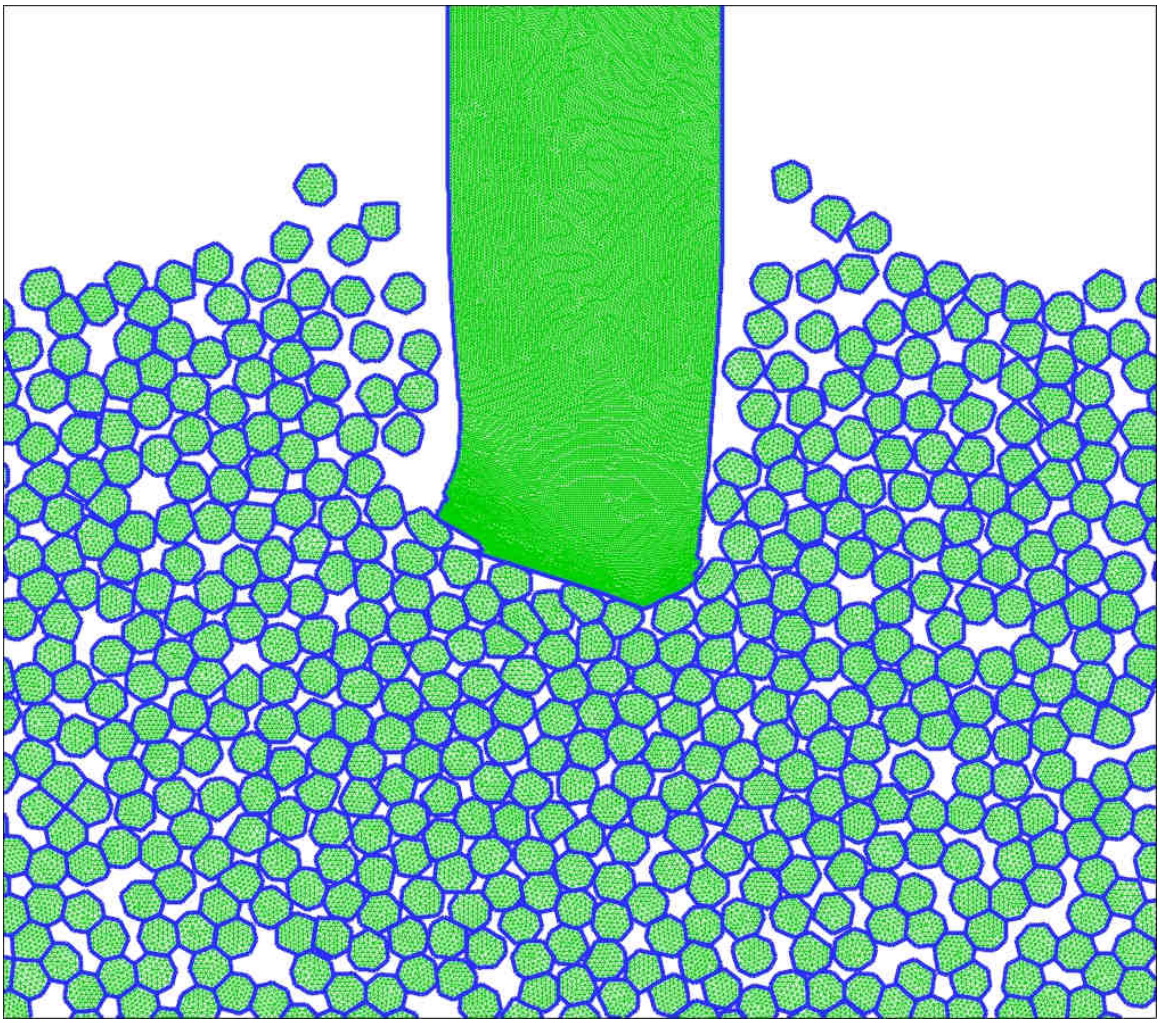

Figure A.2: Snapshot at .65 us showing the deformation field in the 5μm mesh size penetrator and grains.

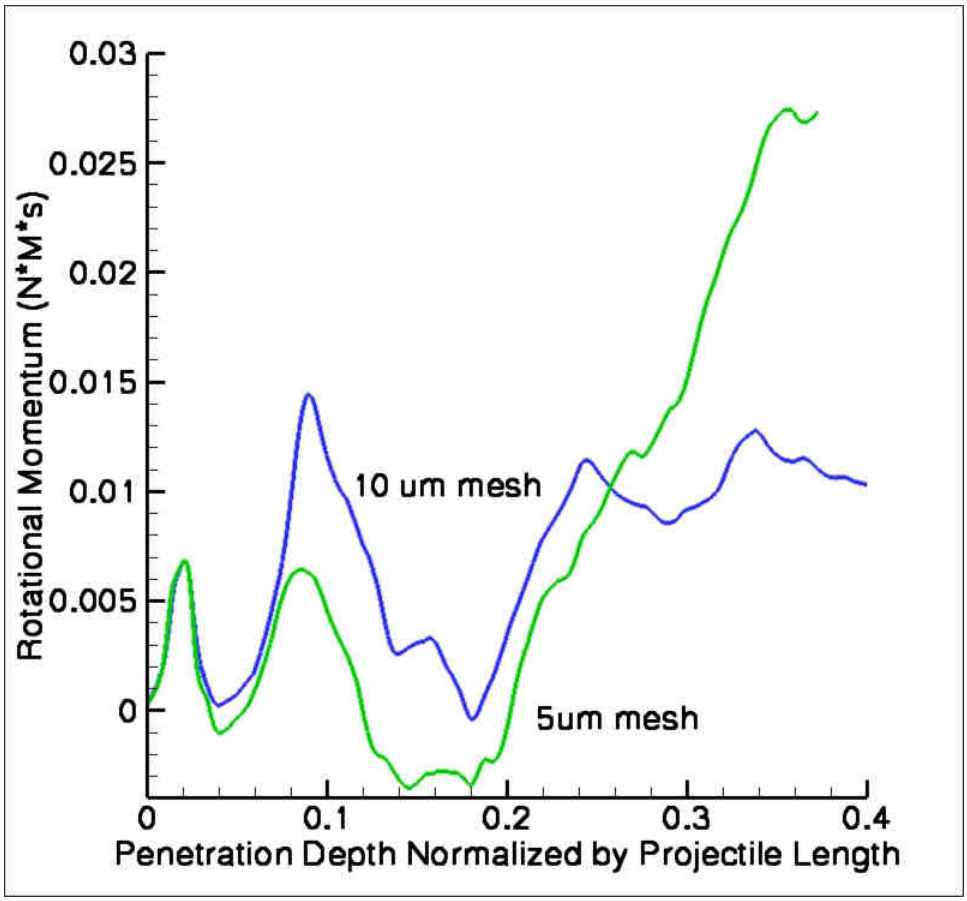

Figure A.3: Rotational momentum curves emphasizing projectile mesh size effects.

Appendix B: Vibration Mode Code Validation

The Finite Element Program (FE) used to calculate the projectile vibrational modes was written using Matlab and can be found in appendix 3. To verify that no programming mistakes were made and that the method is sound, the code was used to calculate the first three bending modes for the problem of a cantilever beam.

The beam was fixed at it left side and had dimensions of .1 m high, 1 m deep, and 5 m long. The slenderness ratio of the beam was 50 making Euler-Bernoulli beam theory applicable. Using beam theory Bottega [67] analytically calculated the first three bending modes for this problem, results can be found in Table B.1 in the analytic row.

The first three bending modes of the beam were calculated using three different mesh sizes of 50, 25, and 10 mm. Results for these calculations can again be found in Table B.1 and compared against the theoretical values. As the mesh is refined the FE calculations converge to the theoretical value and have a relative error of less than 1.008 for the lowest mode. The first three calculated mode shapes can be seen in Figure B.1 and conform to theory.

Table B.1: Bending modes for a cantilever beam

Solution	ω_1 Hz	Error ω_1	ω_2 Hz	Error ω_2	ω_3 Hz	Error ω_3
Analytic	20.57	-	128.9	-	361.0	-
50 mm mesh	25.468	1.238	159.3	1.235	440.6	1.231
25 mm mesh	21.665	1.053	135.4	1.050	378.35	1.048
10 mm mesh	20.727	1.008	129.7	1.006	362.26	1.004

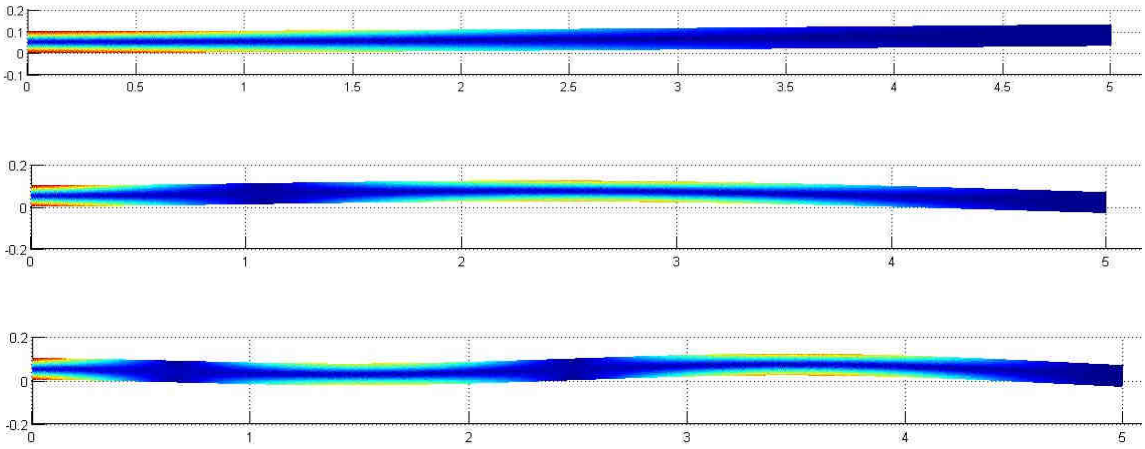

Figure B.1 First three calculated bending modes showing contours of effective stress (arbitrary units)

Appendix C: Matlab Bending Mode Program

```
%Eigen Solver for to find structural bending modes using constant
strain triangle finite elements
clc
clear
format long
fid=fopen('ogive.mesh', 'r');%Read in the mesh
val=fscanf(fid, '%d %d', 2)
pts=fscanf(fid, '%e %e', [2,val(1)]);
con=fscanf(fid, '%d %d', [3,val(2)]);
pts=pts';
pts=pts/1000.0;%convert to meters
con=con';
cnta=0
fclose(fid);
%produce materail properties matrix
Kmod=163.9e9;%Pa
Gmod=77.5e9;%Pa
ro=7823.0*2
Emod=9*Kmod/(1+3*Kmod/Gmod);
poi=(1-2*Gmod/(3*Kmod))/(2+(2*Gmod)/(3*Kmod));
%poi=0.0
E=[1.0-poi,poi,0;poi,1.0-poi,0;0,0,(1.0-
2.0*poi)/2.0]*Emod/((1.0+poi)*(1.0-2.0*poi));

K(1:val(1)*2,1:val(1)*2)=0.0;
mass(1:val(1)*2,1:val(1)*2)=0.0;
Atot=0.0;
for i=1:val(2);
%Formulate B matrix for CST
B(1,1)=pts(con(i,2),2)-pts(con(i,3),2);
B(1,2)=0.0;
B(1,3)=pts(con(i,3),2)-pts(con(i,1),2);
B(1,4)=0.0;
B(1,5)=pts(con(i,1),2)-pts(con(i,2),2);
B(1,6)=0.0;
B(2,1)=0.0;
B(2,2)=pts(con(i,3),1)-pts(con(i,2),1);
B(2,3)=0.0;
B(2,4)=pts(con(i,1),1)-pts(con(i,3),1);
B(2,5)=0.0;
B(2,6)=pts(con(i,2),1)-pts(con(i,1),1);
B(3,1)=pts(con(i,3),1)-pts(con(i,2),1);
B(3,2)=pts(con(i,2),2)-pts(con(i,3),2);
B(3,3)=pts(con(i,1),1)-pts(con(i,3),1);
B(3,4)=pts(con(i,3),2)-pts(con(i,1),2);
B(3,5)=pts(con(i,2),1)-pts(con(i,1),1);
B(3,6)=pts(con(i,1),2)-pts(con(i,2),2);
%Calculate Area of the CST
A=.5*det([pts(con(i,1),1),pts(con(i,1),2),1.0;pts(con(i,2),1),pts(con(i
,2),2),1.0;pts(con(i,3),1),pts(con(i,3),2),1.0]);
B=B/(2.0*A);
Atot=Atot+A;
%Produce the Mass Matrix
```

```
mass(con(i,1)*2-1,con(i,1)*2-1)=mass(con(i,1)*2-1,con(i,1)*2-
1)+ro*A*1.0/3.0;
mass(con(i,1)*2,con(i,1)*2)=mass(con(i,1)*2,con(i,1)*2)+ro*A*1.0/3.0;
mass(con(i,2)*2-1,con(i,2)*2-1)=mass(con(i,2)*2-1,con(i,2)*2-
1)+ro*A*1.0/3.0;
mass(con(i,2)*2,con(i,2)*2)=mass(con(i,2)*2,con(i,2)*2)+ro*A*1.0/3.0;
mass(con(i,3)*2-1,con(i,3)*2-1)=mass(con(i,3)*2-1,con(i,3)*2-
1)+ro*A*1.0/3.0;
mass(con(i,3)*2,con(i,3)*2)=mass(con(i,3)*2,con(i,3)*2)+ro*A*1.0/3.0;
Kelem=A*transpose(B)*E*B;%K for the element
%build K with Kelem
for j=1:3
    for m=1:3
        K(con(i,j)*2-1,con(i,m)*2-1)=K(con(i,j)*2-1,con(i,m)*2-
1)+Kelem(j*2-1,m*2-1);
        K(con(i,j)*2,con(i,m)*2-1)=K(con(i,j)*2,con(i,m)*2-
1)+Kelem(j*2,m*2-1);
        K(con(i,j)*2-1,con(i,m)*2)=K(con(i,j)*2-
1,con(i,m)*2)+Kelem(j*2-1,m*2);

K(con(i,j)*2,con(i,m)*2)=K(con(i,j)*2,con(i,m)*2)+Kelem(j*2,m*2);
    end
end
end
solve=2
if(solve==1)%Solve for with constraints (used to constrain the beam
problem)
%find u constraints
    ucon(1:val(1)*2)=0;
    u(1:val(1)*2)=0.0;
    for i=1:val(1);
        if(pts(i,1)<-10.00001)%impose displacement constraints
           u(i*2)=0.0;
           u(i*2-1)=0.0;
           ucon(i*2)=1;
           ucon(i*2-1)=1;
           cnta=cnta+2;
        end
    end
%find F constraints
    Fcon(1:val(1)*2)=0;
    F(1:val(1)*2)=0.0;
    load=1000000.0;
    nds=0
    for i=1:val(1);
        if(pts(i,1)>100.9999)%find nodes that will have applied loads
nds=nds+1
        end
    end
    for i=1:val(1);
        if(pts(i,1)>100.9999)%Apply loads to the mesh
           F(i*2)=load/nds;
           %load=load+F(i*2-1)
           Fcon(i*2)=1;
        end
    end
```

```
    %find constrained stiffness matrix
    KF(1:val(1)*2-cnta,1:val(1)*2-cnta)=0.0;
    massF(1:val(1)*2-cnta,1:val(1)*2-cnta)=0.0;

    Fsrt(1:val(1)*2-cnta,1)=0.0;
    cnta=0;
    cntb=0;
    for i=1:val(1)*2
       i/(val(1)*2)
            if(ucon(i)==1);
                cnta=cnta+1;

                continue
            end
            cntb=0;
            Fsrt(i-cnta,1)=F(i);

        for j=1:val(1)*2
            if(ucon(j)==1);
                cntb=cntb+1;

                continue
            end
        KF(i-cnta,j-cntb)=K(i,j);
        massF(i-cnta,j-cntb)=mass(i,j);
        end
    end
    %UFin=inv(KF)*Fsrt;
    cnta=0;
    %for i=1:val(1)*2
    %        if(ucon(i)==1);
    %            cnta=cnta+1;
    %            continue
    %        end
    %u(i)=UFin(i-cnta);
    %end
    dpts(val(1),2)=0;

cnta=0.0
 %   for i=1:val(1);
    %        if(ucon(i)==1);
    %            cnta=cnta+1;
   %             continue
  %           end
    %dpts(i,1)=pts(i,1)+u(i*2-1);
    %dpts(i,2)=pts(i,2)+u(i*2);
 %   end
    %for i=1:val(1)*2
      %  if(Fcon(i)==1)
       %     u(i);
       %  end
   % end
   [V,D] = eigs(KF,massF,50,'sm');
end
   if(solve==2)%unconstrained body
           %KF=K;
```

```
            %massF=mass;
            cntb=0;
            cnta=0;
            ucon(1:val(1)*2)=0;
            u(1:val(1)*2)=0.0;
            opts.tol=1e-50;
            [V,D] = eigs(K,mass,50,'sm',opts);

end
clear K mass KF massF



for i=1:6%val(1)*2-cnta

   if(D(i,i)<inf)
      i
       sqrt(D(i,i))
   end
end

%calculate theoretical W's for a cantilever beam
w1=3.516*(Emod*(.1^3/12)/(.1*ro*5^4))^.5
w2=22.03*(Emod*(.1^3/12)/(.1*ro*5^4))^.5
w3=61.70*(Emod*(.1^3/12)/(.1*ro*5^4))^.5

%Calculate Error between calculated and theoretical W
e1=sqrt(D(1,1))/w1
e1=sqrt(D(2,2))/w2
e1=sqrt(D(3,3))/w3
```

Visualization program used to plot mode shapes

```
%This M-file is used to plot the results of the previously performed
eiganvalue analysis

mode=6
cont=4; %1 strain x, 2 strain y, 3 strain xy , 4 sef
cnta=0;
ncnt(1:val(1))=0;
nstrn(1:val(1),1:4)=0.0;
%V(:,mode)/1000.0
Estrn(val(2),1:3)=0.0;
    for i=1:val(1);
        if(ucon(i*2)==1)
    Ufin(i,1)=0.0;
    Ufin(i,2)=0.0;
        dpts(i,1)=pts(i,1);
        dpts(i,2)=pts(i,2);
            cnta=cnta+1;

            continue
        end
    Ufin(i,1)=V((i-cnta)*2-1,mode);
    Ufin(i,2)=V((i-cnta)*2,mode);
    dpts(i,1)=pts(i,1)+V((i-cnta)*2-1,mode)/1000000.00;
    dpts(i,2)=pts(i,2)+V((i-cnta)*2,mode)/1000000.00;
    end

for i=1:val(2);
%Find local dispacment
    Uloc(1,1)=Ufin(con(i,1),1);
    Uloc(2,1)=Ufin(con(i,1),2);
    Uloc(3,1)=Ufin(con(i,2),1);
    Uloc(4,1)=Ufin(con(i,2),2);
    Uloc(5,1)=Ufin(con(i,3),1);
    Uloc(6,1)=Ufin(con(i,3),2);
%Formulate B matrix for CST
B(1,1)=pts(con(i,2),2)-pts(con(i,3),2);
B(1,2)=0.0;
B(1,3)=pts(con(i,3),2)-pts(con(i,1),2);
B(1,4)=0.0;
B(1,5)=pts(con(i,1),2)-pts(con(i,2),2);
B(1,6)=0.0;
B(2,1)=0.0;
B(2,2)=pts(con(i,3),1)-pts(con(i,2),1);
B(2,3)=0.0;
B(2,4)=pts(con(i,1),1)-pts(con(i,3),1);
B(2,5)=0.0;
B(2,6)=pts(con(i,2),1)-pts(con(i,1),1);
B(3,1)=pts(con(i,3),1)-pts(con(i,2),1);
B(3,2)=pts(con(i,2),2)-pts(con(i,3),2);
B(3,3)=pts(con(i,1),1)-pts(con(i,3),1);
B(3,4)=pts(con(i,3),2)-pts(con(i,1),2);
B(3,5)=pts(con(i,2),1)-pts(con(i,1),1);
B(3,6)=pts(con(i,1),2)-pts(con(i,2),2);
```

```
A=.5*det([pts(con(i,1),1),pts(con(i,1),2),1.0;pts(con(i,2),1),pts(con(i
,2),2),1.0;pts(con(i,3),1),pts(con(i,3),2),1.0]);
B=B/(2.0*A);
%Compute Element Strains
Estrn(i,1:3)=B*Uloc;


for j=1:3
nstrn(con(i,j),1)=nstrn(con(i,j),1)+Estrn(i,1);
nstrn(con(i,j),2)=nstrn(con(i,j),2)+Estrn(i,2);
nstrn(con(i,j),3)=nstrn(con(i,j),3)+Estrn(i,3);
end
ncnt(con(i,1))=ncnt(con(i,1))+1;
ncnt(con(i,2))=ncnt(con(i,2))+1;
ncnt(con(i,3))=ncnt(con(i,3))+1;
end
for i=1:val(2)
    sigz=(Estrn(i,1)-Estrn(i,2))*poi*Emod/((1.0+poi)*(1.0-2.0*poi));
    strn(1,1)=Estrn(i,1);
    strn(2,1)=Estrn(i,2);
    strn(3,1)=Estrn(i,3);
    Estress=E*strn;
    Estrn(i,4)=1/sqrt(2)*((Estress(1)-Estress(2))^2+(Estress(2)-
sigz)^2+(sigz-Estress(1))^2+6*(Estress(3)^2))^.5;
end
for i=1:val(1);
    for j=1:3;
        nstrn(i,j)=nstrn(i,j)/ncnt(i);
    end
    sigz=(nstrn(i,1)-nstrn(i,2))*poi*Emod/((1.0+poi)*(1.0-2.0*poi));
    strn(1,1)=nstrn(i,1);
    strn(2,1)=nstrn(i,2);
    strn(3,1)=nstrn(i,3);
    stress=E*strn;
    nstrn(i,4)=1/sqrt(2)*((stress(1)-stress(2))^2+(stress(2)-
sigz)^2+(sigz-stress(1))^2+6*(stress(3)^2))^.5;
end

trisurf(con,dpts(:,1),dpts(:,2),[],Estrn(:,cont),'LineStyle', 'none')
view(0,90)
daspect([1 1 1])
```